

**Mechanical and biochemical
stimulation of suspended cells in
a microfluidic device
probed with dual optical tweezers**

Dissertation

for the award of the degree

“Doctor rerum naturalium”

of the Georg-August-Universität Göttingen

within the promotion program ProPhys

of the Georg-August University

School of Science (GAUSS)

submitted by

Samaneh Rezvani

from Boroujen (Iran)

Göttingen, 2017

Thesis Committee:

Prof. Dr. Christoph F. Schmidt

3rd Institute of Physics- Biophysics
Georg-August-Universität Göttingen

Prof. Dr. Andreas Janshoff

Institute for Physical Chemistry
Georg-August-Universität Göttingen

Members of the Examination Board:

Reviewer: Prof. Dr. Christoph F. Schmidt

3rd Institute of Physics- Biophysics
Georg-August-Universität Göttingen

2nd reviewer: Prof. Dr. Andreas Janshoff

Institute for Physical Chemistry
Georg-August-Universität Göttingen

Further members of the Examination Board:

Prof. Dr. Marcus Müller

Institute for Theoretical Physics
Georg-August-Universität Göttingen

Prof. Dr. Stefan Klumpp

Institute for Nonlinear Dynamics
Georg-August-Universität Göttingen

Dr. Claus Heussinger

Institute for Theoretical Physics
Georg-August-Universität Göttingen

Dr. Andreas Neef

Bernstein Center for Computational Neuroscience
Max Planck Institute for Dynamics and Self-Organization, Göttingen

Date of Oral Examination: 17.11.2017

Contents

1	Introduction	1
1.1	Outline	6
2	Methods and materials	7
2.1	Optical trapping	7
2.1.1	General description	8
2.1.2	Back focal plane interferometry	10
2.1.3	Calibration of detector signal	11
2.1.4	Optical trapping set-up	14
2.2	Two-particle microrheology to probe cellular force	20
2.2.1	Cellular force probed in passive and active modes	21
2.2.2	Stiffness measurements	24
2.2.3	Representative force measurements	26
2.3	Materials	29
2.3.1	Cell culture	29
2.3.2	Materials and working solutions	31
3	Microfluidic chamber for manipulation of suspended cells	35
3.1	Introduction	35

Contents

3.1.1	Microfluidic stickers; NOA-81 rather than PDMS	37
3.1.2	Device configuration	38
3.1.3	Photo-polymerization of hydrogel membranes	39
3.2	Device requirements for microrheology using optical trap	44
3.2.1	Geometry required for cells microrheology	44
3.2.2	Surface treatment and hydrophobicity	45
3.2.3	Fluid flow control	47
3.2.4	Bio- and optical- compatibility	48
3.2.5	Recycling microfluidic stickers	48
3.3	Device fabrication	49
3.3.1	Stickers preparation	49
3.3.2	Hydrogel membrane fabrication using confocal microscopy	51
3.4	Device characteristics	54
3.4.1	Beam path inside the flow chamber	54
3.4.2	HMM thickness, pore size and exposure time	57
3.4.3	Diffusion through HMM	61
3.5	Summary and conclusion	63
4	Cellular morphology and mechanics in response to biochemical stimuli	65
4.1	Introduction	65
4.1.1	3D cellular morphology	66
4.1.2	Cytoskeleton structures, morphology and cell mechanics	68
4.1.3	Interfering with myosin contractility	69
4.1.4	Experimental approach	71

4.2	Cellular morphology and mechanics	73
4.3	Biochemical stimulation and cellular morphology	75
4.4	Cellular mechanics and biochemical stimulation (novel approach)	78
4.4.1	Microrheology inside a microfluidic device	78
4.4.2	Results	79
4.5	Discussion	88
5	Cell mechanics under osmotic pressure	93
5.1	Theory: osmotic pressure, cortical tension and cell volume	93
5.2	Experimental approach	97
5.2.1	Single step osmotic change in conventional macro-chambers	97
5.2.2	Multi-step osmotic change in a novel microfluidic chamber	98
5.3	Results	101
5.3.1	Single step osmotic compression	101
5.3.2	Multi step gradual osmotic compression	103
5.4	Discussion	109
6	Conclusions	115
A	Appendix	119
A.1	Biochemical protocols	119
A.1.1	Coating of beads	119
A.1.2	Glass cover-slip coating	121
A.1.3	Conventional sample preparation for two-particle microrheology	122
B	Appendix	123

Contents	
B.1 Optics alignment procedure	123
B.1.1 AOD adjustment	123
C Appendix	125
C.1 Soft lithography protocols.	125
C.1.1 Procedure for $\sim 40\text{-}50\ \mu\text{m}$ photoresist using SU-8 3050.	125
C.1.2 Procedure for $\sim 70\ \mu\text{m}$ photoresist using SU-8 3050.	126
D Appendix	129
D.1 Microfluidic device fabrication	129
D.1.1 Microfluidic NOA-81 sticker	129
D.1.2 Hydrogel membrane fabrication	131
Bibliography	133
List of Figures	147
Abbreviations	148
Acknowledgments	150
Affidavit	154
Curriculum Vitae	156

Introduction

Cells communicate with their environment through biochemical and mechanical interactions. They can respond to stimuli by undergoing shape and, in some situations, volume changes. Living cells of both plants and animals are enclosed by a semi-permeable membrane which forms a selective barrier between the cell and its environment such that water molecules, for instance, can pass through the membrane. As water is incompressible, fluid flow is directly related to the cell volume [1].

Unlike plant and bacterial cells, animal cells have no rigid cell wall to resist large forces, instead eukaryotic cell shape is determined by the cortex, a thin network of actin filaments, myosin motors and crosslinking proteins underneath the plasma membrane. Non-muscle myosin II motors move actin filaments in an anti-parallel way and create contractile stress in networks of actin. In fact, myosin generated tension, ion transport and water flows contribute to the control of cell shape and volume [2].

On the other hand, volume and shape are tightly connected to cell mechanics. Key determinants of the mechanical response of a cell are the viscoelastic prop-

erties of the actomyosin cortex, effective surface tension, and osmotic pressure [1].

In animal organs and tissues, cells live in a complex three dimensional (3D) microenvironment. Many basic and clinical in vitro research studies, however, have been done in two dimensional (2D) geometries. Easy environmental control, cell manipulation, imaging and measurement are the main advantages of 2D cell cultures. Nevertheless, this approach decreases compatibility with in vivo system and also increases drug sensitivity in both clinical and fundamental investigations [3].

The structure of the cytoskeleton in adherent cells that are spreading in 2D and flattening by attaching to a flat substrate, is different from their real 3D configuration [4]. Apart from that, an inhomogeneous distribution of the organelles and intracellular structures affects the measured values for mechanical properties. It has been shown that cytoskeletal structures such as actin filaments and microtubules as well as the different cellular organelles like the nucleus, all are contributing to the physical properties and shape stability of the cell [5].

The cortex of cells with a finite surface tension maintains the integrity of the eukaryotic cells against external forces and plays a crucial role in the regulation of cell volume. Particularly non-muscle myosin II builds up tension and is responsible to make contraction on the cortex. Hence it plays a role in maintenance of cell shape and integrity. Its function in cortical tension and cell stiffness has been studied in [6][7][8],[9].

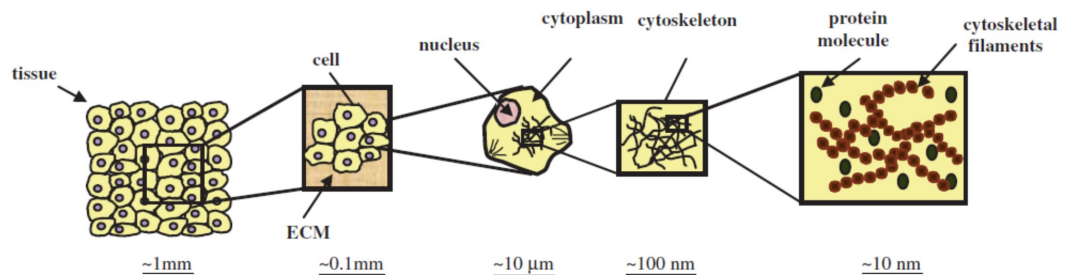


Figure 1.1.: Typical length scales in cell mechanics. Schematic cascade from tissue down to cytoskeletal filaments to single molecules. Adapted from [10]

Blood cells are the best known examples of non-adhering cells. An schematic

of a leukocyte with the myosin family members, commonly expressed by immune cells, and their function is shown in Fig.1.2. The schematic representation of myosin II structure is marked. Each non-muscle myosin (NMM) II presents head domains which can attach to actin and hydrolyze ATP. It binds to two pairs of light chains that regulate the motor function, and the tail domain responsible for bipolar filament formation. It generates contractility on actin-structured networks and regulates the tension in the cell cortex, therefore playing a key role in maintaining the cell shape integrity [11].

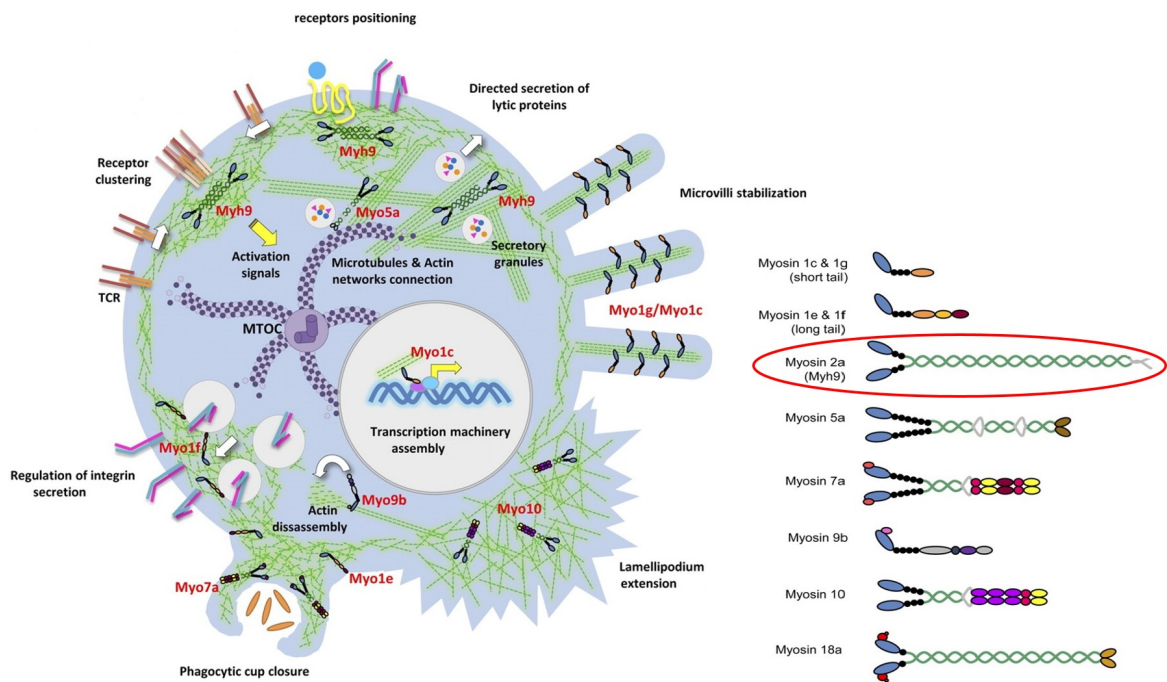


Figure 1.2.: Myosin family in leukocytes. Common functions of myosin family in immune cells is demonstrated in a schematic leukocyte. A legend of different myosins is depicted on the right side. NM myosin II is marked. Figure is adapted from [11]

Myosin force generation within the cortex of a rounded up cell increases surface tension. This helps to keep the integrity of the cell against external forces and hydrostatic pressure, as well as regulates the volume of the cell. (Jiang et al.2012) presented a model system of rounded cells, in which water permeation, active stress in the cortex, as well as mechanosensitive channels and ion pumps all are involved in cellular volume and pressure regulation [1].

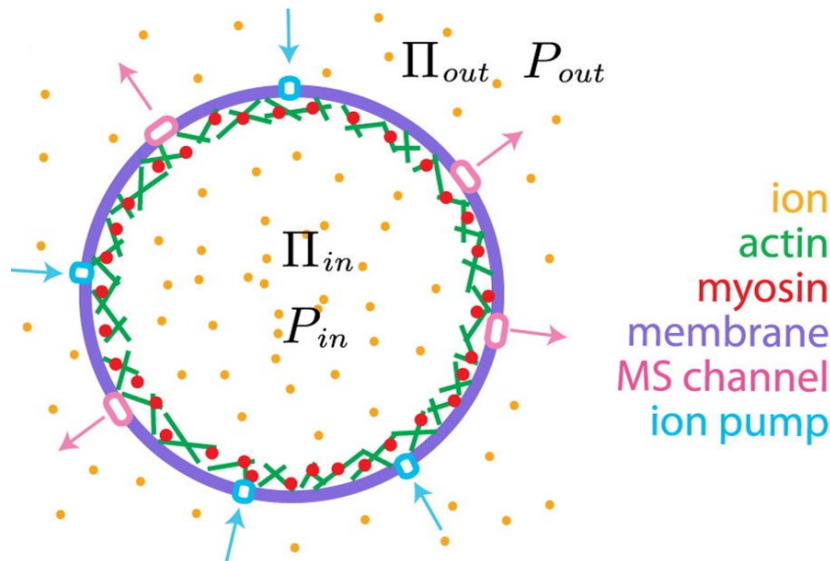


Figure 1.3.: Cellular pressure and volume regulation. Schematic illustration of a rounded-up cell. Water permeation, active stress in the cortex, as well as mechanosensitive channels and ion pumps all are involved in cellular volume and pressure regulation. Picture and model taken from [1]

– Methods

There are several techniques to study the mechanics of suspended cells including micropipette aspiration, magnetic and optical tweezers, AFM and more recently optical stretchers. They typically apply different ranges of forces and measure stiffness in different ranges. AFM goes up to nN and can measure the stiffness of 10-100 pN/ μ m. Magnetic tweezers by means of a magnetic field gradient can measure displacements of the order of 10 nm and apply forces from 0.05 to 20 pN and therefore can measure a lower stiffness \sim 0.1 pN/nm. Optical tweezers using light intensity gradients can go to the sub nm range (0.1 nm), and apply typical force from 0.1 to 100 pN, which is small enough to measure stiffnesses of 100s pN/ μ m [10][12],[13].

Micropipette aspiration and parallel glass plate have been used to determine cortical tension, intracellular pressure and elastic modulus. In spite of easy implementation, they require large deformation in the cortex for long times, which might activate mechanosensitive signal transduction which in turn may alter cortical mechanics. Optical trapping on the other hand provides localized point measurements. In fact, it measures an effective tension however it is difficult to char-

acterize the cortical part of this tension [14].

In this thesis, we focus on optical tweezers. Using a dual optical trap (OT) makes it possible to probe the viscoelasticity of suspended cells (in 3D), by active and passive microrheology. We quantify the mechanical response of the cells under various conditions and compare different cell lines.

Compared with flattened cells on a substrate, keeping cells in suspension while only partially adhering to beads creates a configuration that is closer to their 3D natural environment. However large variation from cell to cell has made it difficult to measure the effect of drug interference precisely [15].

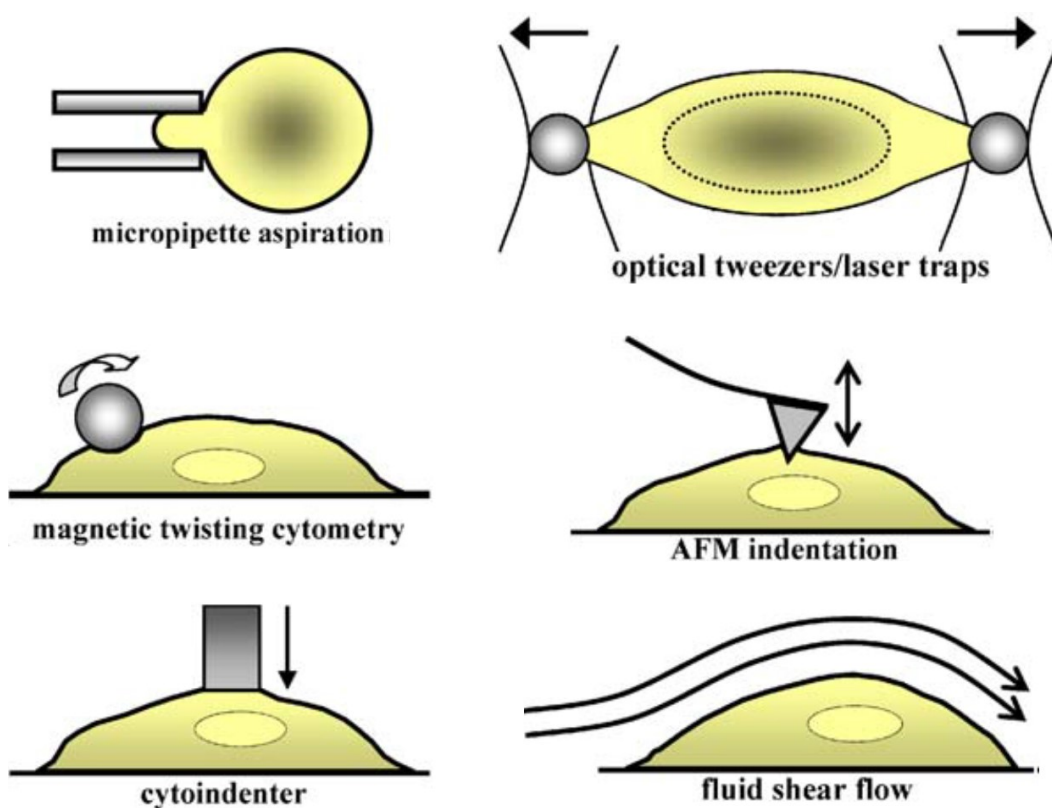


Figure 1.4.: Experimental techniques for probing cell mechanics. Schematic illustration of common experimental techniques. Picture is adapted from [10].

We use a custom-designed microfluidic device with integrated hydrogel micro-windows to rapidly change solution conditions for cells suspended by optical traps without direct fluid flow. We use biochemical inhibitors and different osmolytes to

investigate the time-dependent response of individual cells. The new experimental approach and the results of this work help to understand mechanical properties of cells in 3D, the impact of interior cytoskeletal structure and time-dependent cell response to mechanical and biochemical perturbations.

1.1 Outline

At the beginning of the 2nd chapter, an introduction to optical trapping and microrheology is given. Then the materials and methods used for culturing, transfection and handling the cells, in addition to fluid chambers, is presented.

The 3rd chapter provides an extensive description of our novel microfluidic device, as the main result of this work. Technical details of requirements and fabrication, to characteristics and advantages are explained. We used this chamber for time-dependent studies of mechanical properties of single cells undergoing biochemical and mechanical stimulations.

In the following chapters, the first successful application of this device in biophysical studies is shown.

In chapter 4, biochemical stimulation of cells in suspension is investigated. The interconnection between cell morphology and mechanics is explored by intrastuctural perturbation exclusively. Special attention is paid to the results with individual cells suspended in a micro-fluidic device under molecular motor inhibition.

The 5th chapter focuses on osmotic pressure as a mechanical stimulus for the cells. Again, force fluctuations and cell stiffness measurements obtained with a dual optical trap are described. Successful attempts to control osmotic stress on cells suspended in a micro-fluidic chamber is shown. Physical properties of cells under rapid exchange of osmolytes are presented and the outcomes are discussed.

Chapter 6 concludes the work and gives an outlook for potential follow-up investigations in future. Detailed protocols can be found in the appendix, followed by the cited references at the end.

Methods and materials

“Physics is simple in theory, but in practice is filled with the possibility for limitless error.”

Christopher Pike

2.1 Optical trapping

Ten years after the advent of lasers, Arthur Ashkin was the first one who studied radiation pressure of light. Ever since he had managed to manipulate and lift the micro-particles against the gravity with focused laser light, researchers have been exploring new specimens in different biophysical aspects using radiation pressure of light. Very fast it had been developed from manipulation of live bacteria, viruses and sperms to DNA and chromosomes [16][17][18].

2.1.1 General description

The physics behind optical trapping is the difference between the momentum of the photons entering and leaving a nano- or micro-object, translates to the difference in object's momentum. Regarding momentum calculation there are different regimes for different particle size with respect to the wavelength of the trapping laser light; ray-optics regime for particle diameter much larger than wavelength ($r \gg \lambda$), and rayleigh regime for particles much smaller than that ($r \ll \lambda$). However, up to now the most common applications of the optical tweezers for biophysical studies has been done with micro-meter sized beads and trapping laser in the visible or near infrared range, therefore both have the same order of magnitude. Thus force calculation in this case needs an approach between these two limits. Following is a short description of the two mentioned regime.

- Ray optics regime:

For particles much bigger than the wavelength of light ($r \gg \lambda$), geometric optics can be used to calculate the momentum transfer of the trapping particle. According to Newton's second law, force on the particle is equal to the difference of momentum flux between entering and leaving light of a dielectric particle:

$$\vec{F} = \frac{d\vec{F}}{dt} = n_m/c \iint (\vec{S}_{in} - \vec{S}_{out})dA \quad (2.1)$$

where n_m is the refractive index of the surrounding medium, c speed of light, $\vec{S} = \vec{E} \times \vec{B}$ the Poynting vector for an electromagnetic wave, and A is a cross section area of the particle perpendicular to the light propagation direction. Based on force balance between the 'scattering force' in direction of light propagation, and the 'gradient force' in the direction of intensity gradient, lateral and axial gradient force exerted on the particle is demonstrated in Fig.2.1. For more information see [19],[20].

- Rayleigh regime:

When the particle radius is smaller than the wavelength of light ($r \ll \lambda$), scattering and gradient force are separable as following:

$$F_{scat} = n_m/c \langle S \rangle \sigma \quad (2.2)$$

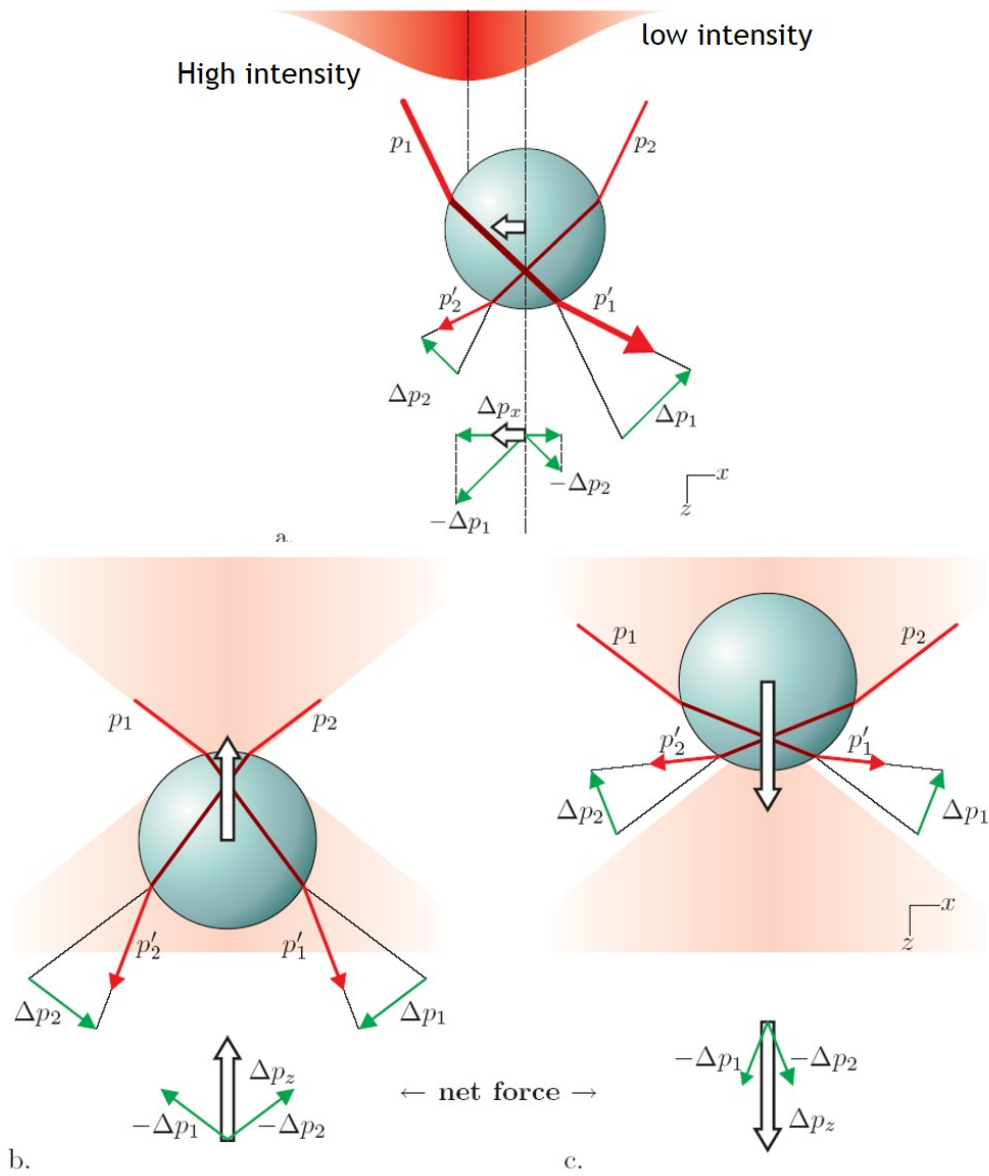


Figure 2.1.: Optical tweezers principle in Ray regime. a) Lateral gradient force in non-uniform laser intensity. b,c) Axial gradient force toward the focus of laser light. The net force is shown qualitatively with white arrows. Adapted from [19].

while

$$\sigma = 8/3\pi(kr)^4 r^2 \left(\frac{m^2 - 1}{m^2 + 2} \right)^2. \quad (2.3)$$

n refractive index of the trapping particle, and $m = n/n_m$ relative indices, and

$k = 2\pi n_m/\lambda$ is the wave number of incident light. The scattering force again is in the direction of light propagation, however, the gradient force toward the center of the trap is given by

$$F_{grad} = \frac{\alpha}{2} \nabla \langle E^2 \rangle \quad (2.4)$$

where

$$\alpha = n_m^2 r^3 \left(\frac{m^2 - 1}{m^2 + 2} \right). \quad (2.5)$$

Stable trapping will be achieved by maximizing the gradient force with respect to the scattering force or the Q-factor as

$$Q = \frac{F_{grad}}{F_{scat}} = \frac{3\sqrt{3}}{64\pi^5} \frac{n_m^2}{\left(\frac{m^2-1}{m^2+2}\right)} \frac{\lambda^5}{r^3 \omega_0^2}. \quad (2.6)$$

when ω_0 is the width of Gaussian beam:

$$\omega_0 = \frac{\lambda}{\pi NA}. \quad (2.7)$$

Q-factor scales with $1/r^3$, so a smaller particle and higher refractive index (causes $m > 1$) results in a more stable trapping. It's also obvious that an objective lens with a high numerical aperture is a critical component for such a condition.

2.1.2 Back focal plane interferometry

In experiment, trapping laser light after passing through the sample will scatter. Both scattered beam from the sample and transmitted beam (trapping beam) will be collected by a condenser lens. Superposition of them will result in an interferometric pattern on back focal plane (BFP) of the condenser. The characteristics of this pattern, depends on the relative position of two beams which will reach two quadrant photo diodes (QPDs) later, and will be translated to spatial distribution of the intensity (Fig.2.2). Therefore, any movement of trapping particle will shift the interference pattern in BFP detected by QPD. This technique known as back focal plane interferometry (see Fig.2.2), first time presented by (Gittes et al.1998), for a Rayleigh particle that is laterally displaced from the focus of a Gaussian beam [21].

Intensity distributions (differential signals) D_x , D_y can be calculated as follow-

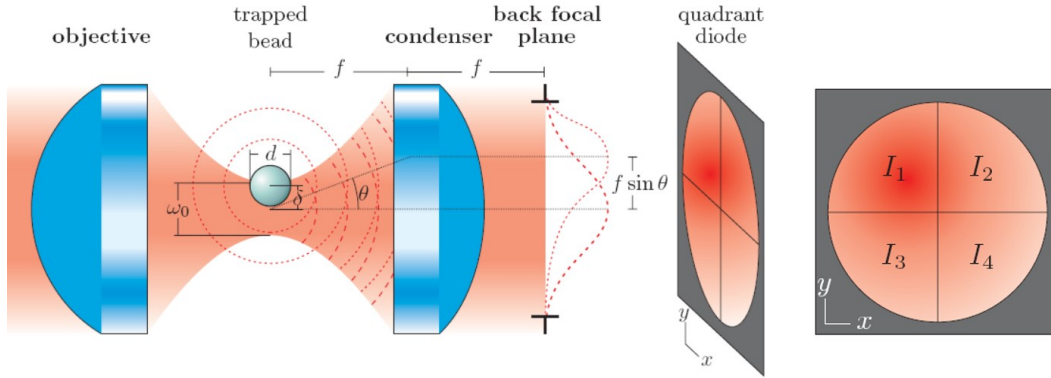


Figure 2.2.: Back-focal-plane interferometry. On left, lateral displacement of a trapped particle from the trap center is shown. Scattered and transmitted light are collected by a condenser lens. When their far-field interference will shift the intensity distribution in the back-focal-plane of the condenser. On the right hand side, intensity distribution on a quadrant photo diode, is illustrated. Lateral resolution of displacements taken in this way is down to sub nanometer. Figure taken from [19].

ing

$$\begin{cases} I_{y+} = I_1 + I_2 \\ I_{y-} = I_3 + I_4 \end{cases} \quad \begin{cases} I_{x+} = I_2 + I_4 \\ I_{x-} = I_1 + I_3 \end{cases} \quad (2.8)$$

$$D_y = \frac{I_{y+} - I_{y-}}{I_{y+} + I_{y-}}. \quad (2.9)$$

and

$$D_x = \frac{I_{x+} - I_{x-}}{I_{x+} + I_{x-}}. \quad (2.10)$$

For small displacements ($\sim \pm 250$ nm), QPD's photo-current to voltage response remains linear Fig.2.3, without crosstalk between x- and y-channels.

2.1.3 Calibration of detector signal

In order to measure the force using an optical trap (OT), first the detector response has to be calibrated. A simple but practical approach is to make use of Brownian motion of a particle trapped in a viscous medium. Here, we explain the motion equation of a dielectric particle under such condition, and then show how to use the power spectral density of its motion. The motion equation is

$$m \frac{\partial^2 x}{\partial t^2} + \gamma \frac{\partial x}{\partial t} + kx(t) + F(t) = 0 \quad (2.11)$$

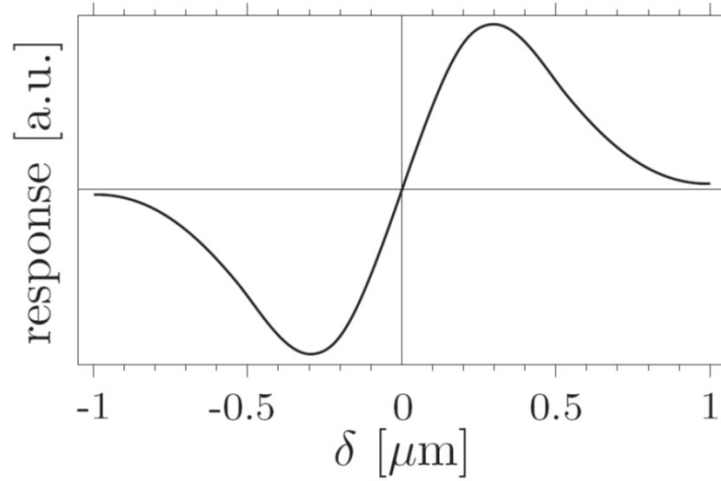


Figure 2.3.: Quadrant photo diode response. For small displacements of $\delta \sim \pm 250$ nm, QPD response is remained linear. Figure taken from [19].

where m is the mass of the particle, γ is a hydrodynamic drag coefficient and k is the trap stiffness. $\gamma \frac{\partial x}{\partial t}$ term shows the drag force exerted on the particle from the medium and kx term is the restoring force of the trap. $F(t)$ is the thermal force causing Brownian motion, therefore, has the time averaged of zero, $\langle F(t) \rangle = 0$. Eventually, the solution for $x(t)$ will be product the multiplication of an exponential decay due to a damping provided by medium, times a periodic term caused by trapping light, plus additional effect of Brownian motion, so

$$x(t) \propto e^{-\frac{\gamma t}{m}} \cos\left(\sqrt{\frac{k}{m}} t\right). \quad (2.12)$$

After solving the motion equation, one can calculate the power spectrum of the particle's position which is a Lorentzian function [22]:

$$S_x(f) = \frac{k_B T}{\pi^2 \gamma (f_c^2 + f^2)} \quad (2.13)$$

where k_B is Boltzmann's constant and T absolute temperature and

$$f_c = \frac{k}{2\pi\gamma} \quad (2.14)$$

is defined as a characteristic frequency so-called 'corner frequency'. For frequencies ($f \ll f_c$), the power spectrum is approximately constant indicating that particle is confined. However, at higher frequencies ($f \gg f_c$), $S_x(f)$ is falling off

with the $1/f^2$ (or ω^{-2}), similar to the free diffusion of the particle. Meaning, in short time scale, particle does not feel the confinement from the trap (see Fig.2.4).

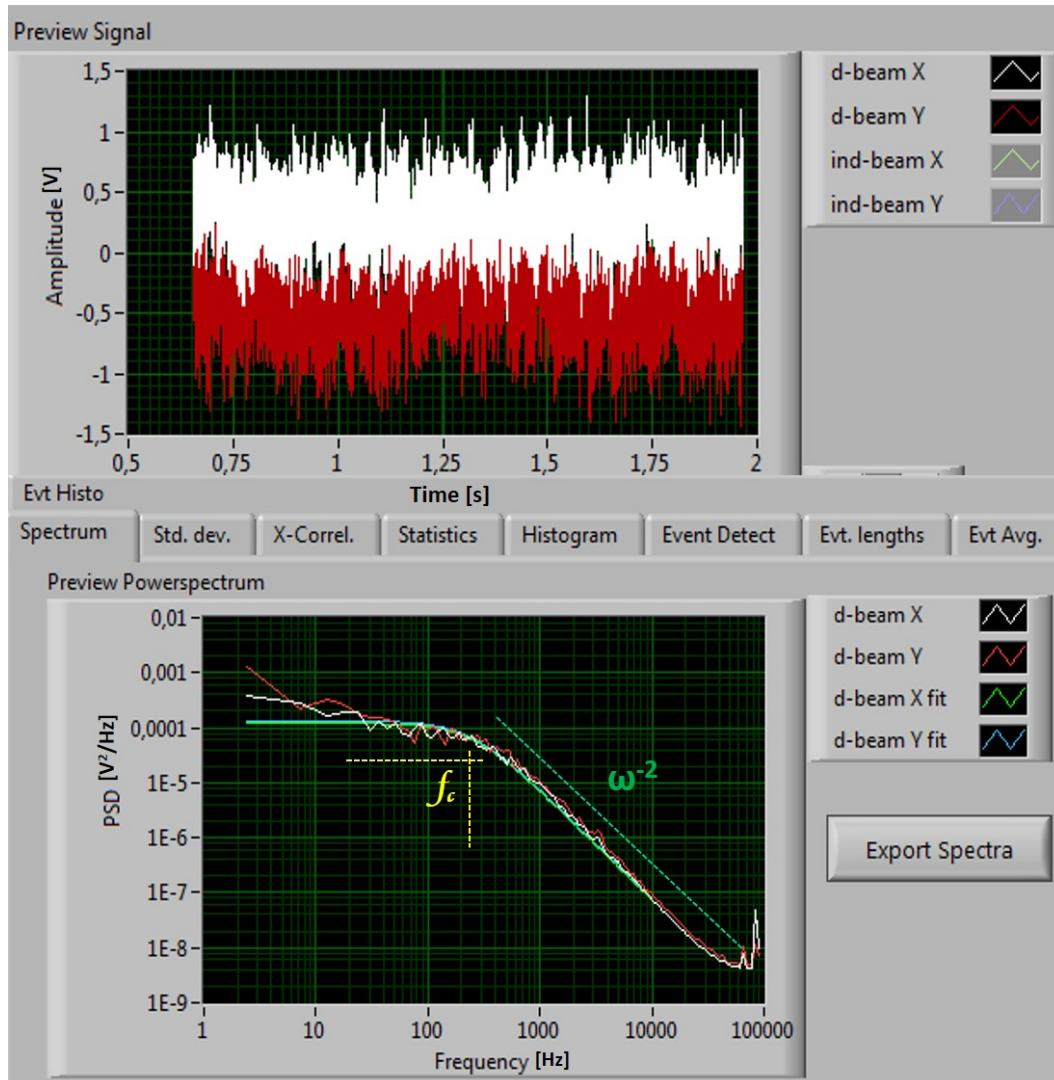


Figure 2.4.: Calibration of an optical trap using power spectrum of an embedded particle. Top panel: $4 \mu\text{m}$ trapped particle's position over time, and power spectral density (PSD) of its displacements at the bottom panel. Displacements of polystyrene trapped bead versus time, in X and Y direction by white and red color are shown on top. The lower window PSD curves (again white and red) and the Lorentzian fit (green color) are displayed. f_c is a characteristic frequency proportional to the trap stiffness. For low frequencies a plateau regime is seen, however, at higher frequencies a scaling of ω^{-2} shows up similar to free diffusion the particle. Meaning, the particle is not affected by the optical trap in short time scale. Figure shows the analyzing interface of the Labview program.

Finally with the Stokes drag coefficient, $\gamma=6\pi\eta r$, one can calculate the trap stiffness k . More detailed solution of the particle's power spectrum is described by [23], and [24].

Experimentally, after capturing two beads, based on Brownian motion of a particle in a viscous fluid (at room temperature and medium viscosity of $\eta =9.7 \times 10^{-4}$ Pa.s), we calculated the drag force applied on them to calibrate the trap stiffness and displacements. In practice, using labview program, we fit the best Lorentzian function to the bead's displacement spectrum and found the corner frequency f_c by which, the trap stiffness $k = 6\pi\eta r\omega_c$ can be calculated ($\omega_c = 2\pi f_c$), shown in Fig.2.4.

After the calibration, we let trapped particles bind to the opposite sides of a suspended cell. Depending on coating efficiency it might take 5-10 min for cells to tightly bind to protein coated beads and get ready for microrheology (MR) experiments.

2.1.4 Optical trapping set-up

For this work, we used a custom-built optical trap integrated with an inverted microscope (Fig.2.5). Trapping laser, was a near infrared solid state (Compass, Nd:YVO4, 1064 nm, Coherent Inc., Santa Clara, CA, USA) linear polarized 4 W laser, that is protected from back reflection by an optical isolator (IO-5-1064-VHP, Thorlabs, Newton, NJ, USA). Beam diameter is become 3x larger using a beam expander (Qioptic Photonics GmbH & Co KG, Munich, Germany) to the size of ~ 4 mm.

A motor-driven half-wave plate (PRM1Z8, Thorlabs, Newton, NJ, USA), together with a polarizer were used for adjusting the laser intensity, as well as keeping the stability of high laser power. A Glan-Laser polarizing beam splitter (PBS1), separated the light into two orthogonally polarized beams called direct and indirect beams. Later, they will form two individual traps in the specimen plane. Power distribution into these paths is adjustable by orientation of the input polarizer.

Beams in both paths will hit 1:1 telescope lenses (TL), functioning similar to a telescope; the beam from the focal plane of the the first TL (TL1), is imaged by second TL (TL2) on the back-focal-plane (BFP) of the trapping objective. Changing the position of the TL1 while TL2 is fixed, will change the position of the trap in the sample plane. It allows the user to steer the beam without changing the intensity.

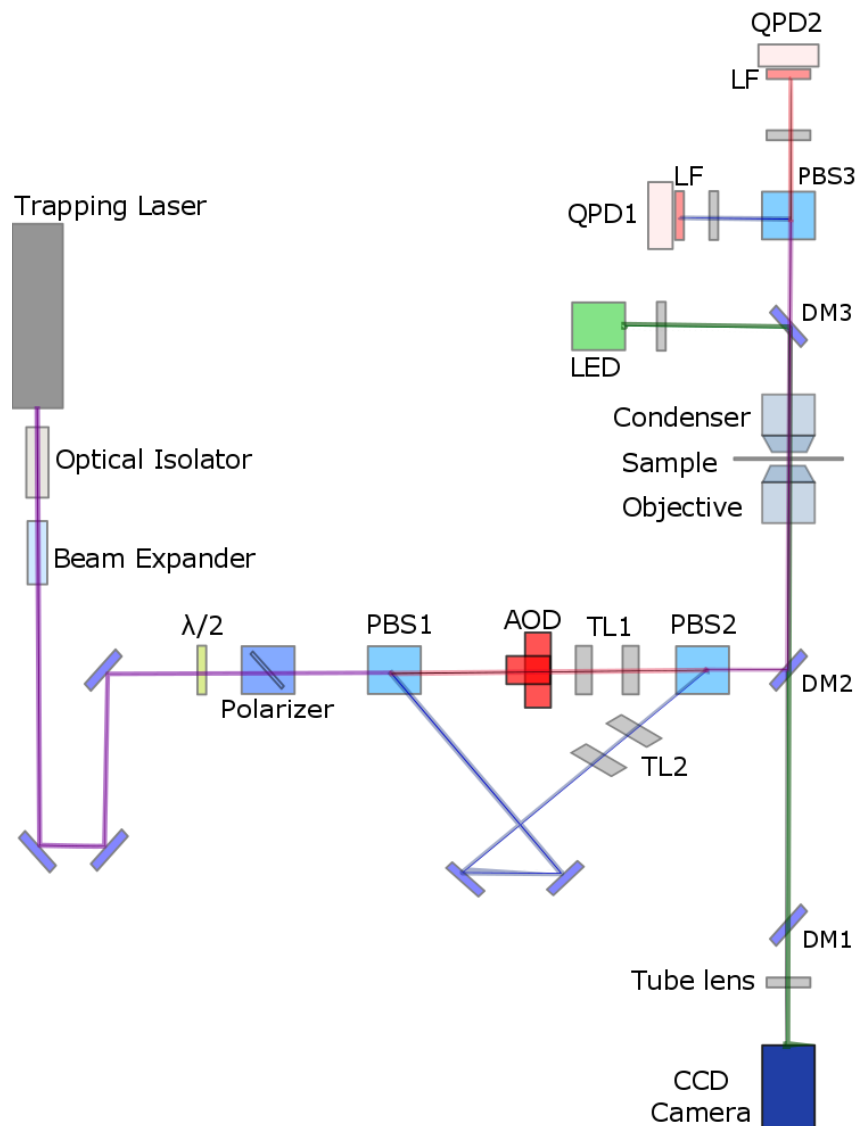


Figure 2.5.: Schematic layout of the dual optical trap set-up. A 1064 nm laser light passes through a beam expander, then a $\lambda/2$ plate and a polarizer to reach a polarizer beam splitter (PBS1) and split into two orthogonal polarization. Later, they will form two individual traps in the sample plane. Direct beam goes through an AOD for fast steering and then telescope lenses to reach the second PBS, recombined and led to the microscope via dichroic mirror (DM1). After passing through the objective, they would again split up by PBS3 and imaged onto the QPDs. For bright field microscopy, a green LED was used to illuminate the sample and image it on a CCD camera. Small blue and gray color rectangles, without labels, show mirrors and lenses, and LFs are 1064 nm laser filters.

In the direct path, before the telescope, we inserted a 2-axis acousto-optic deflector (AOD) which will be described in the following section. Two polarizations were recombined using the second Glan-Laser polarizing beam splitter (PBS2) that coupled to the microscope' objective with a dichroic mirror (DM2).

Laser light was focused on the sample with a 100x oil immersion (NA=1.3) objective (Neofluor, Carl Zeiss MicroImaging GmbH, Jena, Germany). After passing the sample, light was collected by means of a 100x condenser lens (NA=1.4) oil immersion (Carl Zeiss MicroImaging GmbH, Jena, Germany) and then again split into the orthogonally polarized beams while passing through third polarizing beam splitter (PBS3) [24].

The light from BFP of the condenser is imaged onto the quadrant photo-diodes (QPDs) for both polarized beams using another set of lens and a thin film of polarizer(LF) to clean up the signal and reduce crosstalk. In order to measure the intensity distributions in two lateral directions, QPDs are converting the photo-current to voltage.

For bright field imaging, we used green LED to illuminate the sample. It is located above the condenser and coupled to the microscope. LED light after passing through dichroic mirrors (DM) and the microscope, finally reaches the CCD camera (Coolsnap EZ, Photometrics, Tucson, AZ, USA).

Fig.2.5 represents the schematic layout of the set-up and Fig.2.6 illustrates a simple adjustment of the telescope lenses, TLs. In the following section, we describe AOD basics and operation in more detail.

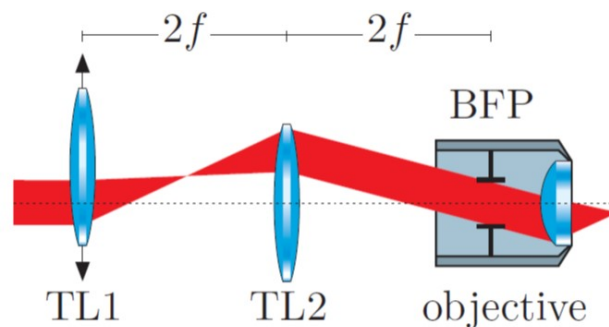


Figure 2.6.: Schematic adjustment of telescope lenses. The first telescope lens (TL1) is adjustable; its lateral displacement will change the angle of the beam and thus position of the trap in the sample plane. The second lens was kept fixed, in order to image the beam profile onto a BFP of the objective. Figure is taken from [19].

- Acousto-Optic Deflector

In this work, we used Acousto-Optic Deflectors (AODs) associated with high frequency RF drivers (MHz). Here is a brief introduction of AOD's principle, practical operation and its application to control oscillations needed for active microrheology. Appendix.B gives a short guide how to insert it into the trapping set-up with regard to opto-electronics aspects.

In 1992, Brillouin predicted the light diffraction by an acoustic wave. Ten years later, the first experimental test of this phenomena was carried out. Then the particular case of 1st order diffraction under a certain angle of incidence, in 1935, has been observed by Rytow. The laser invention has led to the development of acousto-optics and its application, mainly for deflection, modulation and signal processing. Technical progress in both crystal growth and high frequency piezo-electric transducers have brought valuable benefits to acousto-optics components' improvements.

Bragg cell is a device which has a piezo-electric transducer and a crystal such as quartz. Driving piezo transducer in the radio frequency (RF), creates an acoustic wave in the inserted crystal. It makes a particular sound wave based on periodic planes, expansion and compression of crystal' molecules in a periodic pattern. This pattern receives the incident light in a particular angle, acts as a grating; after Bragg diffraction, leads to efficient diffracted orders separated in certain angles.

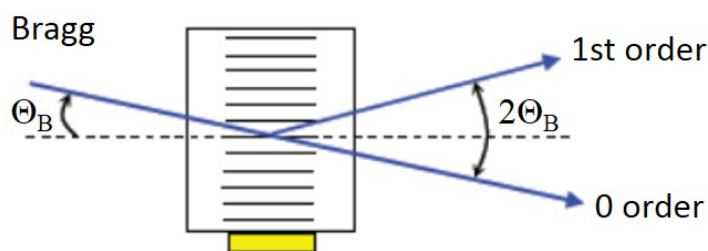


Figure 2.7.: Bragg diffraction. When the plane acoustic wave is traveling through a crystal, makes it behaves like an optical grating for an incident light. This figure shows Bragg diffraction of the light with the incident angle Θ_B that causes separation angle $2\Theta_B$ between the Zero- and 1st-order. Figure based on <http://www.aoptoelectronic.com>.

The light directly transmitted through the cell is known as 'Zero-order', while the first diffracted beam next to that, generated by interaction of light and acoustic

wave is called 1st-order. The angle between Zero- and 1st-order is known as separation angle and depends on the wavelength and the RF frequency (see Fig.2.7).

In this work, we used 2-axis XY deflectors (Fig.2.8), based on birefringent interaction in TeO₂ crystal (DTSXY-400-1064, AA OPTO-ELECTRONIC, Orsay, France). TeO₂ is the most common crystal used in AO devices for visible and infra red range (IR wavelengths). Two deflectors are mounted together on a plate, such that crystal cut is optimized for collinearity of incident and diffracted beams, when the incident ray is close to its auto-collimation axis. The consequence of two successive interactions linked to the X and Y channels, will give the same polarization as input light to the output.

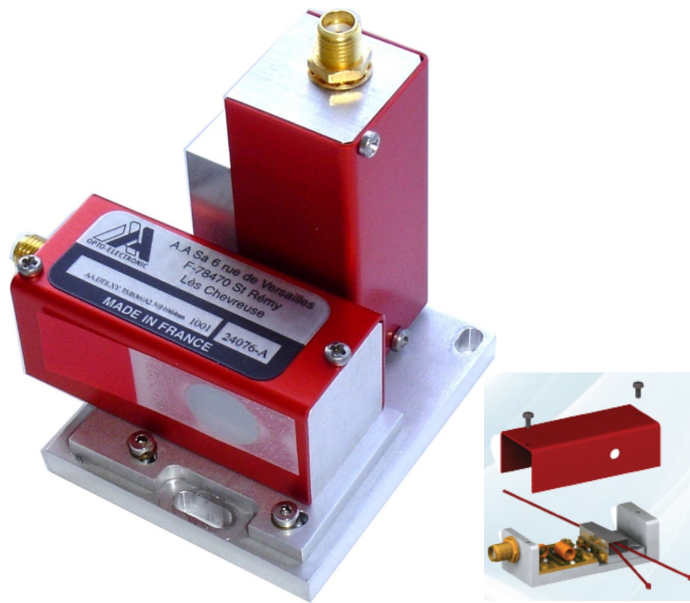


Figure 2.8.: AA Optoelectronic 2-axis AO-Deflectors. High frequency TeO₂ AODs, DTSXY-400 for 1064 nm. The (1,1) diffracted order supposed to be collimated with the incident light on the input of the crystal face. The small inset on the right shows separation between the Zero- and 1st-order. Figure adapted from the manufacturer's datasheet <http://www.aaoptoelectronic.com>.

This AOD is specified for 1064 nm wavelength and proper for a linear polarized beam with diameter of $d \simeq 1.2-6$ mm. This particular device gives just the Zero- and 1st-orders in form of 2x2 array as shown in Fig.2.9. Driving it with its central frequency 75 MHz (corresponding to an input voltage of 5 V), separation angle on each axis will be ~ 98 mrad.

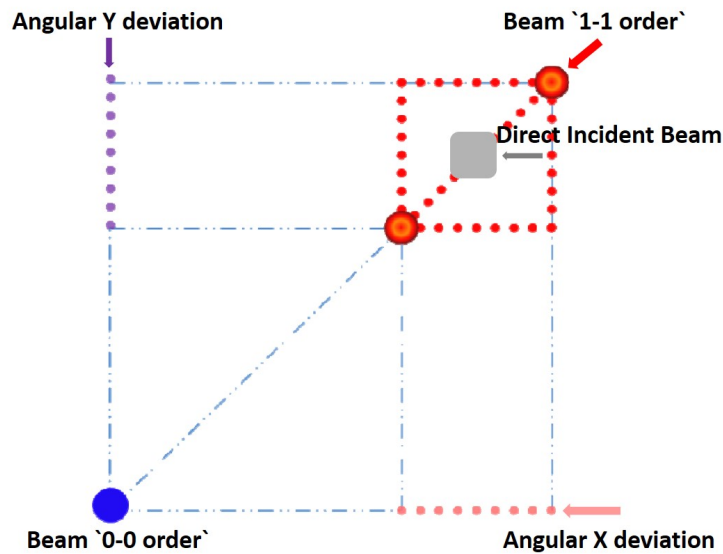


Figure 2.9.: Representation of output optical beams of 2-axis AOD. Deviation of diffraction orders while passing 2-Axis AOD gives 2x2 array outcome. Efficiency of the (1,1) order can be improved by adjusting the AOD position while measuring the intensities. Figure adapted from the manufacturer's datasheet <http://www.aoptoelectronic.com>.

- Oscillating the trapping beam using AODs

In order to operate the 2-axis AOD (DTSXY-400-1064) in our set-up, we need a radio frequency driver that can feed AODs with a proper frequency and modulation. A variable frequency driver and voltage controlled oscillator (DRFA10Y2X-D, AA OPTOELECTRONIC, Orsay, France) has been connected to AODs and operated in CW mode. According to manufacture test-sheet for 2-Axis DTSXY-400-1064 AOD, the efficiency of the module in 1-1 order with the given condition was about 70%. Knowing this, after inserting the device into the set-up, final adjustments were done by comparing the output intensity with respect to the input. For detailed adjustment see the Appendix.B.

For active microrheology, one needs to oscillate one of the trapping beams and record particle's position accordingly. We drive AOD signal on an external mode to make and control the oscillation. An external tunable power supply, is connected to a lock-in-amplifier to generate a modulated input for AOD. We chose a lock-in-amplifier (SR-830 DSP, Stanford research systems, Sunnyvale, USA) to act as a controllable signal generator with high precision in amplitude and frequency

modulation. Using SR-830, one can operate sinusoidal modulation over broad range from 1 mHz up to 100 kHz of frequency, and the amplitude from 4 mV to 5 V with a mV precision.

For our active MR measurements, slow oscillations with small amplitude was required. External power supply was set to 5 V to provide the central driving frequency of AODs. We were interested to oscillate a micron sized trapped particle with 0.2 Hz and an amplitude of < 500 nm. To this aim, first we needed the voltage-displacement calibration of the particle.

- Calibration of AOD caused movement

We imaged and recorded position of the trapped particle, driven with a certain amplitude, for a few periods. The particle, accordingly was moved back and forth. Knowing the field of view and the pixel size, we analyzed the images using ImageJ-Fiji program (ImageJ 1.48; Java 1.6.0 [64-bit]) and measured the displacements in micrometer to get the final calibration value (e.g. 14.11 $\mu\text{m}/\text{V}$). Based on this calibration factor, a voltage correspond to the desired oscillation amplitude can be calculated (e.g. 28 mV for oscillation with 400 nm amplitude).

2.2 Two-particle microrheology to probe cellular force

Microrheology (MR) is the term for a number of techniques applied to study viscoelastic properties of materials by observing the motion of the micrometer-size probe particles embedded in a material. In comparison to (macro-) rheology, viscoelasticity can be measured over a wide range of frequencies [25]. The Sample amount needed for it, is relatively small (e.g femtoliter) and additionally different size of probe particles (micro- or nano-meter) can be used [26]. Since in this range, Reynolds number is very small, inertial effects can be neglected.

The optical tweezer (OT) can be used to manipulate microscopic objects such as dielectric particles, using gradient of laser light. OT can detect displacements below nanometer (0.1 nm) and forces less than 1 pN (0.1 pN). Different modes of microrheology have been used to detect displacements of colloidal particles embedded in materials such as passive microrheology (PMR) when particle's motion is passively tracked, or active microrheology (AMR), when external forces are imposed on embedded particles and corresponding fluctuations will be recorded . Ever since microrheology (MR) had been introduced, single or multi particle

MR techniques such as video-particle tracking, magnetic and laser tweezers, have been employed to study mechanical properties of fluidic systems, as well as in bio- and polymer-physics [27]. Furthermore, correlated motions of probe particles in different time scales, can be used to investigate the material properties of non-equilibrium systems such as living cells [26].

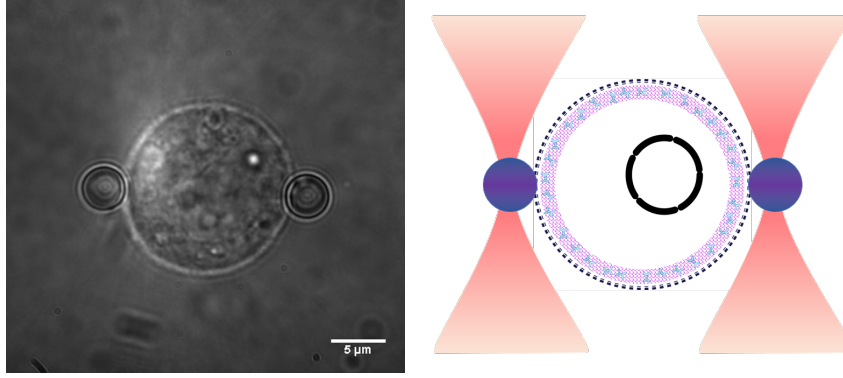


Figure 2.10.: Two-particle microrheology of cellular system using optical traps. Suspended fibroblast held by two trapped micro-beads on the left and sketch of cell suspended with gradient laser beams on the right.

In the following section, we explain how AMR and PMR can measure the force generated by a suspended cell.

2.2.1 Cellular force probed in passive and active modes

Using a dual optical trap, we measure cross correlation displacements of two dielectric (polystyrene) beads which are bound to the opposite sides of a suspended cell, to calculate fluctuations of the cellular force. Experimental configuration is shown in Fig.2.10.

Passive microrheology (PMR)

For two-particle PMR (2P-PMR), displacements of particles, $u^i(t)$ -in the direction parallel to the connecting line of two particles- will be recorded using two QPDs. Then fourier transform of their cross- correlation, $PSD(\omega)$, is measured as the following:

$$PSD(\omega) = \langle u^{(1)}(\omega)u^{(2)*}(\omega) \rangle = \int_{-\infty}^{\infty} \langle u_x^{(1)}(t)u_x^{(2)}(0) \rangle e^{i\omega t} \quad (2.15)$$

Multiplication of $\langle u^{(1)}(\omega)u^{(2)*}(\omega) \rangle$ with trap stiffness k , gives us the force spectrum. For final calculation of the total cellular force, we integrate the force over range of 0.1-10 Hz or $\Sigma_{0.1}^{10} FF^*$.

Active microrheology (AMR)

In active mode, oscillatory force with a given frequency is applied on one of the particles using an acousto-optics deflector (AOD). The QPD signals, shown in Fig.2.11, corresponding to oscillatory and the stationary traps as well as the AOD driving signal are recorded. In this configuration, when an oscillating force F_2 is applied on the second particle and u_1 is the corresponding movement of the first one, the complex response function of the system $A_{1,2}$ is given by:

$$A_{1,2} = A'_{1,2} + iA''_{1,2} = \frac{u_1}{F_2} \quad (2.16)$$

Calculation of the response function based on the fluctuation dissipation theorem (FDT) for equilibrium systems, indicates the thermal force. However, in PMR measurements, the total force exerted on the particles is taken into account.

According to (Mizuno et al.2009), 2-particle AMR and PMR for Rounded-up cells did not agree on cellular response function in low frequencies, below 10 Hz [28]. Meaning, in this range the system is not in equilibrium and apart from thermal force, there should be an active force generated by the cell. We used this fact and combine AMR and PMR to calculate the active cellular force (non-equilibrium part), which is the subtraction result of FDT calculations (thermal) from the force values obtained by PMR (total), formulated in eq.2.17:

$$\langle u^{(1)}u^{(2)*} \rangle_{non-equil} = \langle u^{(1)}u^{(2)*} \rangle_{total} - \langle u^{(1)}u^{(2)*} \rangle_{thermal} \quad (2.17)$$

From the AMR response function, using FDT, the thermal fluctuations $\langle u^{(1)}u^{(2)*} \rangle_{thermal}$ is:

$$\langle u^{(1)}u^{(2)*} \rangle_{thermal} = \frac{2k_B T}{\omega} A''_{1,2}. \quad (2.18)$$

Fig.2.12 shows both imaginary ($A''_{1,2}$) and the real part of the cell response function ($A'_{1,2}$) given by PMR and AMR, and also FDT violation in low frequencies. It is shown that real parts are roughly overlapping and the difference is mainly on imaginary parts and at low frequency range (from 0.1 to 10 Hz). The cell

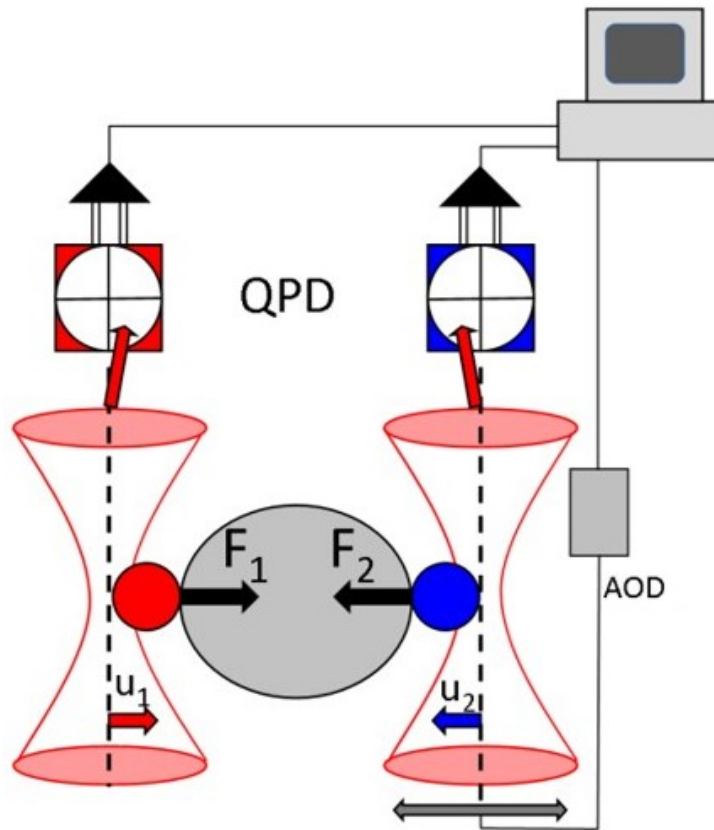


Figure 2.11.: Representation of cellular force measurement using OT. Rounded-up cell between two trapped beads, exerts force on them (F_1, F_2). Beads displacements u_1, u_2 will be detected by QPDs and recorded digitally via FPGA I/O board and Labview program. Figure is re-presented from [20].

response function given by AMR (the thermal part) is approximately zero, while PMR shows a negative value of total force. Therefore, we assume that in this range the total force is dominated by non-equilibrium part of fluctuations (eq. 2.19). The same effect has been shown for 3T3 fibroblasts in [20].

$$\langle u^{(1)} u^{(2)*} \rangle_{non-equil} \approx \langle u^{(1)} u^{(2)*} \rangle_{total} \quad (2.19)$$

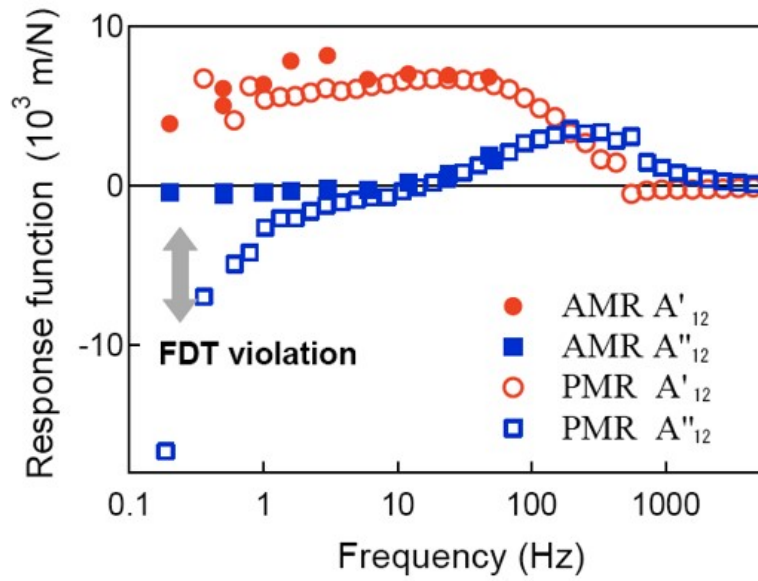


Figure 2.12.: Response function of a MLO-Y4 cell measured by AMR and PMR. Violation of fluctuation dissipation theorem (FDT) in imaginary part of the response function (squares) of a round cell in low frequencies. Circles show real part of response function measured in both active and passive modes. Figure is re-printed from [28].

2.2.2 Stiffness measurements

The optical traps play a role of an elastic environment for the cell, similar to what usually is provided by an extracellular matrix or neighboring cells. In practice, by changing the laser power, we can control this environmental conditions. (Mizuno et al.2009) modeled the cell and traps as coupled springs to approve this idea [28].

In our active measurements, oscillatory force obtained by AOD, drove one of the the particles back and forth, Fig.2.13, while the other one was kept stationary. Small amplitude of oscillations (< 500 nm) with a low frequency (0.2 Hz) was applied to be able to record the linear behavior of the cell. The center of the oscillating trap and QPD signals corresponding to displacement of particles with respect to the center of both oscillatory and stationary traps, were recorded. When the oscillating beam is moved by d , and beads are displaced by $(u^{(1)}, u^{(2)})$ from the center of the traps, in Fig.2.13, the elongation of the cell will be

$$\Delta l = d - (u^{(1)} - u^{(2)}). \quad (2.20)$$

ΔL shows the effective elongation of the cell. In a case that force-versus-elongation

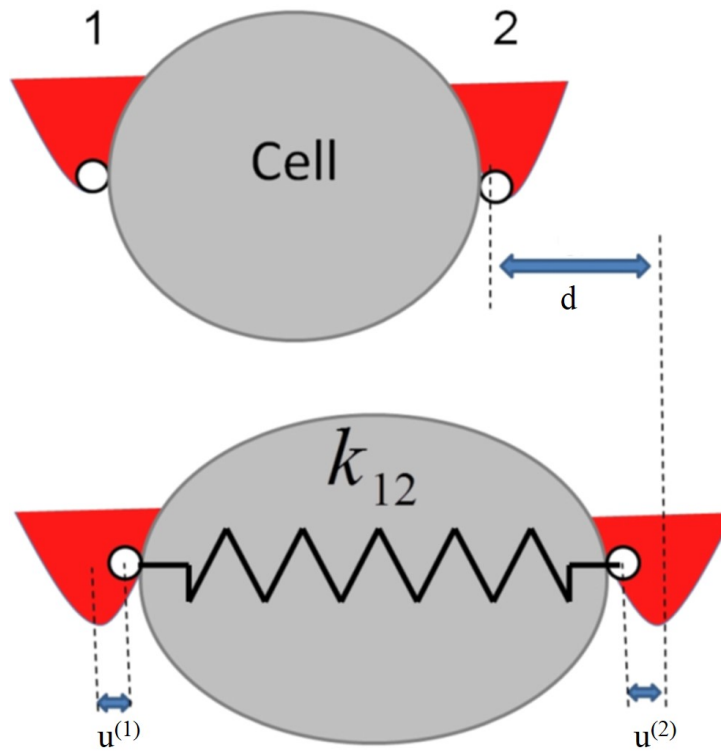


Figure 2.13.: Representation of stiffness measurement. Rounded-up cell bound to the trapped beads, each in a parabolic potential well on two sides. Stretching one of the traps using AOD, by distance d , displaces both beads from the trap centers by $u^{(1)}, u^{(2)}$. We used Hook's law to derive an effective spring constant of the cell k_{12} . Figure is taken from [20].

curve comes out linear, Hook's law for elastic spring can be used; by which the slope will give the spring constant of the cell.

$$F = -k_{cell}\Delta l \quad (2.21)$$

The force balance for this system with k as a trap stiffness and k_{12} the effective spring constant of the cell, gives the displacements of probe particles.

$$u^{(1)} = u^{(2)} = -\frac{F}{(k + 2k_{12})} \quad (2.22)$$

Real measurements of cellular stiffness is presented in the following section (Fig.2.15).

Finally, one should know that the measured force based on probe particle' dis-

placements, $k^2 \langle u^{(1)}u^{(2)*} \rangle$, is the force transmitted to the particles. According to (Mizuno et al.2009), however, when F denotes the total traction force between probe particles in this configuration, the total force fluctuations $\langle FF^* \rangle$ is related to the transmitted force by:

$$-k^2 \langle u^{(1)}u^{(2)*} \rangle = -\frac{k^2}{(k + 2k_{12})^2} \langle FF^* \rangle. \quad (2.23)$$

This means higher forces will be transmitted to probe particles, when traps are stronger (larger k).

Nevertheless, assuming that the prefactor $\frac{k^2}{(k + 2k_{12})^2}$ does not have a big impact, what is measured and presented in this thesis is the transmitted force.

2.2.3 Representative force measurements

In this section, some examples of our typical measurements, based on given explanations up to this point, are presented. In the next chapters we only show and discuss about the evaluated results based on these fundamental steps.

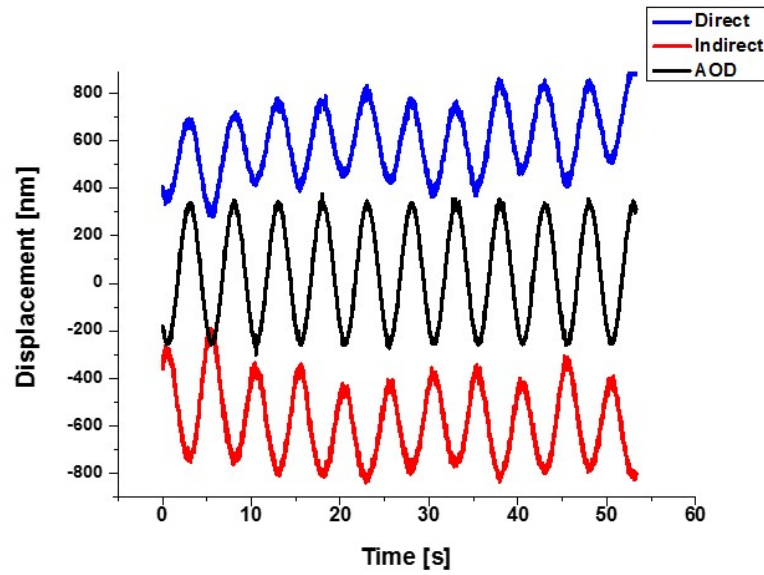


Figure 2.14.: Representation of time-course particles' displacements in Active MR. When AOD is oscillating the center of the direct beam (black curve), corresponding trapped particle is following (blue curve). Simultaneously, the position of the second particle in the stationary trap is recorded (indirect beam, red curve). Displacements from the center of the traps are shown on vertical axis when the driving frequency was 0.2 Hz.

First, recorded amplitudes in an AMR experiment are demonstrated in Fig.2.14. A MCF-7 cell is held by $4\mu\text{m}$ fibronectin coated polystyrene beads. Using the AOD, one of traps is oscillating with 300 nm amplitude and 0.2 Hz frequency. Position of the AOD-steered trap, as well as displacements of particles from the center of corresponding traps are shown, by which later we calculate the cell elongation.

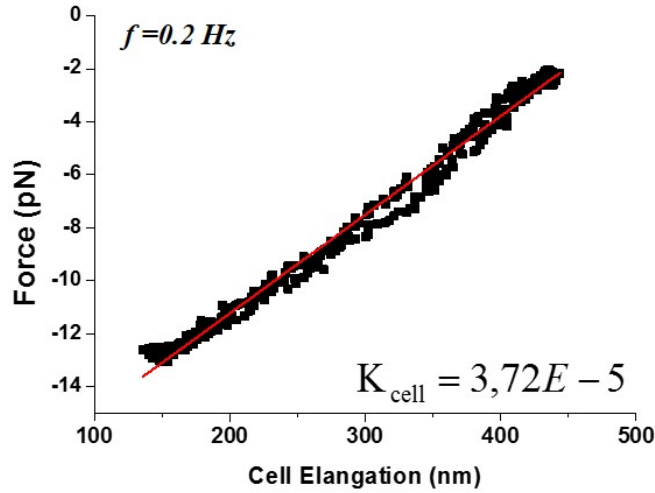


Figure 2.15.: Representative measurement of cell stiffness. Force versus elongation of a rounded-up MCF-7 cell, measured in simple active mode, when oscillation frequency is 0.2 Hz, and deformation amplitude $<500\mu\text{m}$. Using Hook's law $F = -k_{\text{cell}}\Delta l$, slop of the linear fit (red curve), gives the cell stiffness K_{cell} .

Fig.2.15 represents the force-elongation measurement of a MCF-7 cell, probed with the optical trap in the active mode (AMR). The stiffness is calculated based on Hook's law (eq. 2.21).

Apart from AMR, we can record fluctuations of the force transmitted to each of trapped particles. Fig.2.16 depicts how MCF-7 cell exerted force $F_i = k \cdot u_i$ on beads attached to its sides, for a period of 6 minutes.

Finally, in the last graph of this section (Fig.2.17), for MCF-7 cells, we have seen a ω^{-2} power-law behavior in the power spectral density of forces. This is consistent with the previous work of (Mizuno et al.2009) [28]. Stronger traps (higher k) increases the transmitted force to the trapping particles. It is important not to confuse between this ω^{-2} scaling and the diffusion in purely viscous environment

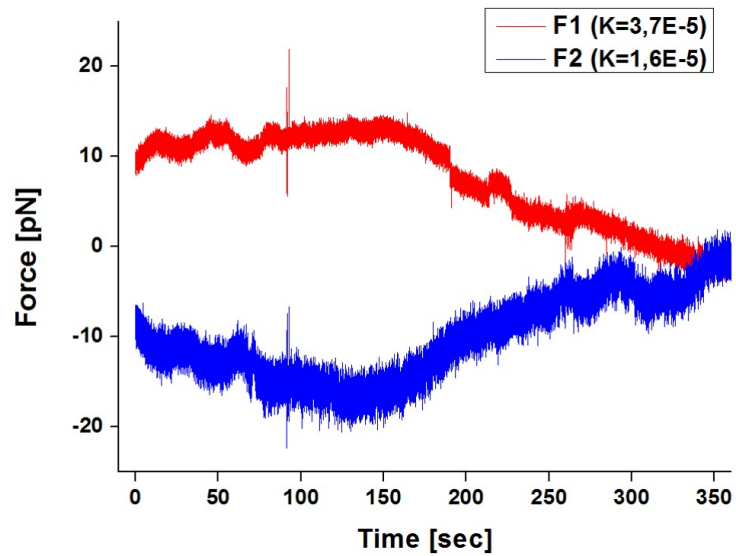


Figure 2.16.: Representative measurement of cellular force. Long term force fluctuations on probe particles in both sides of a MCF-7 cell, F1, F2. Force generated by the cell result in anti-correlation displacements of particles (legend unit $[N/m]$).

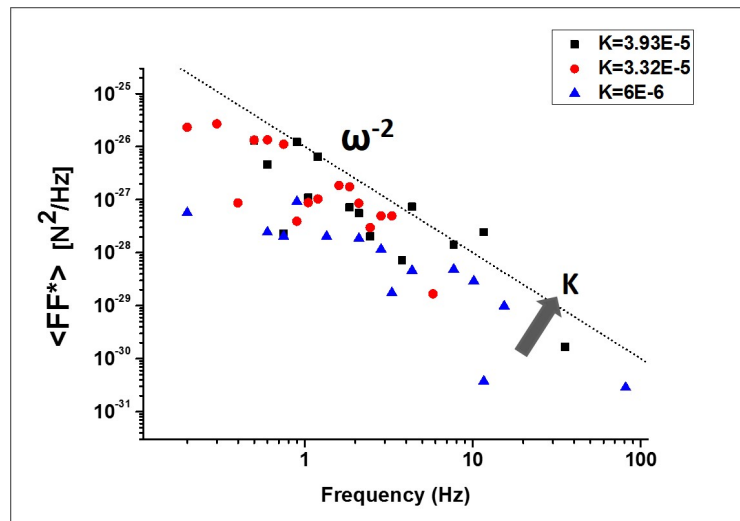


Figure 2.17.: Frequency dependence of cellular force fluctuations. Power spectral density of force, $k^2 \langle u_1 u_2^* \rangle$. In high trap stiffness it follows an ω^{-2} power-law indicated by the dash line. The arrow shows the direction of larger value for K (legend unit $[N/m]$).

(causing the same power-law behavior), since here ω^{-2} shows up due to the non-equilibrium force fluctuations in cellular systems.

2.3 Materials

2.3.1 Cell culture

In this work, we used three different cell lines: 3T3 NIH fibroblasts, MCF-7 and L-1210, all were taken from DSMZ (Braunschweig, Germany).

NIH-3T3 (ACC 59) mouse embryonic fibroblasts, naturally adherent cells, were cultured in Dulbecco's modified Eagle's medium (DMEM) (D6429, Sigma-Aldrich, St. Louis, MO, USA) with 10% fetal bovine serum (FBS, # F0244, Sigma-Aldrich) and 1% penicillin-streptomycin (# 17-602E, Lonza, Basel, Switzerland) in 75 cm² culture flasks (83.1813, Saarestedt AG, Numbrecht, Germany) at 37 °C and 5% CO₂. For culturing, cells were grown up to a confluency of roughly 80% and passaged into new culture flasks using 0.05% trypsin (59417C, Sigma) every 2-3 days with a density of ~150000 cells per flask.

In order to do force measurement experiments, suspend cells were needed; so, cells were trypsinized for 3 min at 37°C, followed by adding DMEM (supplemented with 10% FBS) and then 5min centrifuging on 1000 rpm. Finally, the cell pellet re-suspended in the CO₂ independent medium (18045-054, Life Technologies, Darmstadt, Germany), again with 10% FBS, were ready for the experiment. Cells could be kept in ice and used up to 7-8 h.

MCF-7s (ACC 115) human breast adenocarcinoma, also adherent cells, were cultured and prepared for the experiment the same as NIH-3T3s. Care had to be taken that they needed high-sugar culture medium and their population density on the culture flask was important. High Glucose (4,5 g/l) DMEM (D6429, Sigma-Aldrich, Germany) was used and every new passages had at least 0.5-0.6 million cells per flask.

L1210 (ACC 123) mouse leukemia, lymphoblast like cells grow naturally in suspension (see <https://www.atcc.org/Products>). We grew them in DMEM (D6429) medium. For culturing, without a need for trypsinization, directly after 5 min spinning down with 1000 rpm (162 xg), and re-suspending ~100000 cells were put into new 75 cm²-flask and the rest could be taken in 15 ml falcon tube (in ice) for the experiment (also up to 7-8 h). As they are relatively fast, every 1-2 days

they have to be split to 3 or 4.

- Biochemical inhibitors and sugar solutions

For the drug perturbation experiments, either 100 μM blebbistatin (racemic mixture, 203389, Merck, Darmstadt, Germany) or 20 μM Y-27632 (Y0503, Sigma-Aldrich, Germany), were prepared [29],[30].

All solutions had been made fresh and put in a test tube. According to the experiment, it was used directly in the case of single cell experiment in the microfluidic chamber, or it was incubated for $\sim 20\text{-}30$ min together with cells for conventional OT measurements in cover-slip macro-chamber. In the first case we wanted to have a time lapse recording from the moment drug starts diffusing in the channel containing the cells.

For osmotic pressure experiments, we made different concentrations of D-Sorbitol (S1876, Sigma-Aldrich, Germany) in CO_2 independent cell medium supplemented with 10% FBS. Again freshly made solution is highly recommended, specially because bacteria grow in sugar solution very fast. Care has to be taken that all drug and sugar solutions have to be filtered prior to infusion into the micro-channels.

- Transfection

For confocal fluorescence microscopy of NIH-3T3 cells, we used electroporation (4D nucleofector unit, Lonza, Basel, Switzerland), to directly transfer genes into the cell. After trypsinization and centrifuge, ~ 1 million cells were resuspended in the desired transfection buffer (SE buffer Kit L (24RCT), V4XC-1024 KT, Lonza). We used plasmid DNA for non-muscle-myosin heavy chain IIa GFP (from R.Adelstein, Addgene plasmid # 11347) to label non-muscle-myosin-IIa, and pmaxGFP Vector (SE kit, Lonza) for general (non-specified) fluorescent labeling (both in green). These vectors were transfected to a total amount of 3 μg in the sample when the cell solution was put into transfection vessels and mounted for nucleofection (4D Lonza unit) under the program CA137. After 5 min incubation, 100 μl of pre-warmed cell medium was added and later put into a culture flask.

2.3.2 Materials and working solutions

In this section, we describe first micro-particles (beads) which was used for MR experiments. Second, the chambers that have been used exclusively for three different experiments. Lastly, preparation of cells and beads mixed suspensions is presented.

1) Beads

4 μm polystyrene carboxylated beads, coated with fibronectin protein was used for 2-particle MR, in order to bind to the cell. As it's a protein commonly found in extra cellular matrix of adherent cell [31],[32], we expected NIH-3T3 and MCF-7 cell bind to them relatively tight. Coating protocol will be found in Appendix.A. Based on a coating efficiency, it may take 5-10 min for 3T3 cells to adhere, while MCF-7 were faster (3-4 min) but their contact area grew larger over time. This perhaps is due to their tendency for being attached in a polygonal form. Nevertheless, fibronectin (F-0895, Sigma-Aldrich) coated particles did not stick to L-1210 spherical shape blood cells. Simply saying, suspended blood cells are not meant for sticking. After several trials it turned out that Poly-L-Lysine (P4707, Sigma-Aldrich) a positively charged flexible molecule which is known to facilitate the attachments of cells and proteins on solid surfaces, binds strongly to these cells [33] ,[34]. Electrostatic interaction between the negatively charged membrane of L-1210 cells and the positively charged Poly-L-Lysine (PLL) coated beads, is the reason for this behavior (see PLL coating protocol in Appendix.A) [35][36].

2) Chambers for suspended cells

In this work we used three different types of chamber for suspended cells imaging or microrheology: conventional macro-chambers, ibidi μ -slides and our novel micro-chambers. The important point was how to keep the cell suspending all along the experiment, without adhering to the chamber's surfaces .

The first type was the conventional flow chamber, essentially applied for microrheology (in bulk cell studies), simply made of a coverslip, double-stick tape and a microscopy glass slide. In order to prevent cells and beads sticking on the glass surface, we coated cover-slips with Dichloro-dimethyl-silane (DDS). Using this silane compound in liquid form (40140, Sigma-Aldrich), we made their sur-

faces hydrophobic. After infusing cells and beads in flow chamber, in order to prevent medium drought, vacuum grease or nail polish sealed the chamber. DDS coating procedure is explained in Appendix.A.1.2

. Second, for cell volume measurements and fluorescent confocal imaging, we used ibidi uncoated μ -chamber (80111 uncoated μ -Slide, ibidi GmbH, Martinsried, Germany). As it is manufactured from hydrophobic plastic, it did not need any further treatment. This plastic also has a high optical quality which exhibits very low birefringence and autofluorescence (see <https://ibidi.com/channel-slides>). The last but the most important one, the new flow chamber extensively used in this thesis, was a custom-designed microfluidic device made of NOA-81 with integrated hydrogel micro-windows. A comprehensive description of the device, requirements, fabrication and its characteristics is given in next chapter.

At the end of this chapter, we discuss about sample preparation exclusively for microrheology measurements of single cells inside our new micro-chamber.

3) Cell and bead mixed suspensions

Required population density of beads and cells (per volume) is changing from macro- to micro chambers. A general instructions for preparation of these mixtures is given in appendix A.2., where an initial estimation of concentrations for MR experiment in conventional coverslip fluid macro-chamber is presented. Indeed, regarding the type of experiment and its duration, some population optimization is required.

When it comes to micro-channel, geometrical aspects become important, as well as particles and cell's velocity. In this case, the chamber volume is at least a few 100 times smaller than macro-channels and particles are relatively faster ($\sim 50 \mu\text{m/s}$). Thus it is necessary to increase the cell density (hundred times higher for the same probability of catching cells), but simultaneously one should be careful not to crowd the sample since it increases the risk of channel clogging or unwanted particles coming toward both traps.

In the following, we describe extensively the micro-fluid chamber preparation and corresponding solutions requirements.

- Working solutions and microfluidic chamber preparation

We use a custom-designed microfluidic device made of NOA-81 integrated with

hydrogel micro-windows. We rapidly change solution conditions for suspended cells held by optical traps without direct fluid mixing. In the next chapter, we show how diffusion of the molecules happens through the hydrogel windows (Fig.3.20). The configuration of the micro-device and particularly the hydrogel membrane, helps to record time-dependent mechanical responses of individual cells under different treatments. Fig.2.18 demonstrates the real and schematic view of the rounded-up cell, held with trapping particles in a micro-chamber.

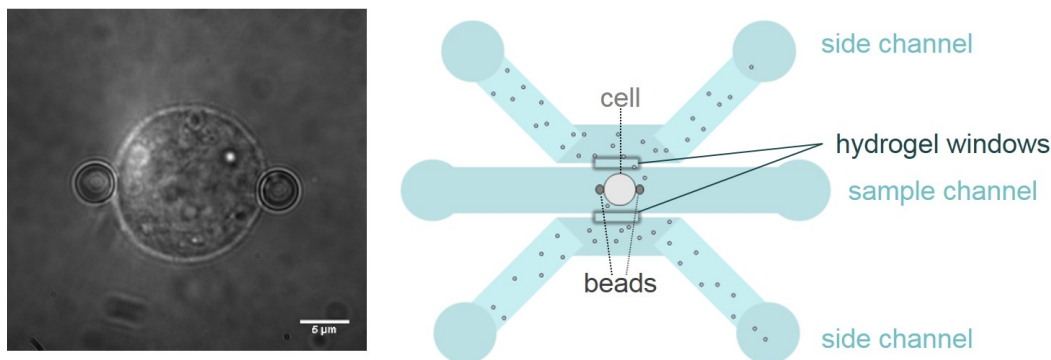


Figure 2.18.: Two-particle microrheology in a microfluidic device. Suspended fibroblast held by two trapped micro-beads on left and a sketch of a cell suspended in the flow chamber while molecules are diffusing through the hydrogel membrane windows.

Regarding the risk of biochemical contamination, bacterial growth and not-well-dissolved molecules in the micro channels, using freshly made and filtered solutions is highly recommended. $0.2 \mu\text{m}$ pore sized filters (Minisart syringe filter, Sartorius, Gottingen, Germany), were used in this work.

In order to re-use the chamber, it has to be washed carefully with IPA and then with deionized water for 10-20 min to make sure that nothing clogs the channels or sticks to the surface.

The next step, is to fill out all three channels with the CO_2 independent medium of the cells. Infusing the solution inside the channels is done with the aid of compressed air (see 3.2.3). Applied pressure has to be very low (0.1- 0.2 bar) to gently push the cells inside otherwise, cells will deform while entering and pass through the channel with a high velocity.

Gradually air pressure has to vanish while having enough cells and beads inside the sample channel. Then using soft tubings and paper clips, all three channels

will be closed.

In order to start the MR experiment, initially we measure the force and stiffness of the cell without drug perturbation (cell in closed channel). Then we carefully open the outlet of side-channels and connect their inlets to tubes containing the inhibitor solution (15 ml falcon tubes) and again apply a very mild air pressure to infuse them through. Since the sample channel is closed, therefore, there is no new flow through it. However, the solutions with a constant flow rates are running through the side-channels. Due to diffusion of molecules through the hydrogel, within a few seconds the final concentration of medium in all the channels will become equal (in the case that both side-channels contain the same solution).

The cells probed in our micro-device are mostly NIH-3T3 fibroblast, as we found them easier to lift with fibronectin coated beads (in comparison to L-1210 and MCF-7 in our micro-device) with a lower tendency to stick to the surface. Cells and beads preparation for MR inside the micro-chamber is similar to conventional cover-slip chambers (Appendix.A.2), except the density that is mentioned above. Initially, a solution with high population density for both cells and beads was provided. Then populations by adding more cells or beads, or by diluting with culture medium, were optimized. Care has to be taken that, sonication of beads before mixing in cell solution is important since their accumulation in a cluster-form can clog the channel.

Microfluidic chamber for manipulation of suspended cells

“Good design is obvious. Great design is transparent.”

Joe Sparano

3.1 Introduction

Microfluidic devices are increasingly used for biophysical studies, for example in X-ray studies to probe protein structures [37] or for optical stretcher experiments designed to investigate cell viscoelasticity [8]. A major advantage of microfluidic devices for cell biophysics applications is the ability to manipulate fast movements of solutions in micro-channels; formation static or dynamic environmental changes and generating sub-cellular scale of physical and chemical changes to trigger the fast response of the cells, with low reagent consumption is facilitated by these devices [38].

Microfluidic stickers are recent kind of microfluidic devices constructed using UV-

curing optical glue. They are relatively cheap devices that have been presented to facilitate device making in the lab and are suitable for culturing cells and tissues [39], [40]. Although it is an effective method for adherent cells, dealing with suspended cells is still challenging. By introducing hydrogel integrated microfluidic stickers, we have opened a new approach to facilitate handling the suspended cell.

This chapter mainly focuses on a versatile micro-device, with a three channel configuration which gives an opportunity for temporal and spatial control of the local concentrations in a microfluidic device. To this end, microfluidic stickers made of Norland Optical Adhesive, NOA-81, are developed. Using scanning confocal microscopy for optical projection lithography, we perform photopolymerization and fabricate hydrogel membrane micro-windows. These micro-windows act as barriers for side fluid flow. However, they are permeable to small solute and solvent molecules.

The microfluidic device is designed such that a rapide change of solutions in each individual channel is possible without direct mixing. This results in a localized concentration gradient. The functionality of the hydrogel micro membrane integrated in such a flow chamber, together with low-cost, quick and simple fabrication has inspired us to introduce it for the first time in biophysical studies. Our subject of study is suspended eukaryotic cells. As fluid velocity in the channels is controllable, we can dynamically follow individual to dense populations of cells in a closed chamber. The cells under investigation are inserted in the micro-channels and hold in place with optical tweezers. We apply mechanical and biochemical stimuli and investigate their mechanical responses. We expose cells to different osmolytes, or biochemical drugs that arrive and interfere with the cells after diffusion. Force fluctuations and stiffness of the cell are measured upon performing *passive* and *active* microrheology, respectively.

Indeed, the device is developed such that investigation, imaging and tracking of living cells under different environmental conditions is possible. A main advantage of this micro-device is to probe single cell behavior over time; before, during and after imposing biochemical/mechanical stimuli, as well as observing changes in their mechanical properties during their recovery period.

In the next chapters, cell responses to osmotic pressure as the mechanical and cellular inhibitor compounds as the biochemical stimuli are discussed.

3.1.1 Microfluidic stickers; NOA-81 rather than PDMS

The UV-curable optical adhesive NOA-81 (Norland products Inc. Cranbury, New Jersey, USA) is a versatile liquid photopolymer for low-cost microfluidic chip production [41]. Compared to polydimethylsiloxane (PDMS), the most widely spread polymeric material for microfluidic channels, NOA-81 is, entirely transparent and non-scattering in the visible range (refractive index of 1.56). It is mainly used for fast bonding of optical components and fiber optics. Additionally, its low fluorescence and high transmission in the near UV range (Fig.3.1), makes it an ideal adhesive for our device.

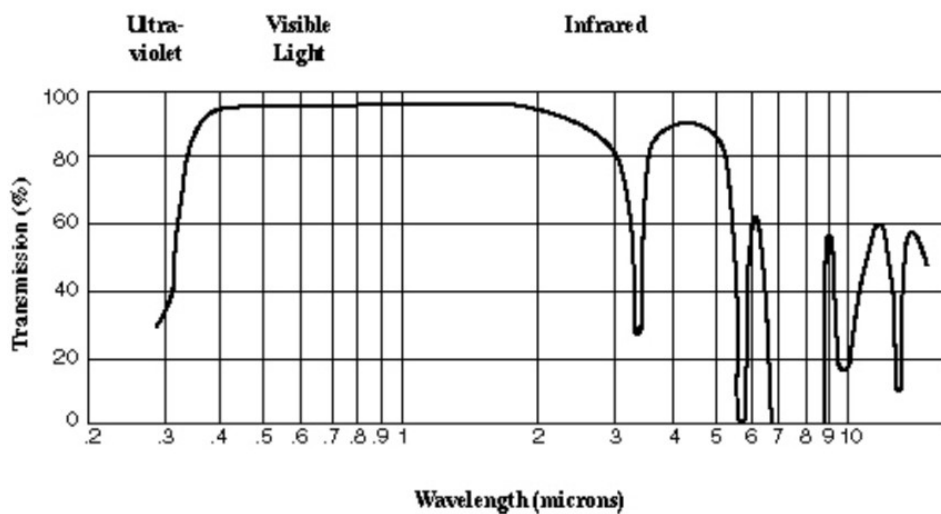


Figure 3.1.: NOA-81 Transmission Spectrum. NOA-81 transmits the near-UV light. Adapted from [42].

In addition, better chemical resistance to organic solvents, impermeability to oxygen and water vapor, persistence against swelling upon contact with fluids, and enhanced stability regarding surface treatments (e.g. oxygen plasma), makes it remarkable [41],[43]. A droplet of NOA-81 in exposed to the UV light, cures within a few seconds to a hard elastic polymer. The peak of sensitivity is around 365 nm and curing time depends on light intensity and thickness of the droplet that has been applied. Longer curing time is required for thicker films to allow UV light to penetrate to the full desired depth [42].

An exceptional advantage of NOA-81 resin is its high Young's modulus (1 GPa), that allows for channels with a large aspect ratio design while still maintaining sharp rigid upright walls. After curing, it shows very good adhesion to glass,

metal or plastic without any swelling or leakage due to aqua solution for up to a few months. This is still problematic for PDMS based devices [39]. It is explained in the next sections that channels will be tightly sticking on a glass cover slip.

3.1.2 Device configuration

A three channel micro-device configuration (Fig.3.2) with a sample channel located between two side channels is a pragmatic design in order to generate localized gradient concentration as well as a symmetrical diffusion profile introduced from side-channels through the sample channel. Neighboring channels are connected via an opening window in the wall, where a hydrogel membrane will be fabricated. So we are able to rapidly change the solution flowing through each channel individually. Channels are fabricated with 150-300 μm width, 50 μm wall thickness, 50x100 μm rectangular windows and up to 4 cm length (Fig.3.2).

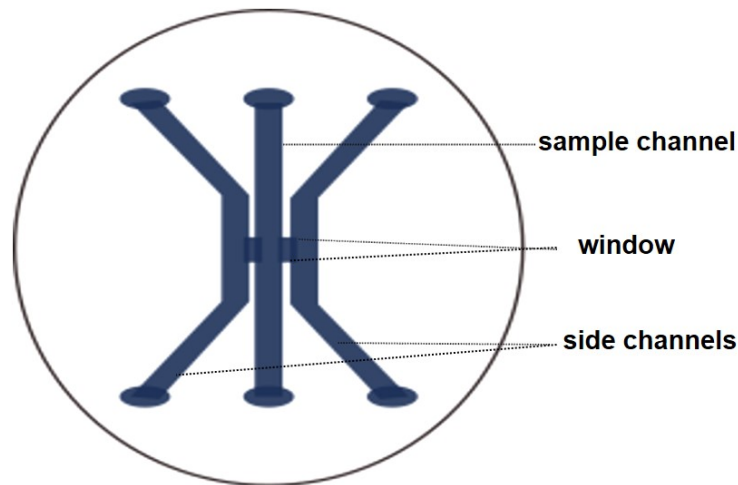


Figure 3.2.: Schematic configuration of micro-device on a 2–inch silicon wafer. Two side channels are connected to the sample channel in the middle via open windows in the wall. All are designed with the same width of 150 μm , 50 μm wall thickness, 50x100 μm windows.

In principle, a fluid flow can be characterized by the Reynolds number which is the ratio of inertial and viscous forces given by:

$$Re = LV\rho/\mu \tag{3.1}$$

where L is the relevant length scale, V is the average velocity of the flow, μ is the fluid viscosity and ρ is the fluid density. Thus one can predict the flow pattern in different fluid situations like laminar or turbulent flow.

For laminar flow, defined when $Re < 2000$, viscous force is the key player and inertial force is negligible. Fluid particles move along smooth streamlines and energy loss is mainly a consequence of viscous effects. However, in a regime with high Reynolds number the inertial forces dominate. When $Re > 2000$, particle movement will show irregular streamlines due to unsteady flow. Because of the small length scales L in microfluidic devices, Re is smaller than 1. So in this regime, flow is completely laminar and no turbulence occurs [44].

For a rectangular channel, L will be 4 times the cross section area. For instance, in the case of water with a relative velocity of 1 mm/s in our particular microdevice with a cross section of $40 \times 300 \mu\text{m}^2$, we get $Re \leq 0.8$ resulting in a laminar flow inside (density and viscosity of water is 1000 Kg/m^3 and 0.001 Kg/(m.s) respectively).

3.1.3 Photo-polymerization of hydrogel membranes

Photo-polymerization can be considered as a new generation light lithographic technique. In order to fabricate hydrogel membrane micro-windows (HMM) in the microfluidic device, photo-lithography is used.

Lithography is a process used to transfer a pattern onto a substrate. Historically it has been known as the heart of integrated circuit (IC) fabrication. Various methods like optical lithography, X-ray, electron and ion beam lithography have been used, each with different purposes. Practically a photo sensitive compound called photo-resist is exposed to radiation, which in traditional methods, changes the solubility of the photoresist in a particular developer solution. However, photo-polymerization which is a light-activated reaction of monomers to an UV-light crossed-linked polymer structure, recently became popular. Minimum feature resolution, depth of focus, photo-initiator, photo-resist response, light source, oxygen contribution and sample thickness are the key parameters in photo-lithography (see Fig.3.3).

In the following, a brief introduction to each of these parameters is given, followed by a short instruction on how to chose suitable values for these parameters.

- 'Resolution' denotes the smallest feature size of a given pattern which projection system can print faithfully, so can be resolved;

$$l_m = k_1 \lambda / NA \quad (3.2)$$

where NA is the numerical aperture of a lens, λ wavelength of the used light

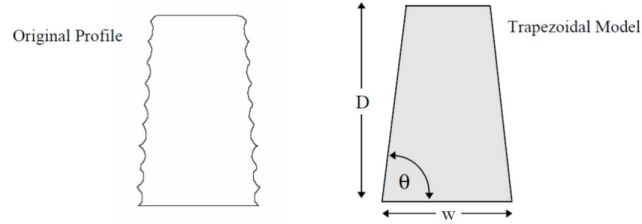


Figure 3.3.: Actual photoresist profile in comparison to its trapezoidal model. Line-width or sidewall angle can be optimized by parameters mentioned in text. This figure is adapted from [45] .

and k_1 a constant between 0.25 and 1, depending on optics, resist and process latitude.

- Depth of focus (DOF) is the range of focus error that still gives an acceptable lithographic result. It shows how much the resist plane can be displaced while specifications of the result feature (e.g. line-width and sidewall angle), appear sufficiently sharp (Fig.3.4) [45],[46],[47].

$$DOF = k_2 \lambda / (NA)^2 \tag{3.3}$$

where k_2 is a process related constant between 0.5 and 1, and depends on k_1 .

A smaller resolution and larger DOF is desired but resolution is improved at the expense of DOF.

Since we do not have very fine structure to resolve, but instead relatively deep channel designed for a high hydrogel wall, we can work with higher DOF using a low NA objective. More details will be described at the end of this section.

- Light source

In optical lithography, the UV radiation is used as the light source; traditional light sources like 'Mercury arc' lamps can provide I, G, H bands with 365, 405, 436 nm respectively, but for higher frequencies these lamps are not suitable (Fig.3.5). Alternatively, UV lasers and excimer lasers for deep UV range (up to 250 nm) are the most commonly used ones.

- Photo-initiator

Photo-initiated polymerization became a popular technique for hydrogel formation *insitu*, owing to its tractable temporal and spatial resolution [49]. There are

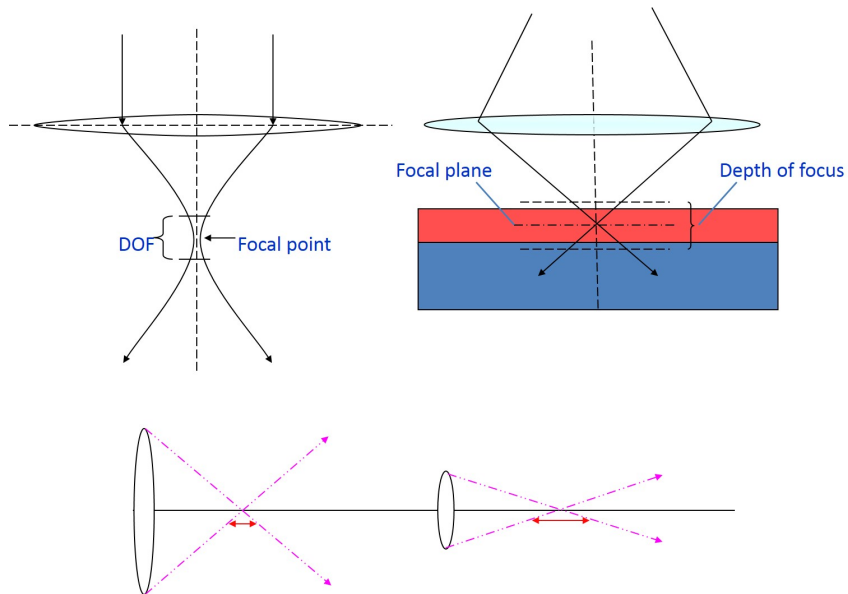


Figure 3.4.: Light projection depth of focus. Top panel depicts the focal point of a lens and the depth of focus (DOF), the range in which an image is in focus and clearly resolved (on left). On right hand side, the light focuses in a layer of resist or polymer on top of the coverslip. The bottom panel, large NA lens results in small DOF, and small NA lens is shown with a large DOF [48].

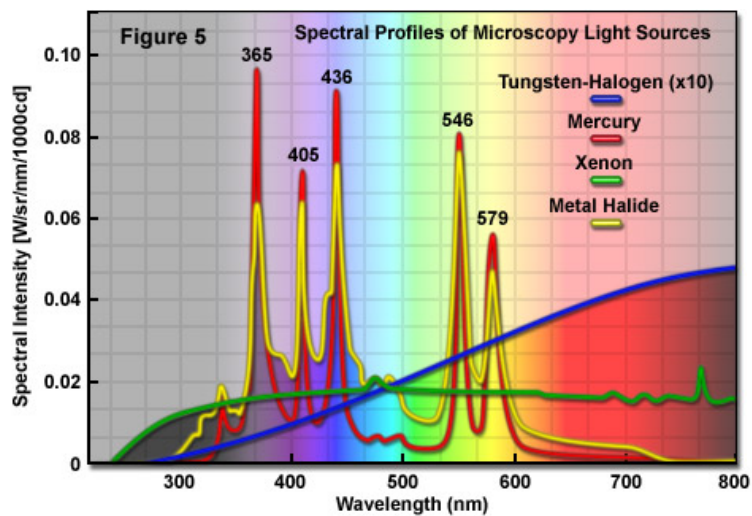


Figure 3.5.: Mercury arc spectrum. Mercury arc can provide 365, 405 and 436 nm lines useful for photo-polymerization. Figure is taken from [http : //zeiss – campus.edu /lightsources /lightsourcefundamentals.html](http://zeiss-campus.edu/lightsources/lightsourcefundamentals.html) .

many photoinitiators that have been characterized for polymerization based on the illumination wavelength. One has to compromise on illumination intensity

and photoinitiator absorption spectrum to get the best for both resolutions. Also volume ratio of initiator in photo-curing solution has been proved to vary the HMM thickness as well as its pore size [50].

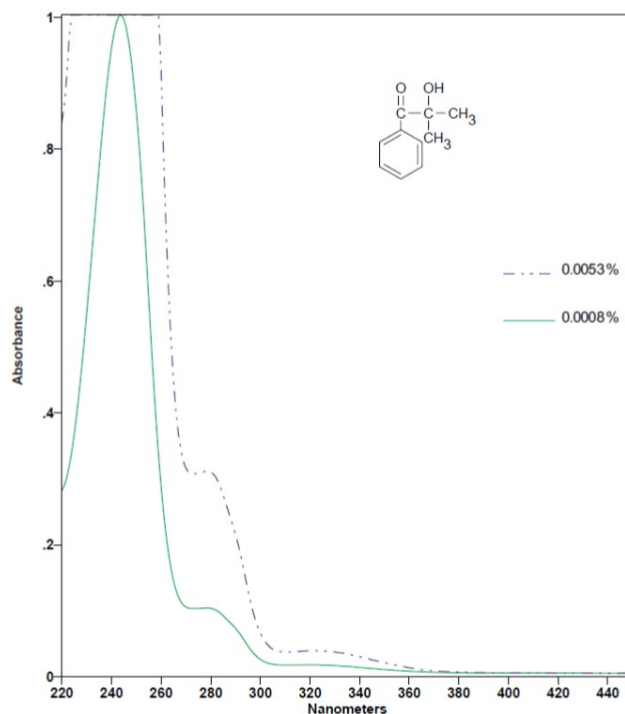


Figure 3.6.: Photo-initiator UV absorption spectrum. 2-Hydroxy-2-methylpropiophenone absorption spectrum (absorbance vs wavelength). Chemical composition is shown on top right. The spectrum is taken from <https://www.sigmaaldrich.com/GeneralInformation/photoinitiators>.

In order to obtain reliable, fast and reproducible polymerization, the gelation rate of photo-initiator has to be considered.

- Hydrogel

Polymerization of PEG-diacrylate, with both wavelengths of 365 and 405 nm has been tested. Chemical composition and concentration (volume ratio) of photo-initiator and intensity of UV light will change the gelation time [49].

Hydrogel membrane micro window (HMM) fabrication principles and characteristics have been introduced by [50]. Poly-Ethylene-Glycol-diacrylate (PEG-DA) as a UV polymerizable solution together with photo-initiator fills up a three channel micro-device. The device has the same design as Fig.3.2. Connecting windows

will be exposed to a filtered-UV-illumination from a mercury lamp. This radiation starts polymerization and forms a hydrogel window. A photo-mask with a narrow slit is inserted before an objective to shape the resulting hydrogel. Opening of this slit and magnification of the objective determines the size of the membrane later [50].

It has been shown that the PEG-DA hydrogel membrane provides the diffusive transport of solute and solvent between the outer and sample channels. HMM permeability to small solute molecules has been shown in [50], [51]. Also some applications like diffusiophoresis of colloidal particles driven by solute concentration or pH gradients (Nan Shi et al. 2016) and solvophoresis of colloidal particle under solute/solvent gradient in the channel were probed [52].

In this work, we use a 405 nm diode laser which illuminates the filled chamber with 95% v/v PEG-DA (PEG-DA, n=400, 01871-250 Polysciences Inc.) and 5% v/v 2-Hydroxy-2-methyl-propiofenone (405655, Sigma-Aldrich). However, 2-Hydroxy 2-methylpropiofenone (Fig.3.6) has a low absorption in this wavelength (405 nm) thus requiring longer exposure time. But since the depth of the channel is relatively high (40-80 μm), providing fast polymerization would be problematic. Fast cross-linking in the illumination plane might cause inhomogeneous polymer formation in different radiation depths; thick in focal spot of the lens and thin far from the radiation focus. Therefore we compromise these low gelation rates with more uniform cross-linked polymer structures. Additionally, polymerization grows more uniformly while using a low NA objective.

Oxygen, on the other hand is known to be a major inhibitor for photopolymerization. But since the NOA-81 sticker and the glass cover slip are both impermeable to oxygen, long UV exposure is not an issue [53]. The resulting intensity, provided by the diode laser in the focal spot of a 10x objective, becomes 400-500 mW/cm^2 (50 mW power of the laser passing through the 0.45 NA objective). Using Leica TCS SP5 software provided for confocal microscopes (Leica Microsystems, Wetzlar, Germany), we can adjust the laser power. 95% of maximum intensity is required for HMM fabrication. It needs approximately 1 to 3 secs for polymerization of 40-80 μm HMM fabrication. This is comparable to the polymerization of PEG solutions using UV lamps which takes 15 sec to a few min, due to their (10x) lower intensity [54].

Practically, while filling the chamber with uncured polymer, one has to avoid air bubbles and particulate contaminations go through. More details will be described

in development section.

3.2 Device requirements for microrheology using optical trap

3.2.1 Geometry required for cells microrheology

Regarding cell experiment inside the flow chamber some geometry optimization is needed.

There are three parameters that have to be considered; hydrogel formation, molecular diffusion, and the laser light beam path through the flow chamber. Hydrogel comes out more uniformly when the channel depth is low and it needs shorter exposure for polymerizations.

Diffusive molecules are relatively slow, so narrower channels are potentially better for diffusion-based investigation. Also, as diffusion happens through HMM, higher walls (deeper channels) would speed it up.

Last but not the least, is the beam path through the flow chamber. We explain a design well-suited for optical signal detection which is narrow in depth but wide in length. On the other hand, chamber geometry is important for handling the cells; a small channel squeezes the cell.

Indeed, these contradictory requirements have to be compromised. A typical cell diameter is 10-15 μm and as we want to let cells swell or shrink under different osmolarity, devices with different heights were fabricated (ranging from 35 to 70 μm).

The chamber width has to be chosen such that fast molecular diffusion can take place and such that optical trapping experiments can be performed. Regarding the diffusion, the width of the sample channel is proportional to diffusion time. Also since a very high NA objective (=1.3) is used for optical trapping, geometries (height and width) of the sample channel is important to prevent light distortion. If the (large angle-) converging trapping light which comes to illuminate the sample, hits the hydrogel membrane walls, it will get distorted (see Fig.3.13). Optical trap measurements are based on scattered light from the sample that reaches the quadrant photo diode (QPD). Therefore, one has to be careful about the unwanted light scattering while passing the sample channel.

We discuss more details about optical compatibility later in characteristic sections. The width of side channels is chosen to be 150 μm and the sample channel, was varied between 150 to 300 μm , with 40 μm depth.

Thanks to our solid NOA-81 sticker, we could fabricate large aspect ratio devices with the length up to 4 cm without stickers getting ruptured or deformed while peeling off from PDMS molds. Technically, the length of the device is also because the condenser lens is located directly on top of the device, which forces us to make the inlet-to-outlet distance longer than its diameter (> 3.5 cm).

In practice, for the first experiment of microrheology inside the closed microfluidic chamber, several trials with careful analysis and geometrical optimizations were needed to finally get the most successful reproducible protocol.

3.2.2 Surface treatment and hydrophobicity

In order to do microrheology using an optical trap in a microfluidic device, we follow a two-particle assay in which two micro particles are supposed to bind to the opposite sides of the cell and suspend it in its cultural medium. The principle behind optical trapping is based on focusing the laser beam such that an object, such as a micro-particle, experiences a gradient force drawing it towards the highest intensity. In simple words, it is always the result of competition between scattering and the gradient force acting on the particle. Stable trapping requires a large difference of the refractive indices of the particles and the surrounding medium as well as a steep intensity gradient of the beam. Apart from that, cell to bead adhesion can be due to either protein-protein or electrostatic charge interactions. In the first case, protein coated beads bind to the cell in the form of focal adhesions. This works very well for naturally adherent cells [15]. In the case of naturally non-adhering cells like blood cells, focal adhesion would not help since they don't form focal adhesions. Instead, attraction between opposite electrical charges is an alternative option.

Apart from bead to cell binding, adhesion to the channel surface had to be taken into account. Sticking of beads and cells to the chamber surface, especially in the micro-channel is problematic, whereas accumulation of them can fully clog the channel or distort the light.

Hence, there are three modes of adhesion that simultaneously must be taken into account: bead to surface, cell to surface, and bead to cell adhesion.

NOA-81 has been accepted as a powerful substitute to PDMS, with high reproducibility and native hydrophilicity [43]. For suspended cell trapping inside NOA-glass sealed devices, we needed to make the surface hydrophobic otherwise they would find contact, stick or start spreading.

We have three cell lines; 3T3 fibroblasts and MCF-7 are the adherent cells.

Polystyrene beads coated with fibronectin are prepared in order to bind to them as mentioned upon focal adhesion formation. Moreover, L1210 mouse leukemia, a type of lymphocyte B-cells are used. Poly-L-Lysine (PLL) coated bead are provided for binding to these cells. In this case adhesion is based on the electrostatic charge attraction.

Our initial attempts to passivate NOA-81 was to block the non-specific binding sites. We tried the most commonly used compounds: Bovine Serum Albumin (BSA), PEG and Pluronic. We tried varying the concentrations and incubation times inside the flow chamber. This method, however, only partially worked and NOA-81 as the bottom surface seemed to be sticky either for cells or beads or in some cases chemical compounds prevented cell to bead adhesion.

So we flipped the device upside down such that the glass cover slip is located at the bottom surface, as shown in Fig.3.8. We realized, it is enough to make the glass hydrophobic (Also, experimentally the deep channels reduce the chance of sticking to top surface). In fact, surface hydrophobicity is done using vapor silanization of dimethyldichlorosilane (DDS).

Practically, NOA (thiol–ene based photopolymer and oxygen impermeable) is not binding to the glass treated with DDS. Therefore, in order to have tightly sealed sticker on the cover slip, silanization has to be done on assembled devices. Briefly, we sucked the silane vapor through micro-channels for ten to twenty minutes. It is similar to the treatment procedure mentioned in [41] using fluoro-silane ($C_8H_4Cl_3F_{13}Si$) vapor. This treatment lasts up to a few weeks. Finally, vapor silanization with DDS, fibroblasts cells and fibronectin beads were chosen to be probed for future experiments.

As previously noted, air bubbles are the most common complication in the microfluidic systems. Silanization increases the risk of bubble formation, especially if high flow rates are applied initially.

Consequently, surface treatment is one of the crucial steps of the experiment. Freshly coated beads and a new flow chamber, with low flow rates for experiment is recommended.

3.2.3 Fluid flow control

In order to drive and control flow inside the microfluidic channels, we use pressure provided by a compressed-air source. Operation of compressed-air driven flow in microfluidic applications has been presented by [55]. With the aid of pressure regulator, channels are filled by pressurizing solution from sealed centrifuge tubes connected to each of the three channels (see Fig.3.7). Moreover, to be able to suspend micro-beads and cells inside the central (sample) channel, we stop the fluid flow by means of a paper clip and a soft tubing connected to its outlet.

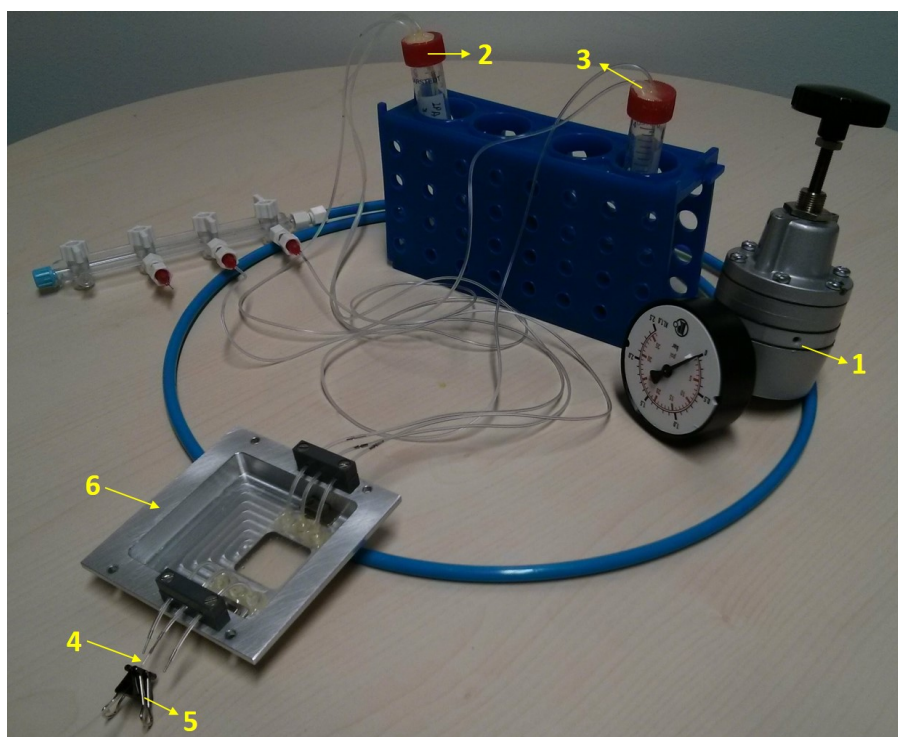


Figure 3.7.: Compressed-air driven flow. A pressure regulator (1), applies pressure by means of compressed air to the medium in tightly sealed tubes (2,3), and drives it through the channels. In this figure, both side channels are fed from the same reservoir (2), where as the central channel is connected to a separate reservoir (3). It is shown closed at one end using soft tubings (4), and a paper clip (5), as it was during the experiment. Position of the chamber was fixed on the shown holder (6), by which it will be located on the microscope stage.

Once the channel is closed, the pressure gradient along the capillary which drives the flow, vanishes. However, flow in the outer channels is kept running to set up a gradient across the central channel that drives diffusion through the hydrogel windows [51].

3.2.4 Bio- and optical- compatibility

Biocompatibility of micro-devices made of NOA-81 has been demonstrated in previous literature [40]. Microfluidic stickers (MFS) have been used for tissue culturing [39]. Neither PEG hydrogels, nor NOA-81 are reported to be poisonous to the cells (Sticker preparation has been illustrated fully in Fig.3.8). Additionally, silane coated channels is done using DDS vapor, which is not toxic for cells. DDS coated glass cover slip also has been used for suspending cell assays in previous work [15].

Poly(ethylene glycol) diacrylate (PEG-DA) hydrogel has been explored in the form of a 2D substrate, scaffolds or 3D capsules for cells and tissue engineering. It is considered to be inert and non toxic to cells [54][56][57],[58], so there is good evidence for bio-compatibility of PEG-based hydrogels.

A part from that, since our device will be used in an optical setup, some modifications are required to make it optically compatible. NOA-81, an optical adhesive glue is selected; its refractive index after curing with UV light changes to the refractive index of glass (1.5 to visible light) [42]. Hence we did not have any problem later on using a condenser lens to collect the light from the sample. Geometrical considerations are mentioned in sections 3.2.1 and 3.4.1 with more details. The sticker was prepared on a standard cover slip glass to be sure no distortion will occur via illumination. Light is going through the sample channel and then passing the NOA layer on top, to be finally detected by QPDs. We believe that a very narrow micro-channel should have a homogeneously distributed NOA top surface with the same refractive index of glass, hence light would not experience any distortion. To increase the precision in this step, spin coating of NOA-81 droplet for sticker preparation is beneficial.

3.2.5 Recycling microfluidic stickers

Our inexpensive device with simple preparation, under proper maintenance can be used for an extended period of time. One advantage of NOA-81 over PDMS which is the most commonly used material in micro devices, is that NOA becomes very stiff with very good adhesion to glass after a few minutes of curing. So, we did not experience any swelling or leakage of the device even when the channels are kept wet for a few weeks. Bacterial growth, however, needs to be avoided in all three channels. Due to additive sugar in the culture medium of cells used for osmotic changes, bacterial growth is expected and actually has been observed.

Regarding this, before and after any use, we wash and fill up micro-channels with isopropanol (*IPA*) for 10-20 minutes. Then it is washed with distilled water for similar amount of time. After rinsing steps, it is ready to be filled with the cell medium. Moreover, using micro filters (e.g 0.2 μm pore size filter) for all consumable solutions, is strongly recommended.

3.3 Device fabrication

3.3.1 Stickers preparation

Microfluidic stickers are made by soft imprint lithography using UV-polymerizable materials and a master PDMS mold. The master mold (PDMS stamp) has to have the proper height and enough features resolution of the desired pattern (see Appendix.A, B.). The negative PDMS stamp is made by replica molding of a photolithographed SU-8 mold (Fig.3.8, A-D). A drop of UV curable resin (NOA-81, Norland Optical Adhesive glue) is poured on a flat PDMS mold and sandwiched with the PDMS stamp (Fig.3.8, E, F). After 2-3 min UV exposure, the PDMS stamp is peeled off and replaced with a cleaned cover slip (Fig.3.8, G). It is better to punch the holes for in/outlets before replication with a cover slip while NOA layer is still soft and completely removing the leftovers is much easier. The flat PDMS mold together with NOA layer bound to coverslip, is exposed to UV light for the second time. Now NOA becomes stiff enough so that it could be detached completely from PDMS mold, while is tightly sticking on the coverslip. Now we flip over the cover slip-NOA chamber and put it under UV light for the last time(Fig.3.8, H). UV exposure for each step is about two minutes, which is optimized based on the aspect ratio and desired geometry.

In this step we can fix the inlet/outlet connections. Tiny acrylic rings are provided so first we pre-fix them on the sticker using a little bit of NOA and short UV exposure. Then proper sized tubings are inserted in the inlet/outlet rings and a 5-min epoxy is applied to fix them firmly together without the epoxy diffusing through. The more accurately the size is matched between opening holes (on the sticker), rings and tubings, results in the less 'dead-volume' we will have later. Depending on the thickness, the epoxy layer may need longer time to totally dry out.

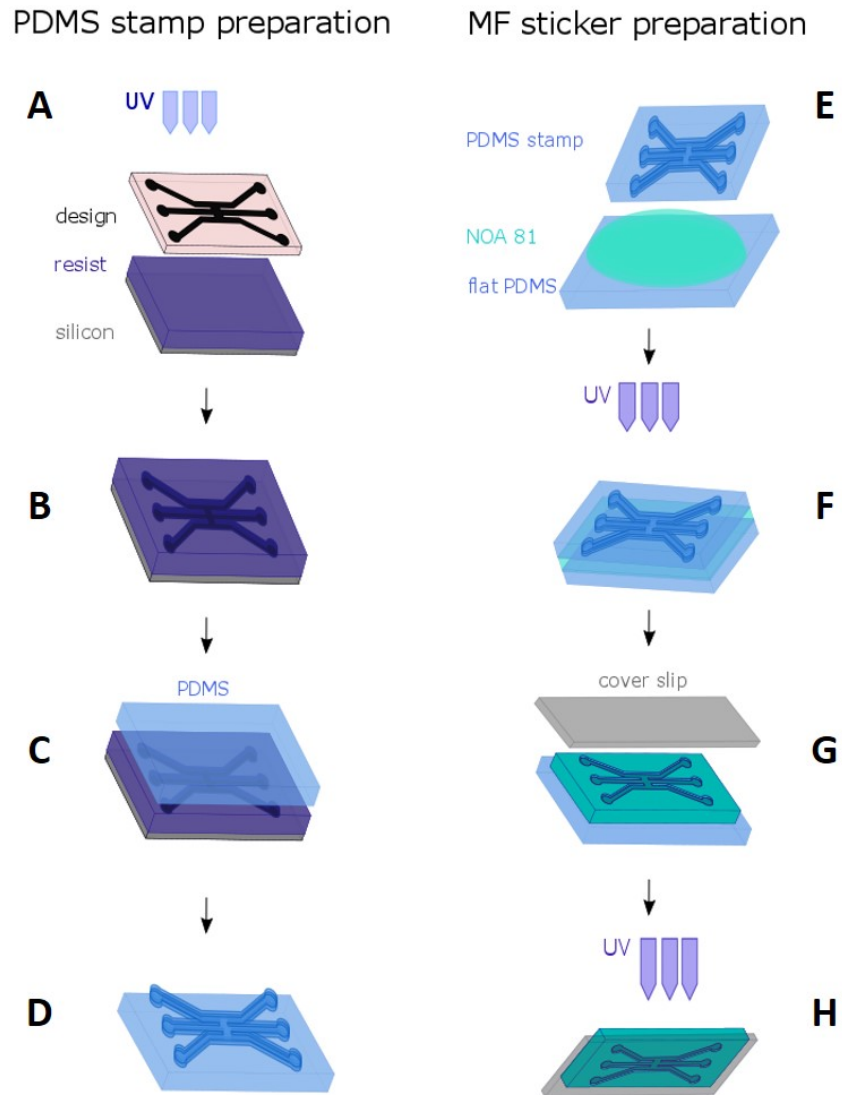


Figure 3.8.: Sticker preparation. Microfluidic stickers made of NOA-81 on glass cover slip using a PDMS stamp. PDMS stamp preparation is illustrated on the left side (A to D) and MF sticker construction steps on the right side (E to H). A) soft lithography of SU-8 photo-resist, B) silicon master mold, C) poured PDMS solution on master mold for baking, D) PDMS stamp, and E) sandwiched uncured NOA-81 between the stamp and flat PDMS mold, F) sandwich exposed to UV, G) stamp replaced with cleaned cover slip, H) PDMS peeled off and sticker exposed to UV.

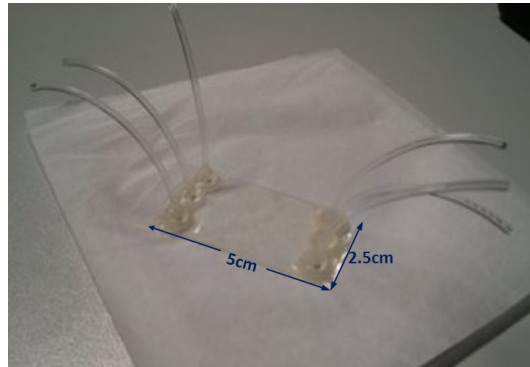


Figure 3.9.: Micro-device final look. Close up view of transparent sticker device made of NOA-81 sealed on a glass cover slip with six in/outlets. The sample channel and two side channels are connected via open windows in the wall. The thickness of the sticker can range from 100 to 200 μm .

3.3.2 Hydrogel membrane fabrication using confocal microscopy

To insert hydrogel windows between the inner and outer channels of our chamber, we followed established procedures [50]. Additionally, we established a new approach to obtain the photopolymerization reaction and 3D printing using confocal laser scanning microscopy. Principles and key points of photopolymerization and hydrogel fabrication were explained in 3.1.3.

Based on that, first we prepared an aqueous hydrogel solution made of 95% v/v polyethylene glycol diacrylate (PEG-DA, n=400, 01871-250 Polysciences Inc.) and 5% v/v photoinitiator (2-hydroxy-2-methylpropiophenone, 405655, Sigma-Aldrich). Second, the channels were filled with PEG-DA and photo-initiator solution. By means of a *LeicaTCSSP5* scanning confocal microscope, we provide an under control photo-reaction, a 10x dry objective (NA=0.45) and a 405 nm diode laser were chosen to drive the reaction. The sample was mounted on a motorized stage while the objective was focused on the middle plane of the channels. As mentioned before to get a sharp-edge hydrogel membrane, parameters had to be optimized. The following values are chosen as they gave the most reliable and reproducible hydrogel. Using 1024 x 1024 pixel format with zoom factor 12x, with the field of view 129.17 x 129.17 μm was selected. The scanning mirror swept this area with the speed of 1000 Hz bidirectionally. By the software interface, the pinhole size could be automatically set to 1 Airy (AU). A rectangular region Of Interest (ROI) with size of 70 x 130 μm was selected to cover the opening window of the chamber wall (a bit larger than window itself 50x100 μm). With this setting

it takes about 500 ms to scan selected ROI once. Three stacks of ROI, with scanning duration of 1557 ms, seemed to give a well-kept straight edge of HMM (see Fig.3.12.). Optimum UV intensity turned out to be 95% of the maximum intensity of 50 mW diode laser (see Fig.3.11,3.1). It is important to wash away the uncured monomers from the channels quickly after illumination. Otherwise the reaction would last longer and cause widening in HMM wall.

As PEG-DA is a very viscous solution and hard to get out of micro channels, we started rinsing first with isopropanol (IPA) and then continued for about 10 min with deionized water. Rinsing with IPA in two ways is beneficial: PEG is solvable in IPA, and channel surfaces are hydrophobic. So it helps to speed up the rinsing.

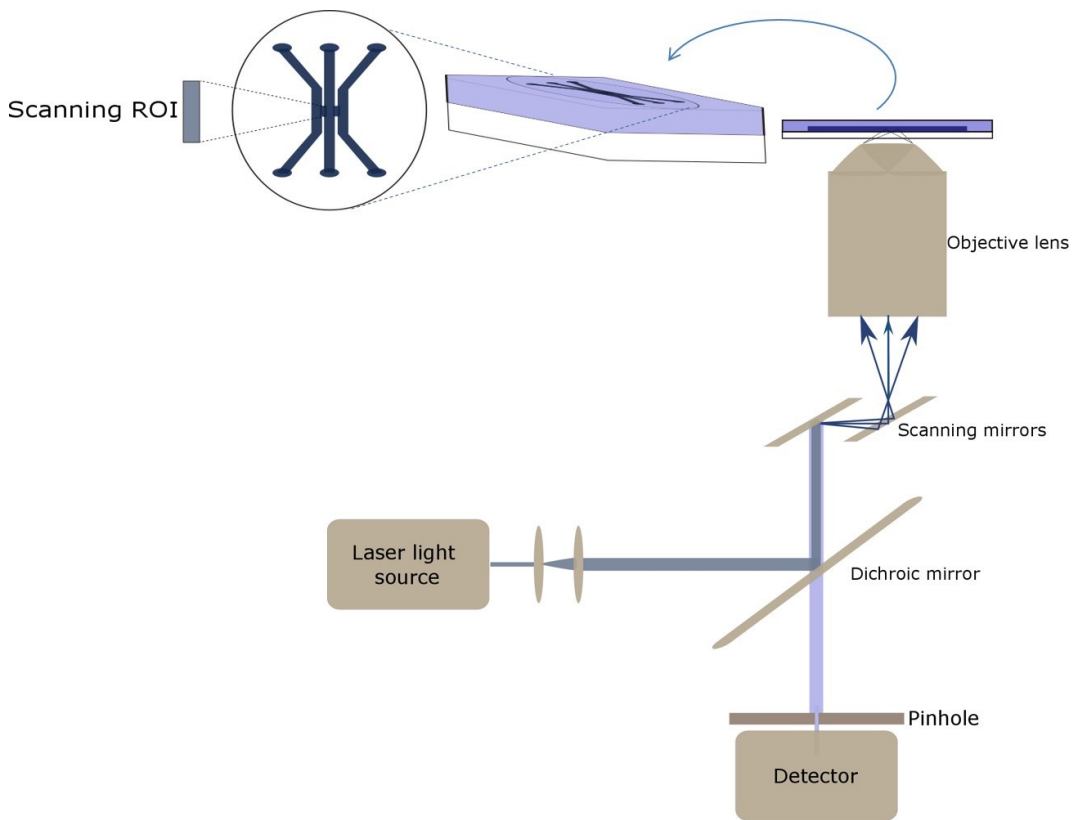


Figure 3.10.: Laser scanning confocal microscope. UV laser scanning confocal microscopy. The laser is focused on the middle plane of the micro device is scanning the rectangular ROI.

As discussed before, HMM thickness and its pore size will change by duration of UV exposure and laser light intensity. Longer UV exposure results in wider, more bulgy membrane and smaller pores. The same is true for increased light intensity. The permeability of large molecules (here biochemical molecules and

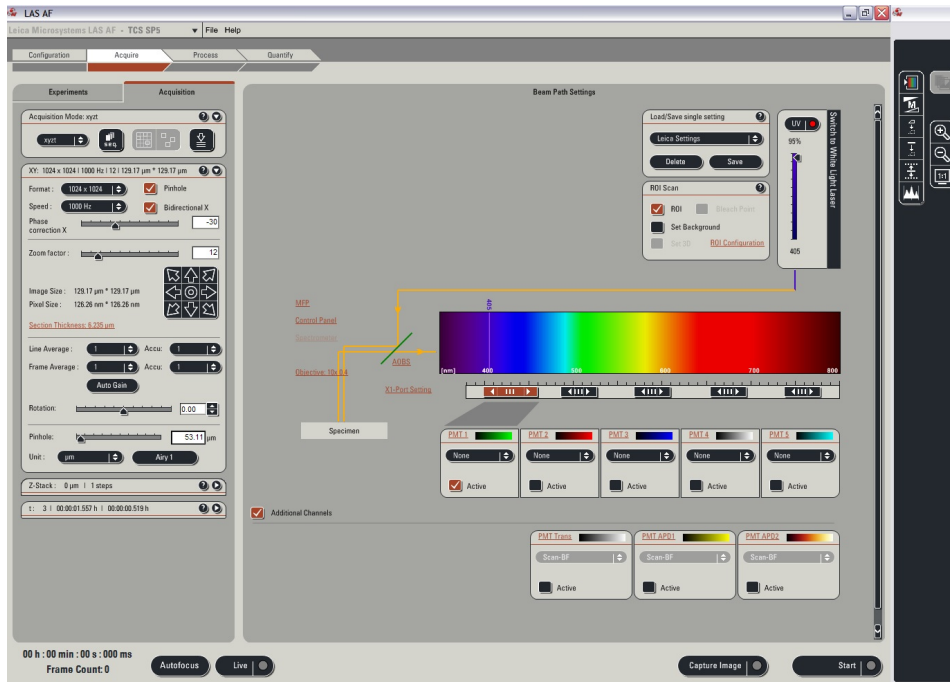


Figure 3.11.: LAS AF software interface. Selected parameters for UV laser scanning confocal microscope: 10X dry objective (NA=0.45) focused the 405 nm diode laser light on the rectangular region of interest (ROI). The 70X130 μm window is scanned with UV light for 1.5 sec to induce the photopolymerization.

Table 3.1.: LAS AF software interface. Selected parameters for UV laser scanning confocal microscope. 1557 ms, and 95% UV intensity.

Acquisition parameter	Set value/mode
Illumination wavelength	405 nm (diode laser)
Laser power	95% of max (=50 mW)
Objective	10 x dry (NA=0.45)
Acquisition mode	XYZt
Image format	1024 x 1024
Scanning speed	1000 Hz (bidirectional)
Pinhole	1 Airy
Zoom factor	12 x
ROI	70 x 130 μm
Exposure time	1557 ms
Z-stack	1 step

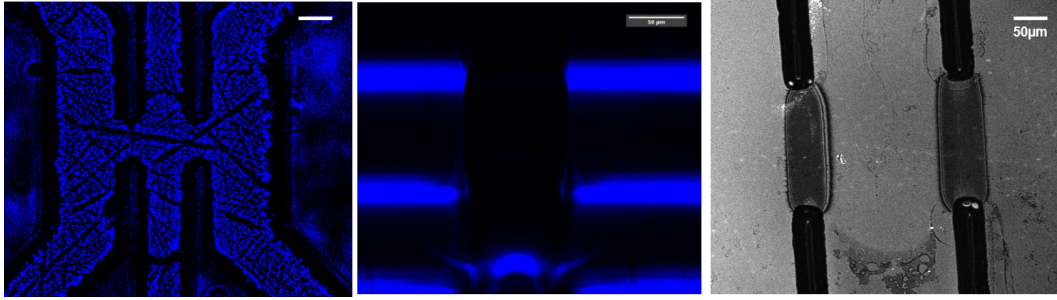


Figure 3.12.: Photo polymerization of hydrogel inside a micro device. From left to right: Filled chamber with uncured PEG-DA, side view of 75 μm HMM, top view of HMM after an immediate wash of uncured monomers (scale bars: 50 μm).

proteins) highly depends on these two parameters.

In fact, confocal scanning hydrogel fabrication is a simple and cheap novel method of 3D printing in a closed system. What is shown in this work is single plane laser scanning hydrogel fabrication with a simple design. Indeed, scanning confocal microscopy is capable of printing more complicated patterns as well as taking stacks and multi-step fabrications.

3.4 Device characteristics

3.4.1 Beam path inside the flow chamber

From the optical point of view, since a very high numerical aperture objective (NA=1.3) was used, channel geometrical dimension (height and width) of the sample channel is very important. A converging light with a large angle, comes to illuminate the sample. It may hit the hydrogel membrane and scatter. Therefore the signal detected by the QPDs will be distorted. Especially since we expose the sample to an oscillating force and want to collect the scattered light from the sample, it is crucial to make sure that there is no dispersion of light next to the hydrogel membrane.

Using ray optics calculations

$$NA = n \sin(\theta/2) \quad (3.4)$$

can give us a theoretical estimation of the diverging light's angle. For instance, an 100x oil immersion objective (1.3 NA) in a medium with refractive index of 1.33 would provide a light cone of $\theta \sim 78$ degree. The beam path inside the device is

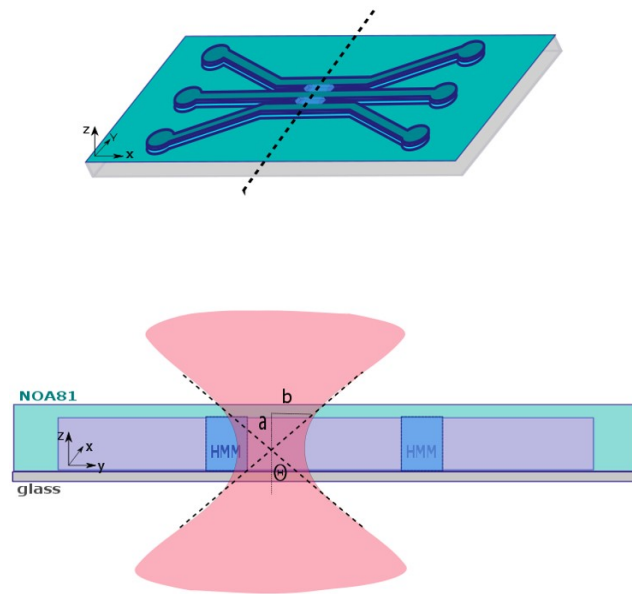


Figure 3.13.: Light path inside the flow chamber. Top view and cross section of the micro-device from the dashed line on top. Hydrogel membrane micro-window (HMM) is shown in light blue. Light is focused inside the sample channel by a high NA objective. On the left hand side, the trapping light hits the wall next to the hydrogel membrane and distorts before detecting by QPD.

illustrated in Fig.3.13. We calculated the side lengths of the cone a, b and the corresponding opening of the cone $2xb$. In other words $2xb$ shows the minimum width for the channel needed to prevent a conical beam hitting the wall (see Fig.3.2).

Table 3.2.: Numerical aperture of the light cone. When a, b are the side lengths of the light cone equal to the depth and half width of the channel respectively (illustrated in Fig.3.13), $2xb$ is the minimum width of the channel needed to prevent light hitting hydrogels (all in μm).

a	b	2xb
5	5	10
10	15	30
20	35	70
25	42	84
30	50	100
35	57	114
40	65	130
45	75	150
50	85	170

Finally, to avoid any additional signal distortion due to geometrical constraints, we chose a narrow and wide configuration of channel with $40\ \mu\text{m}$ height, $300\ \mu\text{m}$ width and $35\ \text{mm}$ length.

In practice, after passing through the sample, trapping laser light is scattered. A condenser lens collects both, the scattered and the transmitted or the trapping beam. Superposition of these beams results in an interferometric pattern in the back focal plane (BFP) of the condenser lens. The pattern characteristics depend on the relative position of two beams. It is imaged by a quadrant photo diode (QPD) resulting in a spatial distribution of intensity. Any movement of the trapping particle will shift the intensity distribution in BFP detected by the QPD. This technique is known as back focal plane interferometry was presented by (Gittes and Schmidt. 1998), [21].

Based on back focal plane interferometry and detected intensity by the QPD, we tested our device to see whether the light was scattered and hit the membrane wall while passing through the chamber. We are going to track the power spectral density (PSD) of the trapping beam in a channel filled only with water. The peak of the PSD is followed, while the relative distance between the beam and the hydrogel wall was changing.

To this end, we programmed the stage to oscillate in both lateral directions, parallel and perpendicular to the membrane wall with a certain frequency and amplitude.

The stage oscillation shown in Fig.3.14 had $1\ \mu\text{m}$ amplitude and $50\ \text{Hz}$ frequency, when HMM is elongated in X direction and the stage is moving back and forth in X or Y directions. The PSD signal showed its highest peak at the frequency of stage oscillation $50\ \text{Hz}$. The maximum PSD peaks versus the distance from the center of the chamber are shown in Fig.3.15.

The peak of PSDs when the beam oscillates parallel to the HMM (X direction, in Fig.3.13) remains unchanged. However, when the beam moves perpendicular to the HMM (Y direction, in Fig.3.13), the PSD peaks raised distinctively. Meaning, moving the beam in this direction, close to the HMM, caused an unwanted distortion or scattering.

Finally, it has to be mentioned for experiments and results presented in this work, no oscillation perpendicular to HMM (Y direction, in Fig.3.13) has been done. Besides the wide and narrow channels, we had to hold the cells in the center of the channel while recording the QPD signal for the optical trapping

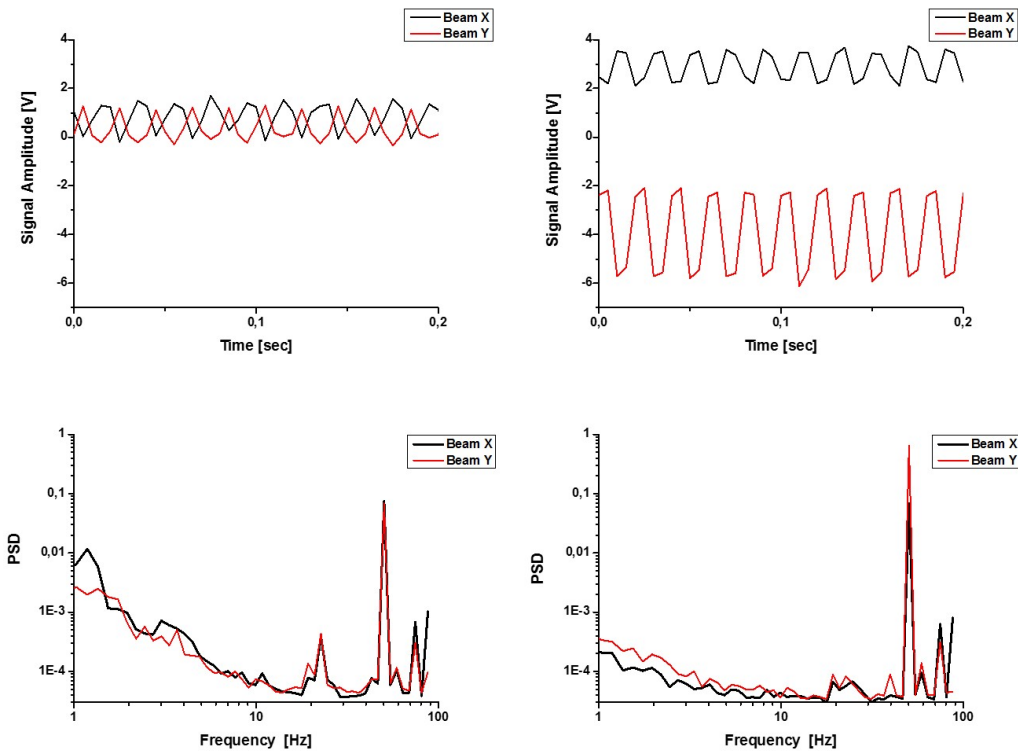


Figure 3.14.: Signal amplitude and power spectral density in flow chamber depends on distance to the HMM. Voltage amplitude on top and power spectral density (PSD) of the QPD signal on the bottom panels are raising when the focused laser beam is getting closer to hydrogel wall. The microfluidic device fixed on the stage was oscillating with 50 Hz perpendicular to HMM (Y direction) and changing the relative distance of the laser focus with respect to the HMM. Plots corresponding to a laser focus 130 μm from the membrane wall are shown on left and 80 μm focus-HMM distance on the right side.

measurements. It was crucial to avoid any unwanted light scattering.

3.4.2 HMM thickness, pore size and exposure time

Hydrogel membrane pores are small enough to act like an impermeable barrier to the side fluid, but as discussed before, they are still large enough to allow for diffusion of solute/solvent molecules. The mesh size of the hydrogel would change for different ratios of PEG-DA and photoinitiator, as well as UV dosage and exposure time. Longer exposure time results in wider HMMs with smaller pores and therefore less trans-membrane flow is expected [50].

In the following section, the effect of 2595 ms UV exposure on HMM properties is investigated (Fig.3.16). It is observed that membranes turned to be wider

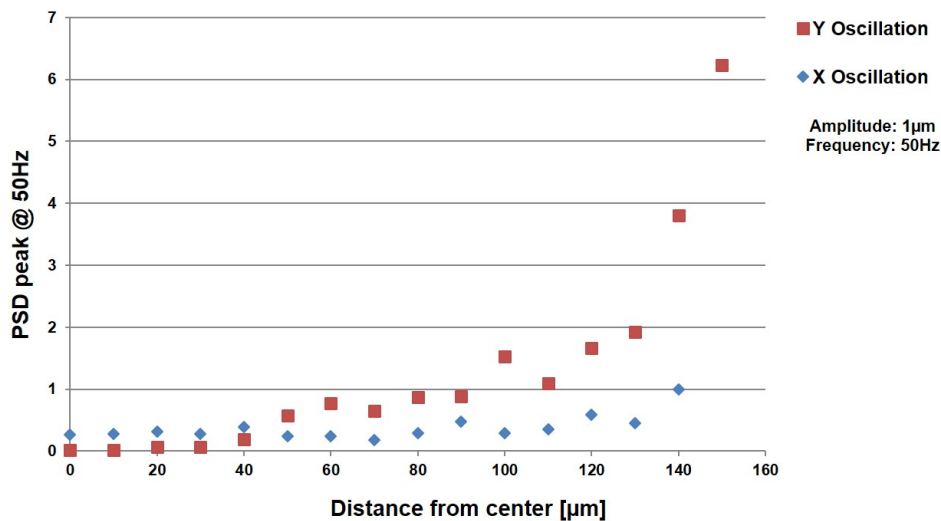


Figure 3.15.: QPD signal due to distorted light path inside the flow chamber. Effect of the wall on power spectral density of detected signal on QPD, when beam oscillates with $1\mu\text{m}$ amplitude in lateral directions: parallel and perpendicular to HMM (every $10\mu\text{m}$ from the center of the sample channel). Blue points are showing PSD peaks when the beam oscillates parallel to the HMM (X direction). However, red points show PSD peaks when the beam moves perpendicularly toward HMM (Y direction).

and bulged out more in the middle. For this experiment 2 mM blebbistatin solution was running in the side channels, when the sample channel contained $1\mu\text{m}$ fluorescent beads with 0 mM blebbistatin. As a result, within 32 sec no difference in the distribution of the micro beads occurred (Fig.3.18). Apparently, a long exposure time resulted in a hydrogel with small pore size.

The evidence for this, was when the exposure time has been decreased to one-half in Fig.3.17, 3.18, the same solution diffuses through and pushed the micro particles away.

We tested the permeability of our laser fabricated HMM, in two separate ways. First as shown before in Fig.3.16, 3.17, we put the fluorescence micro-spheres in the central channel and run solutions containing molecules such as blebbistatin or sugar along the outer channels and followed permeability of HMM.

Secondly, using live cell imaging techniques (not shown in this chapter), we put the fluorescence labeled cells in the sample channel and maintained for example the sugar solution in the outer channels. Hypothetically diffusion of sugar changes the osmotic pressure and results in changes in cell size (Fig.5.3, 5.5). Or in the case of biochemical diffusion, one can observe drug interference on the cells. Indeed,

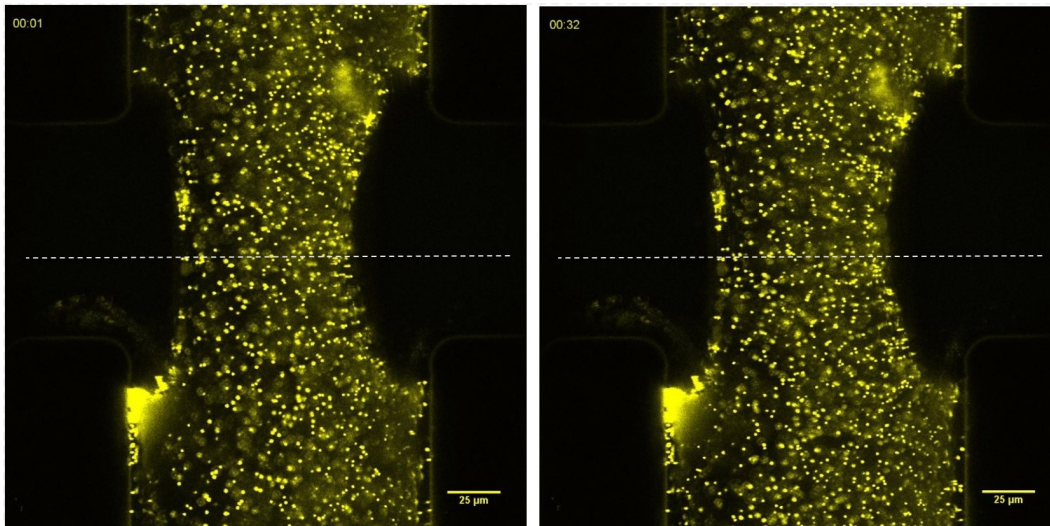


Figure 3.16.: Thick HMM fabricated with long UV exposure. 2595 ms UV exposure did not allow blebbistatin molecules from side channels passing through membranes. The left image shows the initial distribution of $1\mu\text{m}$ fluorescent beads in the sample channel. On the right, their distribution with no change within 32 sec of flowing 2 mM blebbistatin solution in the side channels (scale bar: $25\mu\text{m}$).

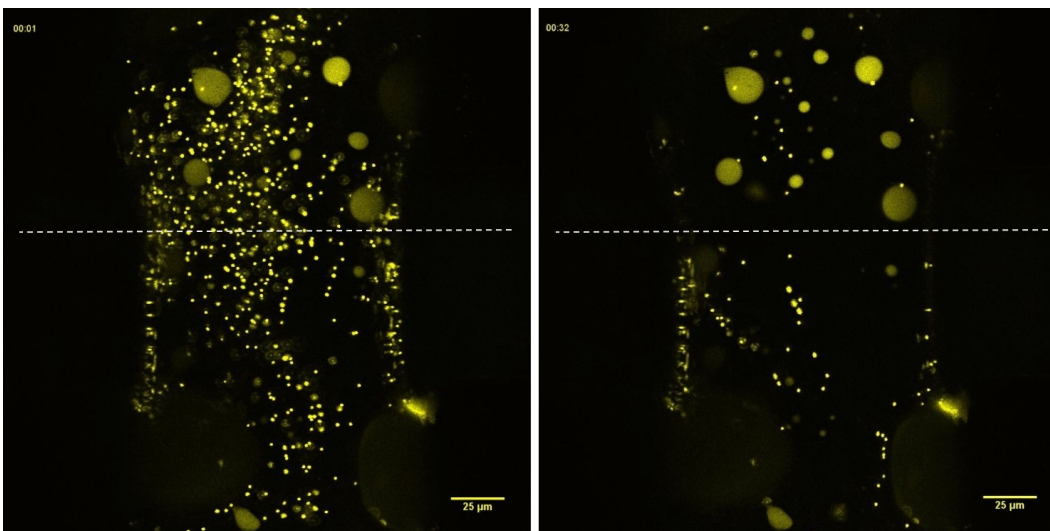


Figure 3.17.: Thin HMM fabricated with short UV exposure. 1500 ms UV exposure makes blebbistatin molecules from the side channels passing through the membrane. The left image shows the initial distribution of $1\mu\text{m}$ fluorescent beads in the sample channel. On the right, their distribution changed within 32 sec of flowing 2 mM blebbistatin solution in side channels (scale bar: $25\mu\text{m}$).

this makes the HMM integrated chamber a very powerful device for biophysical

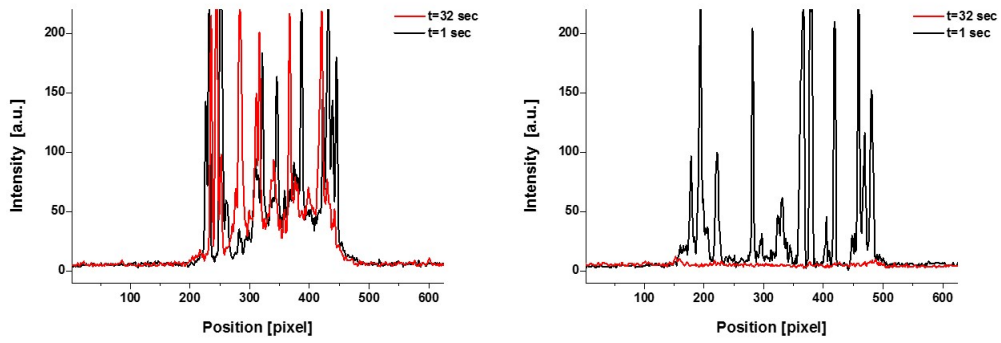


Figure 3.18.: Thick versus thin HMM. Fluorescent microsphere profile is changed by blebbistatin molecules diffusing through the thin hydrogel membrane but not the thick one. Intensity of dashed lines marked in Fig.3.16, 3.17 at t=1 sec is compared to intensity at t=32 sec.

studies. In the next two chapters, some more evidence for HMM permeability will be shown and discussed.

Short exposure time results in a thin membrane with straight edges. However, besides diffusion it might undergo a trans-membrane flow. A trans-membrane flow of fluorescein solution can be observed in case of a high pressure gradient across the HMM (Fig.3.19). This flow obeys Darcy’s law:

$$u_m = -\kappa(\Delta P_m) / \eta w_m \tag{3.5}$$

where η is viscosity of the fluid and w_m is the membrane thickness, ΔP_m denotes the pressure gradient across the HMM, κ is the Darcy permeability and u_m is the trans-flow velocity. κ , is related to the pore size $l_p = \kappa^{1/2}$. According to [59], for traditional hydrogels κ is about 9-16 nm which results in 3-4 nm pores. Trans-membrane flow with a 1.5 bar pressure difference across a 50 μm HMM according to Darcy, results in a velocity of 30 $\mu\text{m}/\text{s}$. Fig.3.19 shows trans-flow of fluorescein sodium salt from the side across the thin HMM within less than 5 sec.

Nevertheless, a very high pressure gradient is not desired for microrheology experiments. All the experiments inside the flow chamber were performed between 0.1 to 0.2 bar. Thus, trans-membrane flow did not influence our measurements.

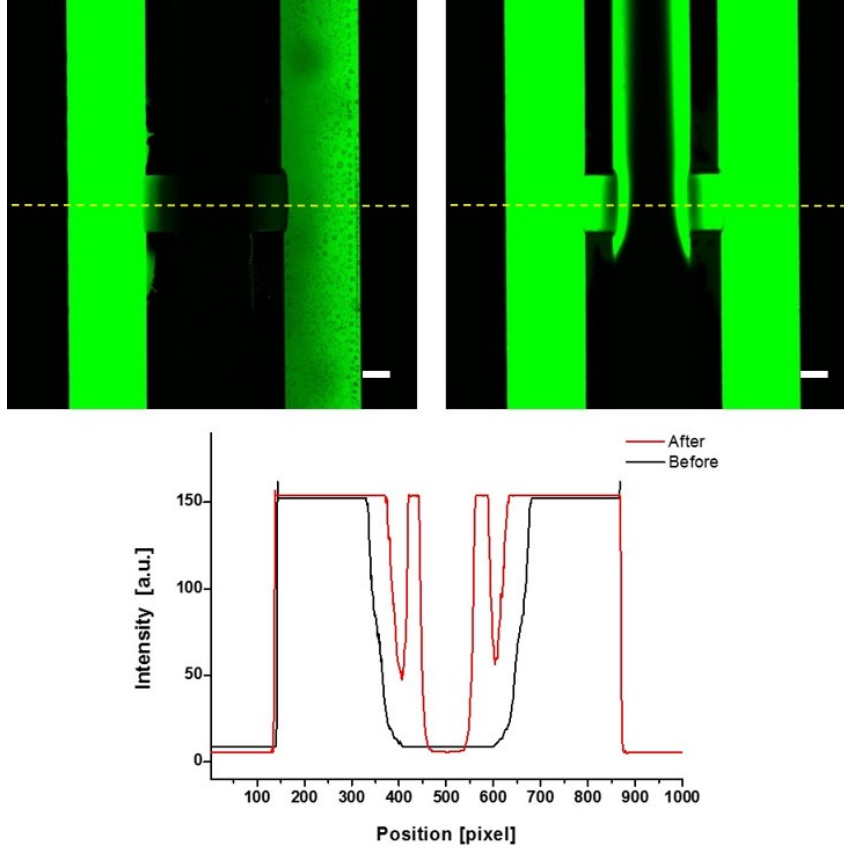


Figure 3.19.: Trans-membrane flow through thin membrane. 1500 ms UV exposure makes trans-membrane flow through thin membrane. All three channels are $150\ \mu\text{m}$, when fluorescein sodium salt running along side channels, passed the $50\ \mu\text{m}$ membrane within <5 sec. The bottom panel shows the intensity profile of the dashed line (marked on the top panel) before and after trans-membrane flow of fluorescein solution (scale bars: $50\ \mu\text{m}$).

3.4.3 Diffusion through HMM

Diffusion time τ_D over a distance L for a solute or molecule with diffusivity D scales like

$$\tau_D \sim \frac{L^2}{D}. \quad (3.6)$$

Typical diffusivity for molecules like glucose and sucrose, or small solutes like NaCl in water is on the order of magnitude with $D \sim 10\ \mu\text{m}^2/\text{s}$ [60][61],[62]. Therefore, the time for diffusive delivery for such dissolved molecules over $100\ \mu\text{m}$, will be $\tau_D \sim 10$ sec. According to [50], the time needed for diffusing in a micro-channel through a HMM becomes

$$\tau_D \sim \frac{(2w_m + w_s)^2}{\pi^2 D} \quad (3.7)$$

where w_s is the width of sample channel, w_m the thickness of the membrane and D is diffusivity of molecules passing through. Experimentally, we investigate diffusion of fluorescein sodium salt through our laser fabricated hydrogel membrane. The results are shown in Fig.3.20, 3.21. Time dependent diffusion pattern and the dynamic intensity profile of a marked dashed line is depicted.

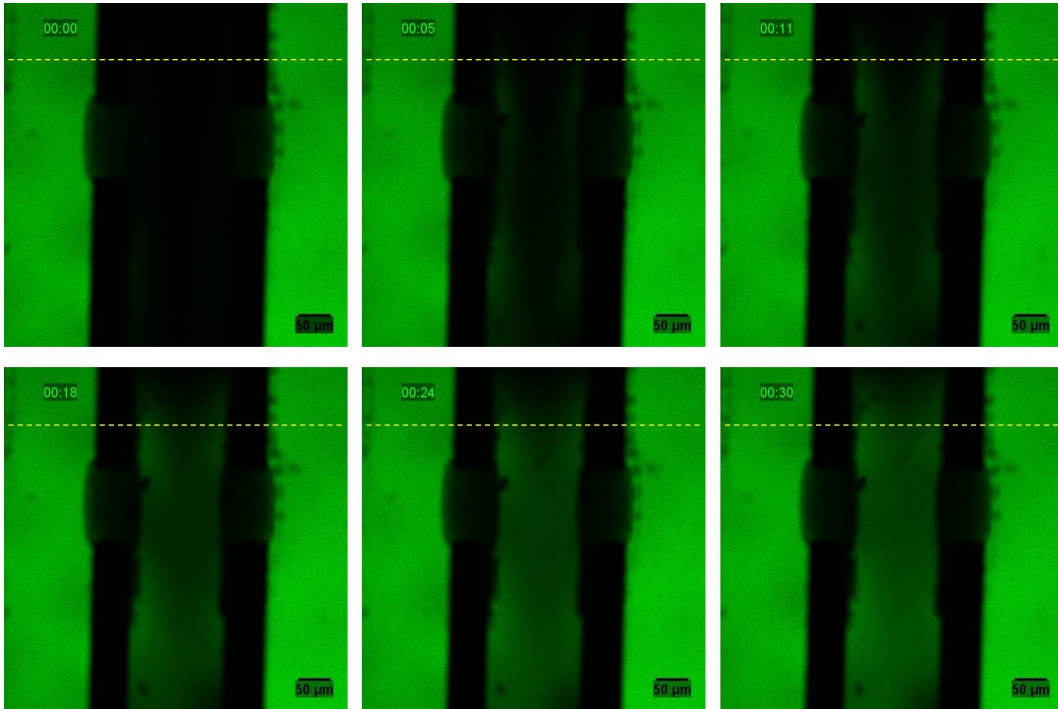


Figure 3.20.: Diffusion of fluorescein molecules through hydrogel membranes. Diffusion pattern of fluorescein molecules through HMM over time.

Considering the dimension of the device ($150 \mu\text{m}$ sample channel after $\sim 50 \mu\text{m}$ HMM) and diffusion from both side channels to the central channel, the results are consistent with the theoretical diffusion time of $\tau_D < 10 \text{ sec}$.

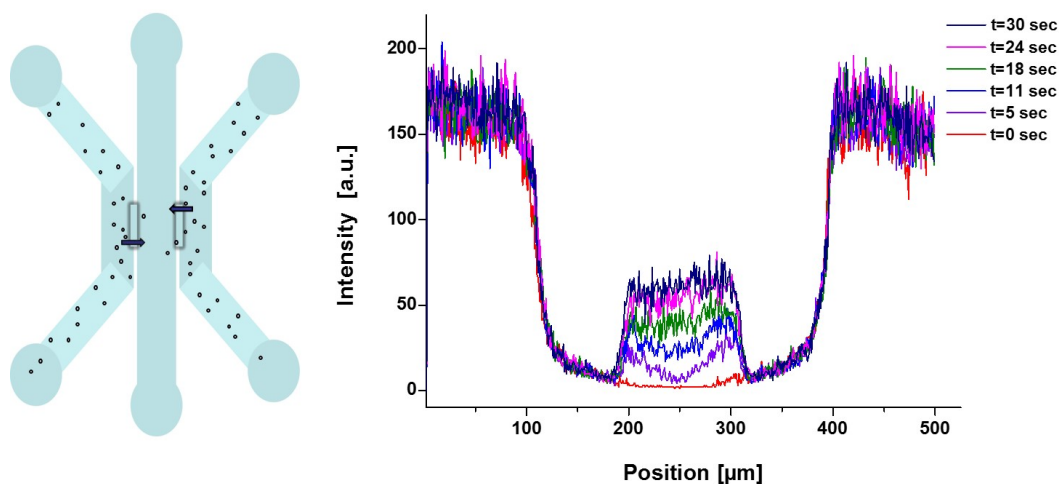


Figure 3.21.: Diffusion of fluorescein molecules through hydrogel membranes. Left: schematic view of diffusion through HMM walls. Right: intensity profile of the dashed line in Fig.3.20.

3.5 Summary and conclusion

In this chapter, the three channel microfluidic device with integrated hydrogel micro-membrane windows (HMM) was introduced. Fabricating microfluidic stickers (MFS) out of NOA-81 [42] was explained.

The innovation part of work, photopolymerization of hydrogel using scanning confocal microscopy, with detailed description of exposure time and intensity and the result have been explained. Molecular diffusions through thick and thin HMM probed with microsphere tracer (and blebbistatin solution) or fluorescein dye, to test the permeability of laser fabricated HMM have been illustrated.

Moreover optical characteristics such as light transparency and the corresponding geometrical optimization was discussed. Surface treatment and stickiness also was considered. Finally, we ended up with the vapor-silanized, narrow-depth but wide channel ($40 \times 150 \mu\text{m}$) that fulfilled the hydrophobicity and optical requirements. Diffusion of the sugar and biochemical molecule through HMM were tested. At the end, successful diffusion based movement of small molecules together with a localized concentration gradient across the HMM have been achieved.

The specific configuration of this device, functionality of the integrated membrane, optic- and bio-compatibility, together with its low-cost and simple fabrication is inspiring to use such micro-chamber for manipulating living cells suspended with optical traps. In the following chapters, cell response to pharmacological inhibitors as biochemical and osmotic changes as mechanical stimuli are presented.

Cellular morphology and mechanics in response to biochemical stimuli

“Cytoskeletal systems are dynamic and adaptable, organized more like ant trails than interstate highways.”

Bruce Alberts

4.1 Introduction

Mechanical properties of cells change from normal to diseased and abnormal states, which has been utilized to detect cancer. There is increasing evidence that cell functions are related to its morphological and mechanical properties [63]. Hence, it is necessary to look carefully through changes in mechanical response of the cell [64].

In this chapter, the focus is on the interplay between cellular morphology and mechanical properties of suspended cells undergoing internal structure perturbation. Experimentally, we investigate connections between these in suspended

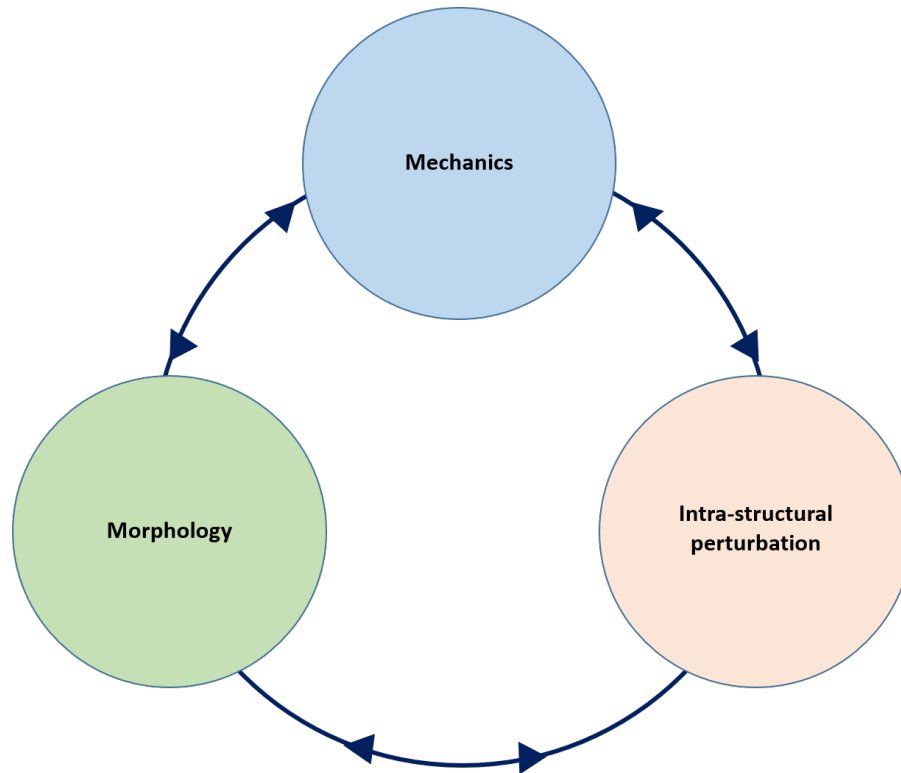


Figure 4.1.: Cell mechanics depends on its 3D morphology and change with biochemical stimulation. Interconnection between cellular morphology, internal structures and mechanical properties.

cells, which will be described in the following section after a brief introduction of probed cellular organization.

4.1.1 3D cellular morphology

Animal cells are living in a complex three dimensional (3D) micro-environment. However, a wide range of basic *in vitro* and clinical research studies has been done in two dimensional (2D) environments [65]. Easy environmental control, cell observation, manipulation, imaging and measurement are the main advantages of 2D cell cultures [66]. Nevertheless, it decreases the compatibility with the *in vivo* system and also increases drug sensitivity in both fundamental and clinical investigations [3]. Nowadays, it is well known that cells behave structurally and functionally different when they adhere on a 2D substrate versus their natural 3D environment, which has a higher degree of structural complexity and experimentally is challenging to maintain a steady state [67].

Most 2D studies are adhesion dependent with an inhomogeneous distribution of the organs and intracellular structures which effects the measured values for mechanical properties such as elastic modulus.

Based on morphology, mammalian cells in culture are divided into three main categories:

- Fibroblast-like: These cells are naturally adhering to their substrate in bipolar or multi-polar elongated shapes.
- Epithelial-like: Cells which are packed together very closely for mechanical support and better communication in all directions. They have a polygonal shape and attach to their substrate in district patches to grow.
- Lymphoblast-like: They are growing in suspension with no need for adhering to substrate and are mostly spherical in shape.

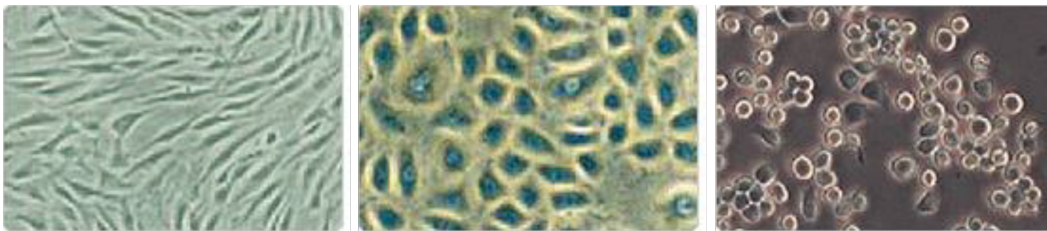


Figure 4.2.: Mammalian cell morphology in culture. Three main categories of mammalian cells in culture (from left to right): Fibroblast-, epithelial- and lymphoblast-like cells. The first two which look bipolar or multi polar in shape, grow attached to a substrate. Whereas lymphoblast-like grow in suspension. Taken from <https://www.thermofisher.com>.

In this work, we experimentally studied naturally non-adherent cell lines and also adherent cells brought into suspension; therefore, only the rounded-up cell configuration is described here. Regarding morphology, round cells typically have a less stiff cytoskeleton (Young's modulus < 1 kPa) compared with the flat adherent ones. Osteocytes in rounded-up and partially adherent state have about an order of magnitude lower elastic constant than when they are attached and flattened [63].

Blood cells are the most well-known example of suspended cells, and have been studied for years. Many other eukaryotic cells appear spherical in shape during mitosis [68],[69],[2]. Stiffness of the cell in this phase, has been shown to be dominated by the cortical layer [69].

4.1.2 Cytoskeleton structures, morphology and cell mechanics

The cellular cytoskeleton is actively involved in mechanical stability and shape control as well as force generation, which is needed for different cellular functions such as motility, cytokinesis and locomotion or in mitosis. It is known that from cytoskeletal structures like actin filaments and microtubules to different cellular organs like the nucleus, all cell components contribute to determine mechanical properties of the cell [70]. For instance, it has been proven that the cellular response to mechanical force using atomic force microscopy (AFM), is the consequence of actin binding proteins, formation and growth of focal adhesions, as well as the presence of lamin in the nucleus [71].

Cortex in adherent versus non-adherent cells

The cortex of rounded cells, keeps the integrity of the eukaryotic cells against external forces and hydrostatic pressure, as well as regulating the cell volume. It is a condensed self-organized network composed of actin filaments and molecular motors such as myosin, together with crosslinking proteins. Myosin motors pull on actin filaments and form a thin shell of actin network all around the cytoplasm. Myosin activity makes these filaments slide on each other, adding pre-stress and hence generating tension all around the cortex. Myosin contribution in tension regulation makes it one of the key cytoskeleton component in force generation [6], [72].

This structure of the cytoskeleton is different in adherent cells that attach to their substrate upon anchor spots called focal adhesion [73]. Focal adhesions are complex proteins that frequently are associated with large bundles of filamentous actin, known as stress fibers. These fibers (attached at one or two ends to focal adhesions) connect the spreading cell to the substrate underneath. Forces are sensed through focal adhesion and transmitted via stress fibers through the whole cytoskeleton. Typically, cross-linked actin filaments and myosin motor proteins are the essential components of these high-ordered structures. Geometry of attachment is important in cell rheology since it changes the cell morphology and organelle distribution, and therefore mechanical properties. It has been shown that during adhesion to the substrate, focal adhesion and pre-stress fibers (bundle of filaments) are required to maintain the flattened morphology and force transmission [74].

In this case, stiffness of the substrate has been shown to have a large impact on cell structure, adhesion and therefore mechanical properties of the cell. According to (Yeung et al.2005) cell softening has been seen while stress fibers gradually disappeared. It is possibly due to reduction of pre-stress on actin network. Whereas, increasing number of focal adhesions in cells on a substrate leads to more and stronger stress fibers and therefore increases cellular pre-stress [75].

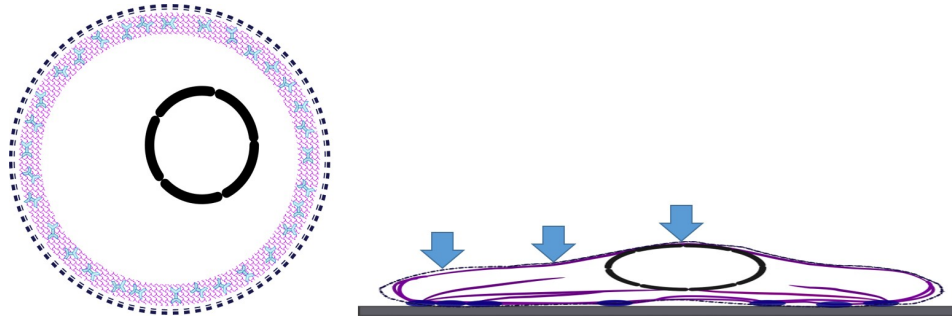


Figure 4.3.: Cytoskeletal organization of adherent and non-adherent cells. Structure of the cell cortex in suspension (left) and adherent cell (right hand side). Underneath the lipid membrane of suspended cell, a network of actin filaments in pink and myosin motors in blue as main components for mechanical stability are illustrated. The cell nucleus inside is in black. However, in non-adherent cells, focal adhesions (dark blue spots) and stress fibers (purple) play a role in force transmission and mechanical properties. Depending on position and method applied for mechanical measurement, non- homogeneous distribution of organelles and structure may change resulting values.

Myosin has been proven to be a key cytoskeleton component in both configurations. It generates contractility on actin-structured networks and regulates the tension in the cell cortex. Therefore, this network has been considered as an active material [6]. This fact made us pay careful attention to the role of myosin motors in mechanics of cells in suspension.

4.1.3 Interfering with myosin contractility

Myosin IIs, the ATP driven molecular motors, are essential components in the motility, contraction, cytokinesis and cortical tension maintenance of eukaryotic cells [77]. Non-muscle myosin II(NMM II), has a globular head domain containing actin binding region and enzymatic ATPase motor domain (see Fig.4.4). Essential and regulatory light chains link the head domain to the heavy chain. NMM II molecules assemble into bipolar filaments and bind to the actin filaments through their head domain. ATPase activity of the head moves actin in an anti-parallel way. Phosphorylation of the light and heavy chain regulates NMM II and increases

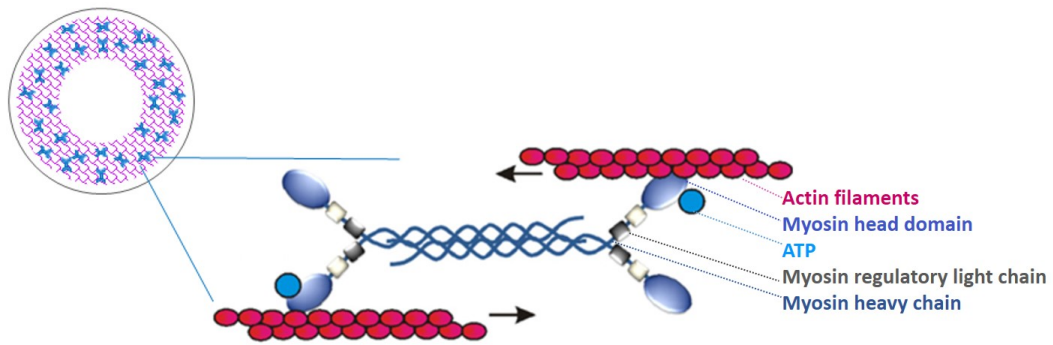


Figure 4.4.: Acto-myosin cortex of non-adherent cells. Exaggerated actomyosin cortex underneath the thin membrane is illustrated with magnified actin filaments pulled by non-muscle myosin II. The cortex underneath the lipid membrane of suspended cell, a network of actin filaments in pink and myosin motors in blue is illustrated (nucleus is not shown here). myosin II motor protein consuming ATP, blue granules bound to its head domain, as a fuel generates mechanical forces. This figure is modified from [76].

ATPase activity of myosin in presence of actin [78].

In order to inhibit myosin motor activity, we introduced the non-adherent cell to two known pharmacological myosin inhibitors: blebbistatin ($C_{18}H_{16}N_2O_2$) a selective non-muscle myosin II ATPase inhibitor, and Y-27632 ($C_{14}H_{21}N_3O$) the rock pathway inhibitor.

Blebbistatin, binds to the ATPase intermediate, slows down phosphate release and induces low actin affinity by which it blocks myosin heads in an actin detached state [77]. Concluding, it prevents myosin head attachment to the actin filaments on the cortex. The second compound inhibits Rho-associated kinase, bringing myosin to an inactive phase and decreases phosphorylation of myosin light chain [76].

According to [14], blebbistatin decreases cell contractility and results in 50% reduction in cortical tension of non-adherent HFF monocyte cells. Also the cortex elastic modulus on average decreased about 50% compared with untreated cortices.

We tried both of them to perturb myosin and get the time series of force generation and cell stiffness in the absence of the contractility.

For better visualization, an example of fluorescence imaging of our myosin labeled fibroblast before and after blebbistatin treatment is shown in Fig.4.5. In fact it looks similar to (Chan et al.2015) who showed actin labeled fibroblasts under the

same blebbistatin treatment. So taken together, the untreated cells show myosin and actin highly pronounced on the cortical layer underneath the plasma membrane (additionally actin labeling showed bleb-like structures), while the cortex of blebbistatin-treated cells look soft a bit floppy with myosin diffused in the whole cytoplasm.

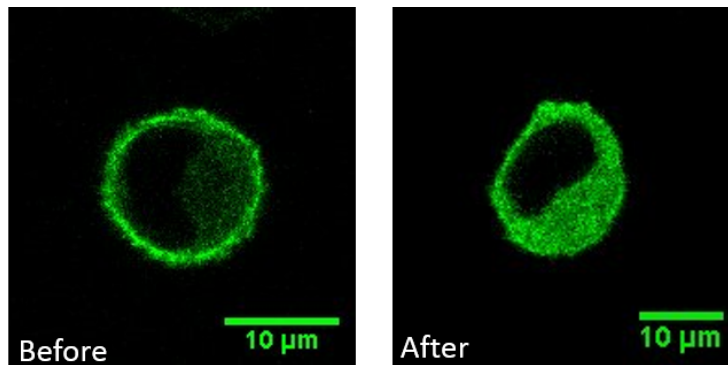


Figure 4.5.: Blebbistatin treatment of myosin labeled 3T3 fibroblasts. Representative cell in suspension undergoing blebbistatin treatment. Myosin is more pronounced on the cortical layer (left). However 20 min after drug perturbation (right) it seems be distributed through the whole cytoskeleton.

4.1.4 Experimental approach

- Conventional and new methods to study mechanics of cells and the cortex

There are several techniques to study the mechanics of suspended cells including micropipette aspiration, magnetic and optical tweezers, AFM and more recently optical stretchers. They typically apply different ranges of forces and measure stiffness in different ranges. AFM goes up to nN and can measure the stiffness of 10-100 pN/ μ m. Magnetic tweezers by means of a magnetic field gradient can measure displacements of the order of 10nm and apply forces from 0.05 to 20 pN and therefore can measure a lower stiffness \sim 0.1 pN/nm. Optical tweezers using light intensity gradients can go to the sub nm range (0.1 nm), and apply typical force from 0.1 to 100 pN, which is small enough to measure stiffnesses of 100s pN/ μ m [10][12],[13].

Micropipette aspiration and parallel glass plate have been used to determine cortical tension, intracellular pressure and elastic modulus. In spite of an easy implementation, they require large deformation in the cortex for long times, which

might activate mechanosensitive signal transduction which in turn may alter cortical mechanics. Optical trapping, on the other hand, provides localized point measurements. In fact, it measures an effective tension though, it is difficult to characterize the cortical part of this tension [14].

High sensitivity to displacement and force measurements, and gentle micro-manipulation of the cell with optical tweezers, together with uniform distribution of cellular structures keeps it a powerful technique in cell mechanic studies. Also, compared to flat cells on a substrate, keeping cell in suspension when they are partially adherent make a 3D configuration, closer to their 3D natural environment.

In this project, we focus on optical tweezers. Using a dual optical trap (OT), it is possible to probe the viscoelasticity of suspended cells while doing active and passive microrheology to quantify the mechanical response of the cells under the various conditions.

Two particle assay has been described in the previous chapters. Here in this chapter, first we describe practical trial of cell morphology and its mechanics probed with OT. The second part indicates effects of biochemical perturbation on cell morphology. This has been done using fluorescence confocal imaging of labeled fibroblasts undergoing myosin inhibition. Lastly, in the most important section of this chapter we describe our new method that we developed to improve OT measurements to get time series of cell responses. This is a novel method to obtain time dependent behavior at the single cell level. We developed a specific microfluidic device which is optics- and bio- compatible to be able to use it in our dual optical tweezers set up. Then, as its first application we show particular usage of this device to study the mechanical responses of a single cell to biochemical perturbation.

4.2 Cellular morphology and mechanics

In this section, mechanical properties of cell lines from different morphologies (in culture), probed with a dual optical trap, are measured and their force fluctuations and stiffness are compared. We used adherent cells, 3T3-fibroblasts and MCF-7 brought into suspension and compared them with naturally suspended L-1210 cells.

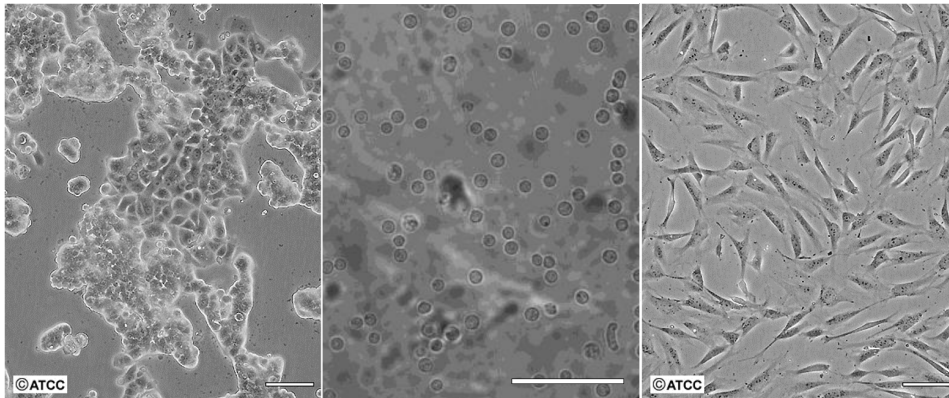


Figure 4.6.: Probed cell lines with different morphologies in culture. From left to right: MCF-7 human breast cancer cells: epithelial-like, L-1210 mouse leukemia: lymphocyte-like, and 3T3 fibroblasts cells on a culture flask. Scale bar is 100 μM . Left and right images are taken from <https://www.atcc.org/Products/Cells-and-Microorganisms>.

Epithelial-like MCF-7 human breast cancer cells and lymphoblastic-like L-1210 mouse leukemia cells, were softer than mouse 3T3 fibroblasts cells. The spring constant (stiffness) of these three cell lines, measured with the dual optical trap is shown in Fig.4.7. From 3T3 to MCF-7 and then L-1210 there is a decreasing trend in stiffness. While L-1210 white blood B-cells that can easily deform, had been even softer than epithelial-like MCF-7.

The same reducing trend also has been seen in the force fluctuation measurements (again Fig.4.7).

The aim of this experiment was to compare different cell morphologies in this experimental configuration: round but partially adherent (suspension with two particles on sides). Experimentally, it is not difficult to handle fibroblasts and epithelial-like cells in this configuration, apparently because of the adhesion receptors on their surface. Fibronectin coated beads can imitate their cultural condition which makes them form focal adhesion and helps them attach. However, L-1210s,

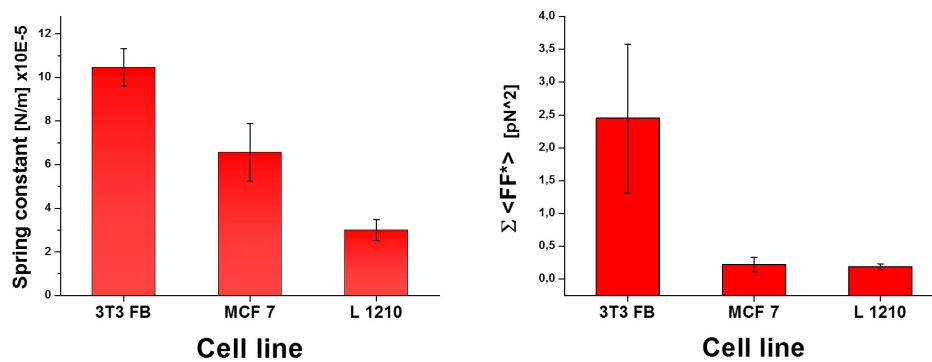


Figure 4.7.: Mechanical properties of different cell lines in suspension. Spring constant and force fluctuations of cell lines from different morphologies, brought into suspension measured via two particle microrheology using a dual optical trap. ($n=15$ for MCF-7 and L-1210) Force fluctuation and stiffness of 3T3 fibroblasts is adapted from [15].

which are naturally non-adhering, were expected to be soft and deformable. In fact, we needed to change the binding sites in order to hold them with the trapping particles (see 2.3.2). Epithelial cells, however, formed focal adhesion relatively quickly (2-3 min), but their attachment area to beads increased with time. Such that one can not hold them in this situation for longer than 15-20 min.

Force fluctuation and stiffness measurements of 3T3 fibroblasts have been shown in [15] (data is taken by the author). Force fluctuation measurements with 2-particle MR are discussed in 2.2.1 We showed that how different cellular morphology and conditions may cause different mechanical properties. We believe, a two particle assay would be more useful for fibroblasts as they are naturally bipolar adherent cells.

Data shown in Fig.4.7 is a comparison of the average values either for force or stiffness of about 15 to 30 cells for each case, and the deviation is shown as error bars. It has to be noted that practically both MCF-7 and L-1210 cells are smaller than 3T3 fibroblasts. However, size-stiffness investigation was not the aim of this experiment. Apart from that, variation from cell to cell sometimes is too high, for 3T3 cells for instance, which makes it difficult to make concrete statements [15].

4.3 Biochemical stimulation and cellular morphology

In this section we are going to depict effects of myosin motor inhibition on cellular morphology. Naturally adherent 3T3 fibroblasts brought into suspension, transfected with green fluorescent protein (GFP), were imaged by fluorescence scanning confocal microscope. Distribution of normalized volume of 15 cells before and after treating with 100 μM blebbistatin is shown in Fig.4.10.

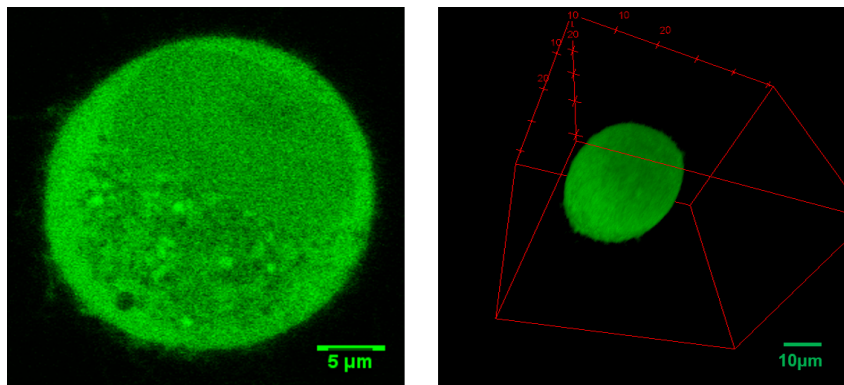


Figure 4.8.: Fluorescent confocal imaging of GFP transfected fibroblasts. GFP distributed within the whole fibroblast cytoskeleton. Cross section area of the middle plane of the cell on the left and 3D reconstruction on the right hand side is shown.

Note has to be taken that our volume measurements is based on the resolution of the scanning confocal microscope in lateral and axial directions. This together with volume regulation of the cell itself, shows variations up to 10% over time.

Moreover, we measured the volume of cells before and after treating with 10 μM Y-27632. Cross section of GFP transfected 3T3 cells and quantified volume for this treatment is shown in Fig.4.11, 4.12.

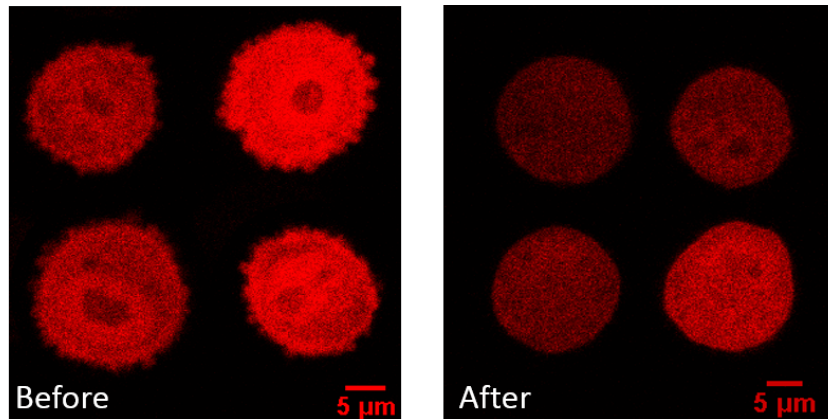


Figure 4.9.: Fluorescent confocal cross section of RFP transfected fibroblasts. Representative RFP transfected 3T3 fibroblasts before and 30 min after blebbistatin treatment. Treated cells looked round and smooth compared to the pre-treated state which showed blebbing.

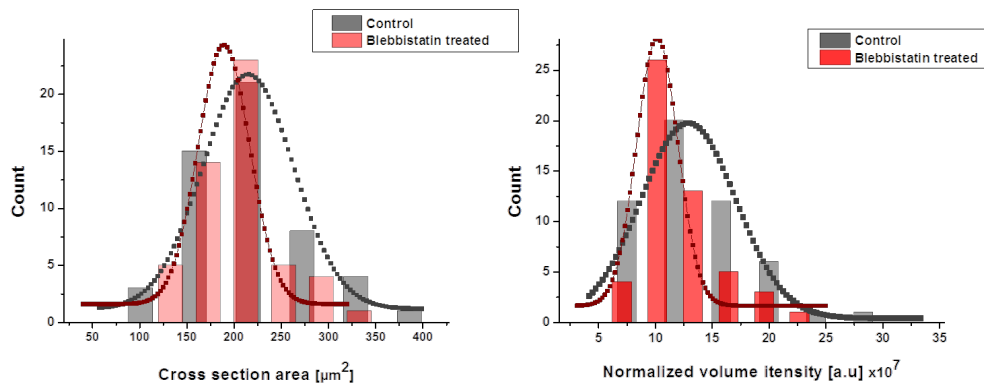


Figure 4.10.: Volume and cross section of fibroblasts changes 30 min after myosin inhibition. Treated cells with 100 μM blebbistatin on average, slightly changed their size compared to the control cells (n=52). Cross section area of the middle plane and normalized intensity of the whole cell volume is calculated.

Area and volume measurements showed slight changes after inhibition of cortical contractions.

Perturbation of cellular internal structure, such as acto-myosin contraction, is reported to change its mechanical properties specifically the cortical tension [7]. However, it does not have a significant effect on the cell volume. According to [79], theoretically even if the cortical layer of rounded-up fibroblasts totally gets disassembled, the expansion in its volume due to this pressure change would be just about 1%. This calculation is based on Laplace law of liquid in a thin shell (liquid drops), cortical tension of the spherical cell, hydrostatic and osmotic pres-

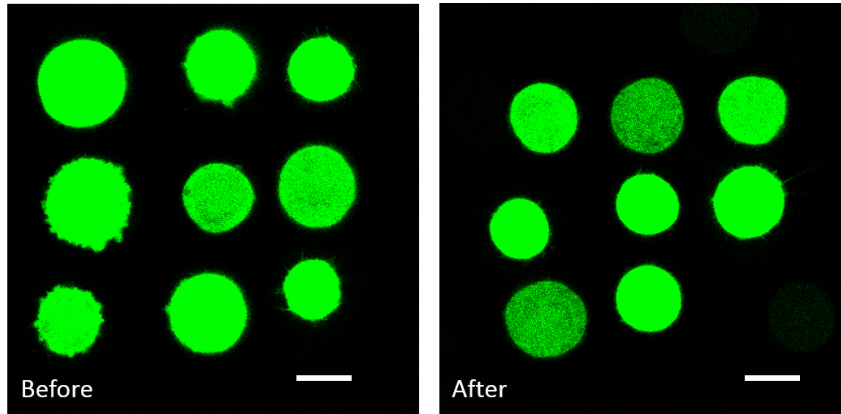


Figure 4.11.: Fluorescent confocal cross section of GFP transfected fibroblasts. Representative GFP transfected 3T3 fibroblasts before and 30 min after Y-27632 treatment (10 μM). Similar to cells treated with blebbistatin, less blebs have been seen on the cell cortex (scale bar 10 μm).

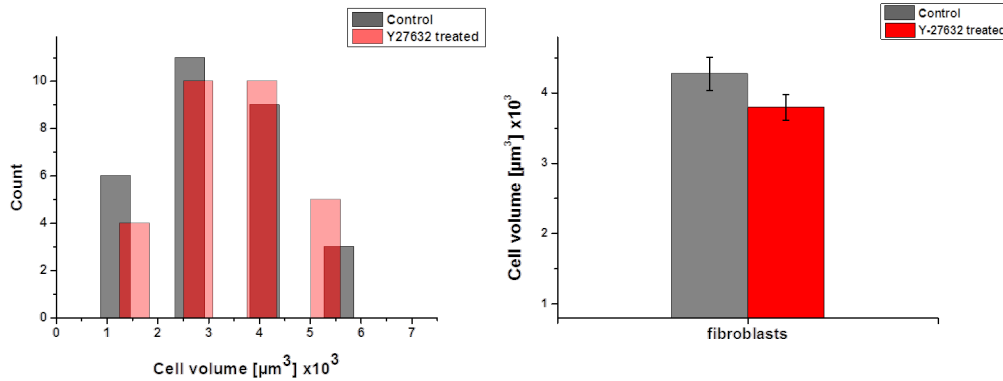


Figure 4.12.: Volume of fibroblasts changes 30 min after Y-27632 myosin inhibitor. Treated cells with 10 μM Y-27632, on average slightly changed in volume compared to the control cells (n=29).

sure changes (see 5.1).

It is observed by (Stewart et al.2011), that 90% reduction of cortical tension caused very small increase in volume [2],[68]. Description of the model and calculations will be explained in the next chapter. However this argument in conjunction with the experimental results clarifies that osmotic pressure is responsible for expansion or compression of the cell rather than the cell cortex.

4.4 Cellular mechanics and biochemical stimulation (novel approach)

Myosin activity has been proven to increase the stiffness of adherent cells to a substrate, but few studies have been done on suspended cells when substrate is not playing a role.

Regarding mechanical and rheological changes due to myosin force generation, up to now most of the studies were focused on the cell adhere to a 2D substrate, which makes them flattened and very stiff. As a result of spreading on a substrate and getting flat, inhomogeneity in structure and organelles' distribution affects local force measurement. For example AFM force-indentation measurements varies according to the position of cantilever on the specimen.

On the other hand, mechanical properties of suspended cells has been investigated recently using an optical stretcher, with no contribution of adhesion to a substrate. In this study, however, using optical trapping we suggest a methodology between these two extremes. First, we take advantage of homogeneous network distribution of rounded-up cells. Since there won't be any anchors to the substrate, we can precisely track the displacements of the particles in order to measure the effective cellular force transmitted to the particles on sides. Secondly, adherent cells brought into suspension and held by beads on opposite sides start forming focal adhesions next to the beads. For instance, for fibroblasts which like to get mechanical support, this is a favorable configuration and similar to their 3D physiological condition. For naturally non-adherent cells, binding to the trapped particles is a practical way to prevent them from rotating during experiment.

4.4.1 Microrheology inside a microfluidic device

Using a dual optical trap makes it possible to probe the viscoelasticity of suspended cells by active and passive microrheology to quantify the mechanical response of the cells under the various conditions. The previous study revealed high variation from cell to cell, always making it difficult to interpret possible changes under different environmental stimulations [15]. Using a custom built membrane integrated flow chamber technique, we are able to get the time series responses of the single cell to various stimuli such as biochemical perturbation. We use a custom-designed microfluidic device made of NOA 81 with integrated hydrogel micro-windows to rapidly change solution conditions for suspended cells held by optical traps without direct fluid flow. In our previous chapter, we showed how potential diffusion based movement of the molecules occurs through the hydrogel

windows together with evidences of drug diffusion.

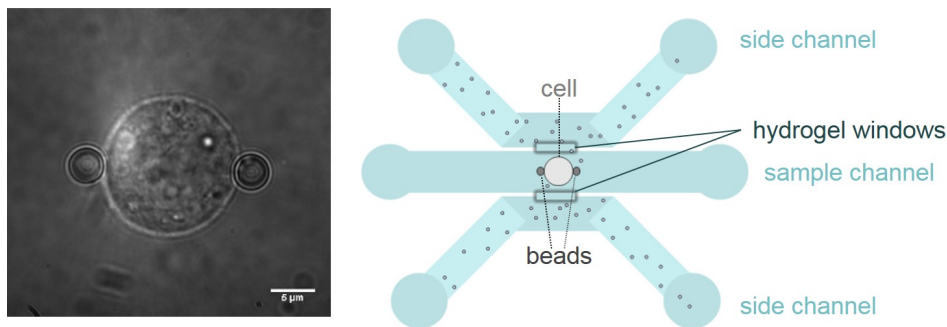


Figure 4.13.: Two particle microrheology in a microfluidic device. Suspended fibroblast held by two trapped micro-beads (left) and sketch of cell suspended in our flow chamber while molecules are diffusing through the connecting hydrogel membrane windows (right).

We investigated the role of motor contractility in stiffness of the suspended cells individually. It has been shown that when myosin contractility is turned down using inhibitors, it reduces the cortical tension (Tinevez et al.2009). But we were wondering whether it changes the stiffness of the whole cell body and thereby its force generation. Contradictory effects have been reported for the averaged stiffness of cells from a particular type. Thus it would be interesting to track individual single cells during treatment and afterward in recovery period. Doing microrheology with an optical trap has made it possible to measure the cellular force generation below pN and see how it changes during different treatments.

4.4.2 Results

In this section the mechanical properties of individual 3T3 fibroblasts, suspended in the microfluidic device and probed with two-particle-microrheology, will be presented in the following order: First long-term stiffness control without any drug interference is shown. Secondly, the results of myosin inhibition obtained with two pharmacological drugs, blebbistatin and Y-27632, is presented in two steps: a) Spring constants, b) Force fluctuations. Lastly, cell recovery will be explained and the chapter will be ended with a discussion.

1. Long term stiffness control

As we're concerned about an effective stiffness of the cell in this experimental configuration (two trapped particles attached to opposite sides of the cell via focal adhesions), had to make sure that it would not get changed due to prolonged suspension.

Before starting with biochemical interference, as a control experiment we measured time dependence of the cell stiffness inside the flow-chamber held with trapped beads. For ten individual cells we recorded displacements and measured the stiffness in time windows of 10 to 20 min for two hours, without any drug interference. In fact, we wanted to see whether this experimental configuration (suspending cell between trapped beads) influences the cell response.

Stiffness measurements as explained before were obtained using AOD, applying oscillatory force on one of the beads. Position of both beads were recorded and based on their displacements, we could get force versus elongation curves. Cells who experienced slow oscillation showed a linear response to small amplitudes of deformation, thus we could use Hook's law for linear springs to derive the spring constant as their stiffness. During this work, we oscillated the bead with 0.2 Hz and about 500 nm amplitude.

The results showed less than 10% (on average 6%) variation in stiffness for each individual cell within a period of two hours (Fig.4.14). Meaning, for future experiments variations above this variation should be considered as an effect of other environmental stimuli.

On the other hand, our long-term measurements inside the micro-device can prove the strength of our methodology (two particle assay). Indeed long-term tracking of mechanical responses of suspended cells, did not show significant change due to light or heat damage.

2. Blebbistatin treatment

a) Spring constant

After long-term control experiments, stiffness measurements of fibroblasts cells, disturbed with 100 μ M blebbistatin were conducted. Initially a suspended cell was held by trapped particles in its culture medium. The same medium (without any drug) filled up the side channels of the microfluidic chamber (introduced in previous chapter). Then it continued with blebbis-

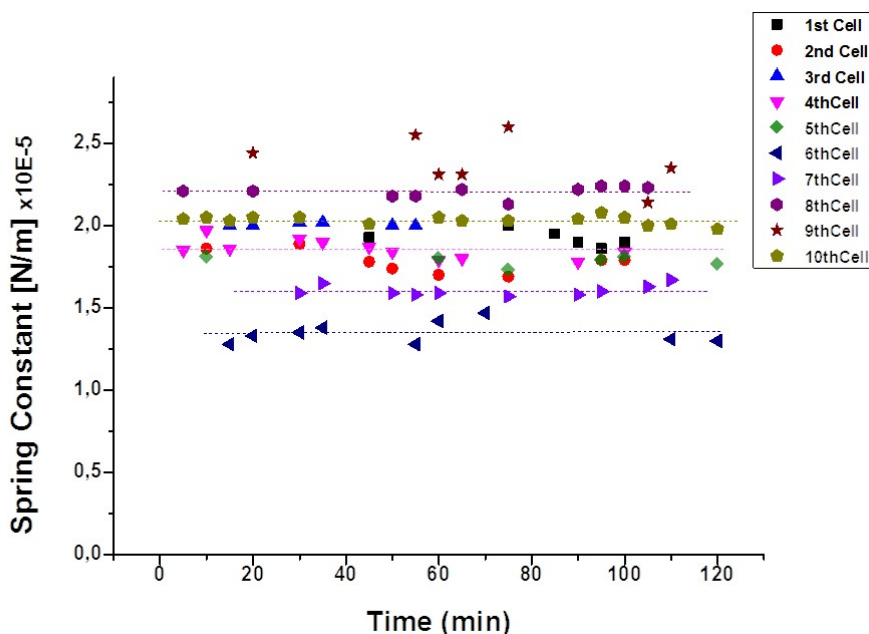


Figure 4.14.: Long term stiffness measurements of cells suspended in the flow chamber. Spring constant of fibroblasts held by two trapped particles inside the microfluidic device without any drug interference. Stiffness measurements are based on simple spring model for cells.

tatin solution diffused through the hydrogel membrane. The cell stiffness was measured while AOD was oscillating one of the particles (0.2 Hz and 500 nm amplitude) and we kept recording the beads positions in time windows of 10 to 20 minutes. In total, the measurement lasted about one hour after blebbistatin diffusion. In order to reduce any possible damage, we turned down the laser intensity in between the measurement steps.

Fig.4.15 shows the time series of cell stiffness, before, right after and later on in the presence of blebbistatin. This plot shows the cell stiffness when myosin is prevented from contracting actin filaments on the cortex. Tension relaxation through the cortex in the absence of myosin activity, initially made us expect cell softening after blebbistatin, but interestingly in some cases the spring constant increased, which means cell got stiffer. Time series data points did not show significant variations from 10 to 50 min after drug perturbation. Therefore we used the time-averaged values for later comparisons (note to small error bars in Fig.4.16).

We obtained time-averageds of cell stiffness from 10 to 50 min after

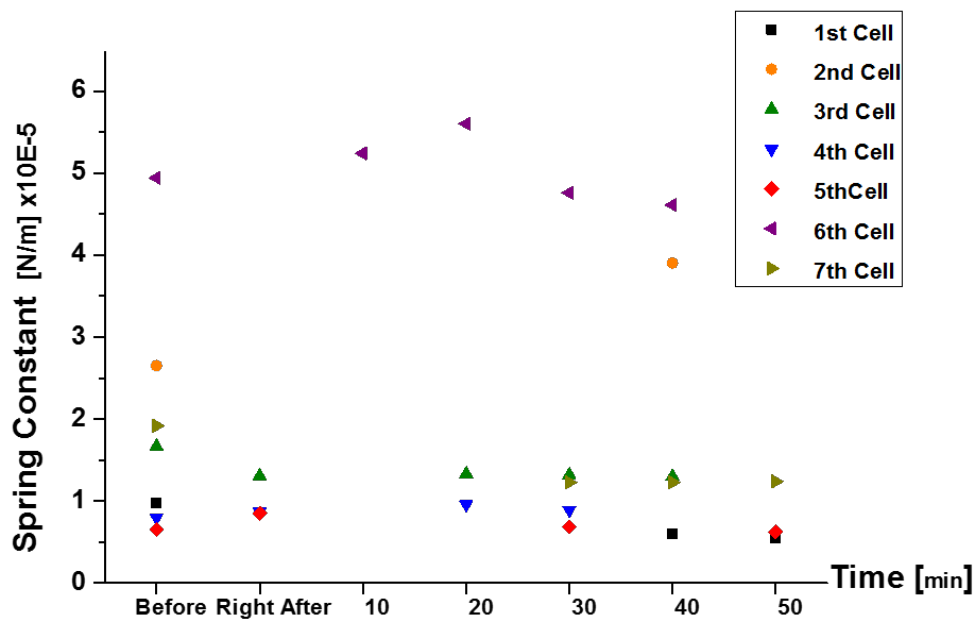


Figure 4.15.: Time series of the spring constant of blebbistatin treated 3T3 fibroblasts. Spring constants of fibroblasts held by two trapped particles inside the microfluidic device, before and after blebbistatin ($100 \mu\text{M}$) addition. We followed individual cells in time windows of 10 min.

myosin inhibition, and plotted cell spring constant versus stiffness of the trap, and compared the values before and after drug perturbation (see Fig.4.16). For better visualization, calculated stiffness difference for each individual cell is depicted in percentage. Obviously, some of the myosin inhibited cells got softer (negative percentage values), however some became stiffer (represented with positive values) and in two cases with $< 10\%$ change, drug addition had no obvious effect. Apparently, this varying behavior is independent from the strength of the trap.

b) Force fluctuations

In addition to stiffness measurements, one can turn down the AOD oscillations and record the beads' displacements caused only by the cell located between them. As mentioned before, two particle passive microrheology,

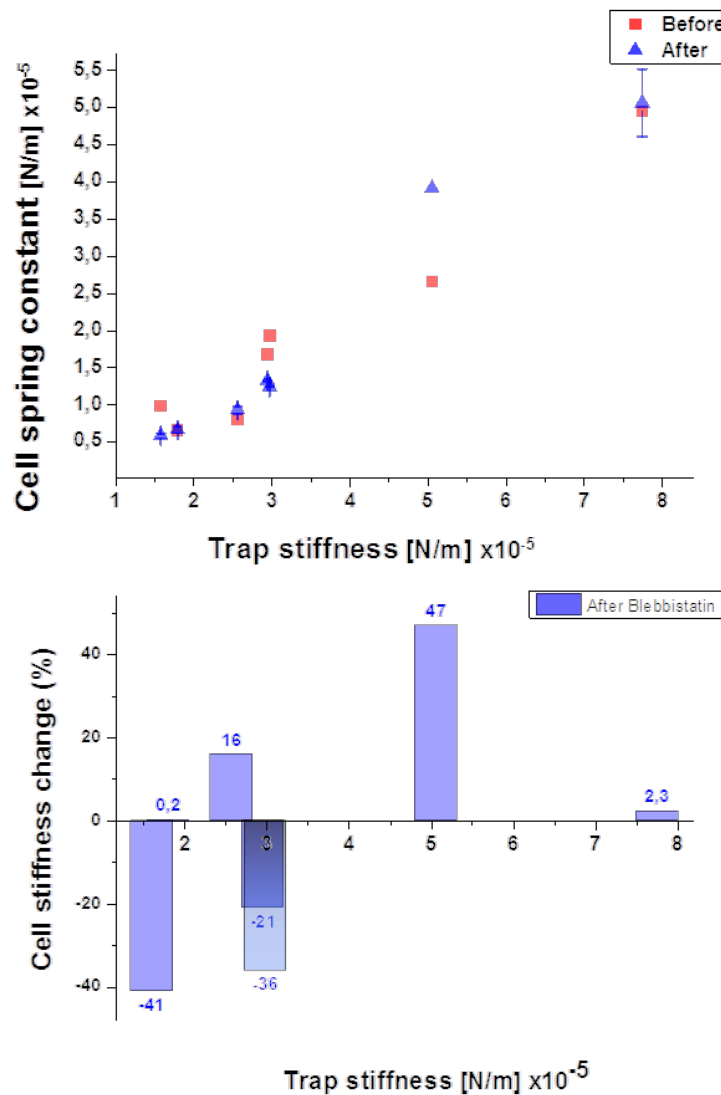


Figure 4.16.: Spring constant of blebbistatin treated 3T3 fibroblasts. Fibroblasts held by two trapped particles inside the microfluidic device, before and after 100 μM blebbistatin treatment. Top panel: comparison of cell stiffness before and after treatment is shown. Blue triangles depicted time-averaged of cell stiffness from 10 to 50 min after drug diffusion into the channel. Bottom panel: relative change of the cell stiffness after blebbistatin is plotted.

lets us measure the force transmitted to the beads which was generated by the cell. It is interesting to see whether myosin inhibition is affecting the force sensed by trap particles. So with same conditions of a cell in a microfluidic chamber and working solution, we followed the particles' displacements and measured the force. In Fig.4.17, time series of force gen-

erated by 3T3 fibroblasts is shown gradually decreasing when blebbistatin inhibits myosin contractions.

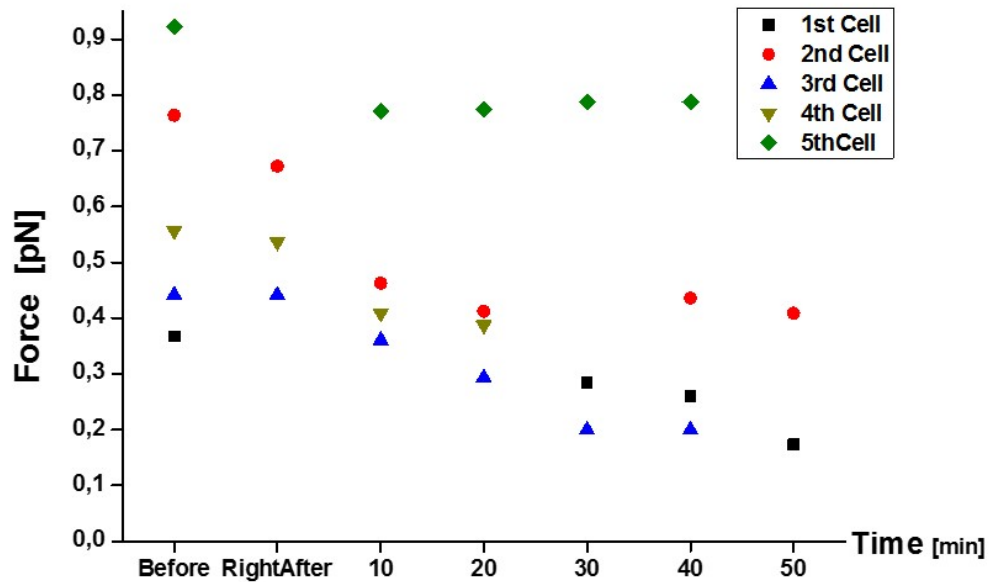


Figure 4.17.: Force fluctuations of blebbistatin treated 3T3 fibroblasts. Force generated by fibroblasts held with two trapped particles inside the microfluidic device, before and after blebbistatin ($100 \mu\text{M}$) entering the channel. We followed the cell in time windows of 10 min.

The clear drop in force, confirmed the presence and functionality of the drug and proved myosin's role in cortical force generation. Apart from that, we compared the time-averaged of the force within 10 to 50 min right after blebbistatin addition, to the cellular force before hand. The result is shown in Fig.4.18. In order to simplify the comparison, the drop of measured values in each case is indicated in percentage.

3. Y-27632 treatment

In order to get a better impression of myosin's role in stiffness and force fluctuations of suspended cells, we tried another pharmacological drug Y-27632. It decreases phosphorylation of myosin light chain and thus inhibits

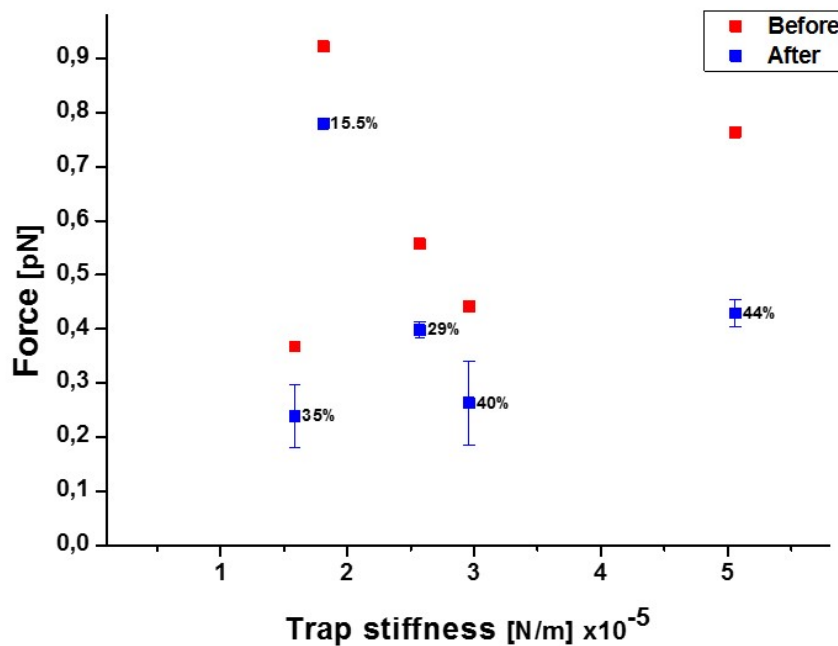


Figure 4.18.: Force generated by blebbistatin treated 3T3 fibroblasts. Force generated by fibroblasts held with two trapped particles inside the microfluidic device, before and after $100 \mu\text{M}$ blebbistatin was added. Blue squares depict the time-averaged of the total force, from 10 to 50 min after drug diffusion into the channel. Relative drop in force after treatment also is shown in percentage.

acto-myosin contraction (see [80], more detail in section 4.1.3). Details of the experimental approach from device geometry to cell manipulation are similar to what was used for blebbistatin, except that $20 \mu\text{M}$ Y-27632 is used to disturb 3T3 fibroblasts.

a) Spring constant

Spring constants of 3T3 fibroblasts before and after Y-27632 treatment together with the relative change caused after treatment are shown in percentages (Fig.4.19).

As for the blebbistatin, the individual cells showed both softening and stiffening after myosin inhibition by Y-27632, which in one hand revealed the

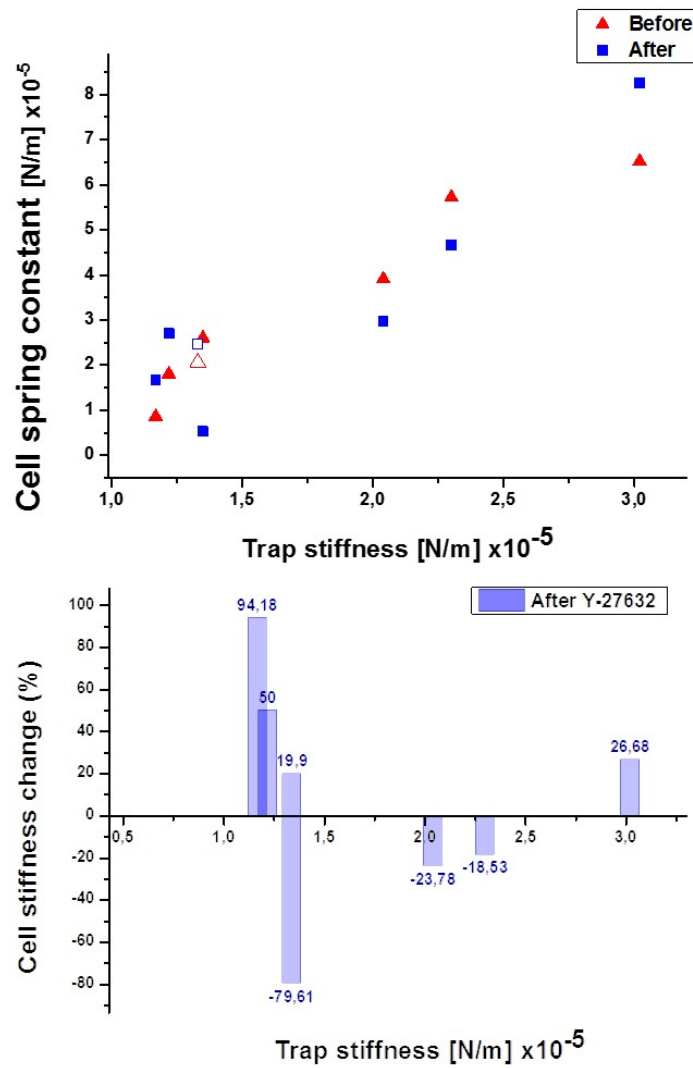


Figure 4.19.: Spring constant of Y-27632 treated 3T3 fibroblasts. Fibroblasts held by two trapped particles inside the microfluidic device, before and after 20 μ M Y-27632 treatment. On top, comparison of cell stiffness before and after treatment is shown. Blue squares depict time-averaged of cell stiffness from 30 to 60 min after drug diffusion into the channel. At the bottom, relative change of the cell stiffness after Y-27632 is plotted.

variable response from cell to cell, but more importantly it means myosin itself has no clear effects on stiffness of the whole rounded-cell body.

b) Force fluctuations

Same as blebbistatin, the force generated by 3T3 fibroblast, before and after Y-27632 treatment together with relative drop in force after treatment is shown in percentage in Fig.4.20

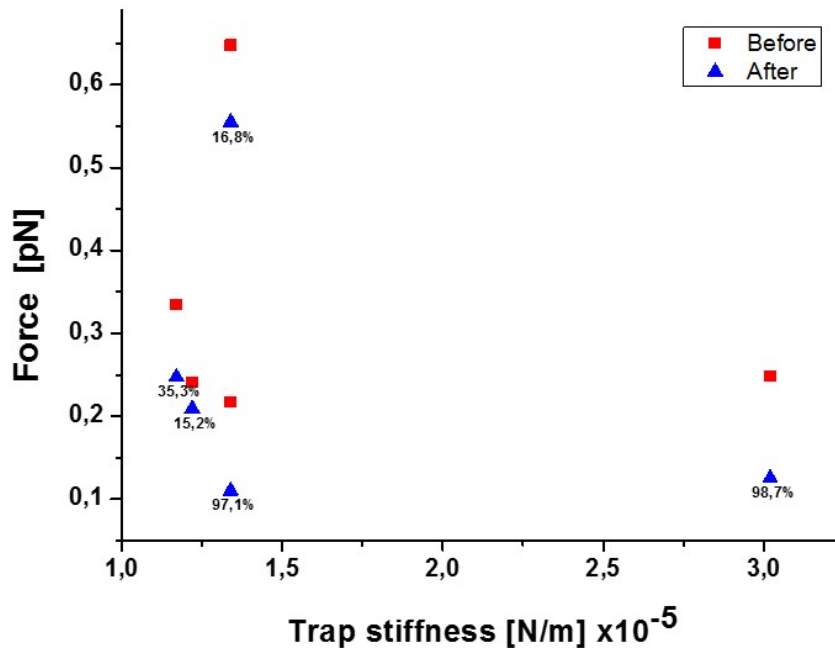


Figure 4.20.: Force generated by Y-27632 treated 3T3 fibroblasts. Force generated by fibroblasts held with two trapped particles inside the microfluidic device, before and after 20 μ M Y-27632. Blue triangles depict time-averaged of the total force, from 30 to 60 min after drug diffusion into the channel. Relative drop in force after treatment also is shown in percentages

The measured force of fibroblasts after Y-27632 decreased for all individual cells. These results are similar to blebbistatin treatment. As we expect, in absence of myosin contractility on the cell cortex, fluctuations of the force transmitted to trapped beads decrease. We again take this force reduction as a proof of drug diffusion through HMM.

4. Cell recovery

Membrane integrated micro-devices provide the opportunity for rapid exchange of the side-solutions simultaneous to two-particle-microrheology

in the central channel. By this we can track the single cells before the treatment until the end of recovery time. Time series of changes in mechanical properties such as force generation and stiffness of the cell can illustrate the required time for cell to recover. Furthermore, we can play with single drug concentration or even mix them.

We followed individual cells treated with myosin inhibitors (introduced in 4.1.3), from the beginning through the treatment period and continued with the recovery time when the drug was washed out. Different concentrations of blebbistatin and Y-27632 were infused to the side channels while stiffness of the cell was measured for one hour of treatment and then one hour after drug solution was washed out (Fig.4.21, top panel).

We took the time-averaged of cell stiffness from 10 to 60 min of treatment and compared it with recovery values. Although there is variation from the mean, it is evident that cells actively attempt to recover (Fig.4.21, bottom panel).

In fact, the aim of these experiments is first to prove the device capability, showing its potential for further analogous studies. Second, to address the question whether cell can recover after myosin inhibition or not. Additionally demonstrating the ability of this methodology to drive the cellular recovery time. Indeed, our preliminary results of the cell recovery looks promising for further investigations.

4.5 Discussion

In this section, we first investigated the role of non-muscle myosin II inhibition on cell stiffness. When myosin pulls on actin stress fibers it generates active stress, which causes the cell to become stiff and more solid-like.

Cell softening due to myosin inhibition on time scales of seconds has been reported for cells adherent to a substrate. According to (Martens et al.2008), it can be the result of reduction in cellular pre-stress in the absence of myosin activity.

However, (Schlosser et al. 2015) showed that blebbistatin, on average, reduced the stiffness of fibroblasts about three times lower. But due to the noticeable cell to cell variation, further investigation is needed to make generalization.

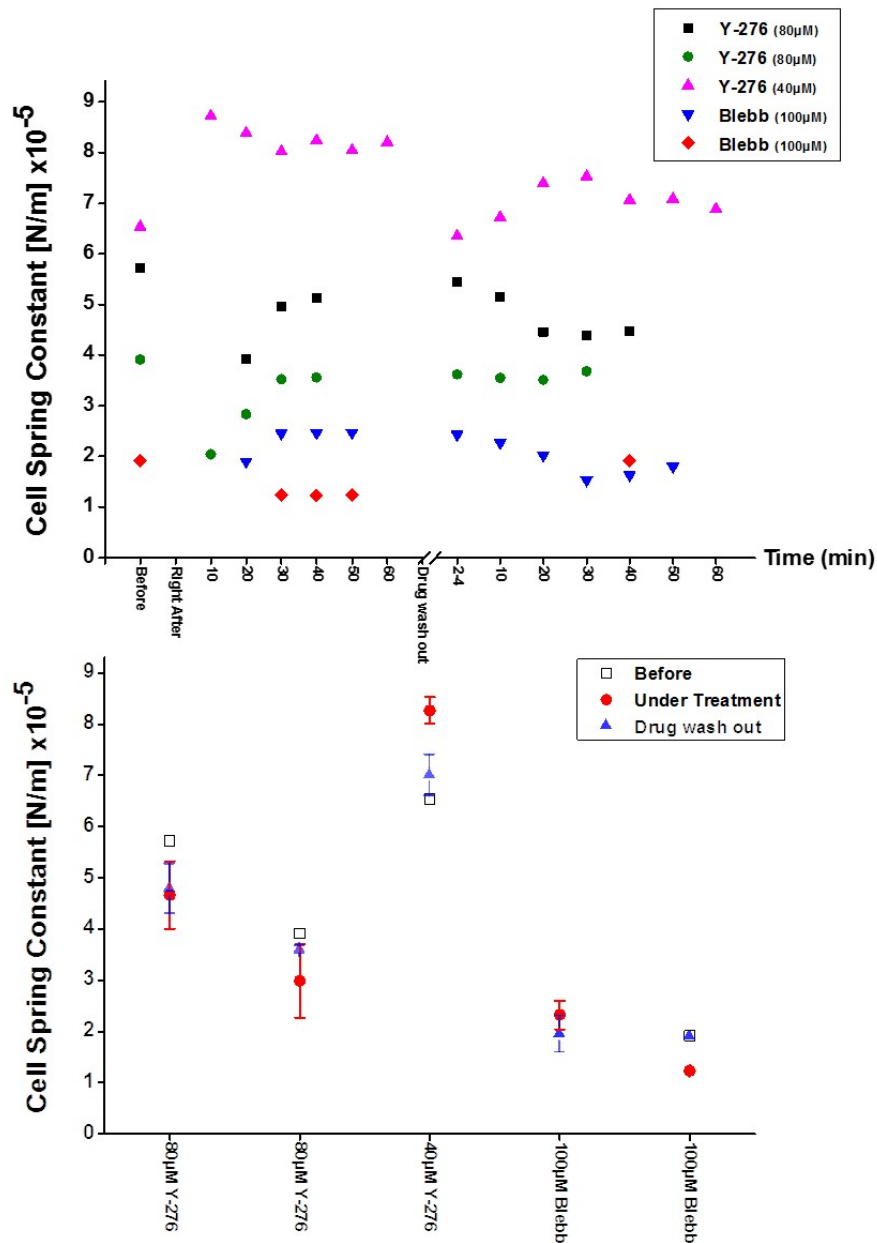


Figure 4.21.: 3T3 fibroblasts stiffness during treatment and recovery. Top panel: Time series of cells before and under myosin inhibitors treatment for an hour, continued afterward when drug is washed out. (Blebb and Y-276 are abbreviation for Blebbistatin and Y-27632 inhibitors respectively.) Lower panel, average cell stiffness during treatment is compared to the recovery time (from 10-60 min), and before hand (Error bars are showing deviation from the mean).

Though, (Chan et al. 2015) using an optical stretcher demonstrated that non- adherent blood cells (e.g. HL 60 Leukemia), cells in mitosis, and nat-

urally adherent cell brought to suspension (e.g. 3T3 fibroblasts and HeLa cells) got stiffer and more solid-like upon non-muscle myosin II inhibition. In other words, myosin activity increases the cytoplasm fluidity in these cases. In addition to pharmacological inhibitors, they knocked down myosin II and again noticed a drop in cell compliance on time scales of seconds. Using the standard linear liquid (SLL) model they described 3-4 sec creep deformations of the cell and concluded myosin activity increases the fluidity of fully suspended cells free from any attachment.

Manipulation of micro/nano-particles has been shown to be capable of characterization active cellular force generation of pN to nN (Leu et al. 2003). In this work, we used it to quantify the effects of two pharmacological inhibitors of myosin II activity on the stiffness of suspended cells.

The amplitude and time scale of the cell deformation obtained by trapping particles, is less than 10% of its radius within 5 seconds (500nm and 0.2 Hz). This is the result of the cell stiffness, by taking average in periods of 10- to-50 min after drug addition compared to the stiffness before treatments; 57% of cells treated with Y-27632 (20mM) showed stiffening and 43% got softer (see Fig.4.19). Blebbistatin treatment also revealed 42% softening, 28.6% stiffening and no significant change in the stiffness has been seen for the rest (28.6%). For both treatments, the comparison is between cells' stiffness before the drug and it's averaged value in a period of 10 to 50 min after drug addition (Fig.4.15, 4.16). But force fluctuations of all the cells treated with both blebbistatin and Y-27632 showed the same descending trend in force fluctuations.

Apparently, myosin contraction has no clear effect on cell stiffness: neither among cells treated with Y-27632 nor among blebbistatin treated ones. But the total cell generated force is reduced.

Thus, based on our results, we conclude that despite the important role that has been shown for non-muscle myosin II in cytokinesis, cell motility and cortex tension, it reduces the force fluctuations but not necessarily the stiffness of the cell body. We hypothesize that in non-adherent cells, myosin generated contractility is not strong enough to determine the cell stiffness alone. In fact, a closer look at the single cell level can explain the previous contradictory reported literature (Schlosser et al.2014 and Chan et

al.2015) about myosin II activity softening or stiffening the suspended cell. We show that small and slow deformations of naturally adherent cells brought into suspension (particularly 3T3 fibroblasts) exhibit different behavior in response to myosin activity inhibition (500nm and 0.2 Hz). We use Hook's law for simple spring model. Driven spring constant showed the cell stiffness which was tracked before and after treatment. As a result, we have seen both an increase and decrease in stiffness of the suspended fibroblasts held by dual optical trap due to myosin contraction inhibition which was independent of the trap stiffness.

Indeed, dynamics of molecular scale interactions on the cortex is poorly understood. But a possible reason for this behavior is that after myosin inhibition, suspended cell may undergo cytoskeletal remodeling. There is some evidence that the tension built up by myosin applying compressive stress on actin filaments causing buckling or breakage. This fragmentation and compaction may contribute to actin turnover and cortex reorganization, hence possibly changing cortex elasticity. Rearrangement of membrane-to-cortex linkers also might have a role in cell stiffness [81].

As mentioned, myosin II is not the only cellular machine playing a role in force distribution along the cell cortex. Together with myosin motors, some cross-linking proteins are also involved in the force applied on the cortex. Thus, the absence of myosin may increase the binding rate of crosslinkers such as α -actinin and hence compensate the force [8].

According to (Chan et al. 2015), in the absence of myosin activity F-actin dominates the cell deformation and hypothetically myosin plays a role in actin depolymerization.

Taken together, complexity of the cortical and internal structure of rounded cells keeps the role of myosin in mechanical properties of this active network still open for further investigations. We hope our prototype introduced here, can help to address related questions in cell mechanics. With the aid of our flow-chamber introduced here probing actin polymerization processes simultaneously with myosin perturbations, or knocking down the myosin, seems to be a helpful aid to address these questions in future.

Cell mechanics under osmotic pressure

“Osmotic forces are unexpectedly great: with 1% sugar solution can be equal to 2/3 atm.”

Jacobus H. van't Hoff

5.1 Theory: osmotic pressure, cortical tension and cell volume

Living cells of both plants and animals are enclosed by a semi-permeable membrane that regulates the flow of liquids, dissolved solids and gases into and out of the cell. This membrane forms a selective barrier between the cell and its environment such that water molecules, for instance, can pass through the membrane.

Osmosis balances the pressure and concentration of solution on both sides of the semi-permeable membrane by making water molecules move from the high-concentration side to the low-concentration side. Based on this fact, tonicity is defined as the relative concentration of solutes dissolved

in a solution like water. When two environments are isoton, the total molar concentration of dissolved solutes is the same in both of them. When cells are in isotonic solution, movement of water out of the cell is balanced by movement of water into the cells. But if cells are placed in hypertonic solution (higher solute concentration and less water than normal cell medium), they will lose water and shrink. Contrarily, in hypotonic solution (less solute and more water), they absorb water and swell.

As water is incompressible, fluid flow is directly related to the cell volume. In both cases cell cortex, together with cytoplasm have to guarantee integrity of the cell.

Moreover, volume and shape regulation has a big impact on cell mechanics. Therefore, this chapter focuses on osmotic pressure which is the most dominant factor in cell volume to investigate mechanical properties of cells.

Unlike plant and bacterial cells, animal cells have no rigid cell wall to resist large changes in cell volume, instead membrane and cortex tension, active contractility and water flows all are contributing to control the cell shape and volume [1].

For better understanding of the control mechanism of volume and shape in animal cells, first we briefly introduce 'cortex tension' of the cell.

- Cortical tension

Tension is the sum of all forces within a material. Tension in the cell cortex is the local stress distributed in the cortical network integrated over the thickness of the cortex. It can be interpreted as the force per unit area in the network.

Eukaryotic cells, are made of a bilayer lipid membrane and an acto-myosin cortex beneath that. Since these two are tightly coupled, the total surface tension is a combined results of the membrane and underlying cortical network properties. Fig.5.1 shows the tension in plasma membrane γ , and the cortical tension T_{cortex} .

According to (Tinevez et al.2009) and (Kruse et al.2004), cortical tension, T_{cortex} , itself has two compartments: active (T_{active}) and elastic ($T_{elastic}$). T_{active} is the result of active processes in the cortex such as myosin mo-

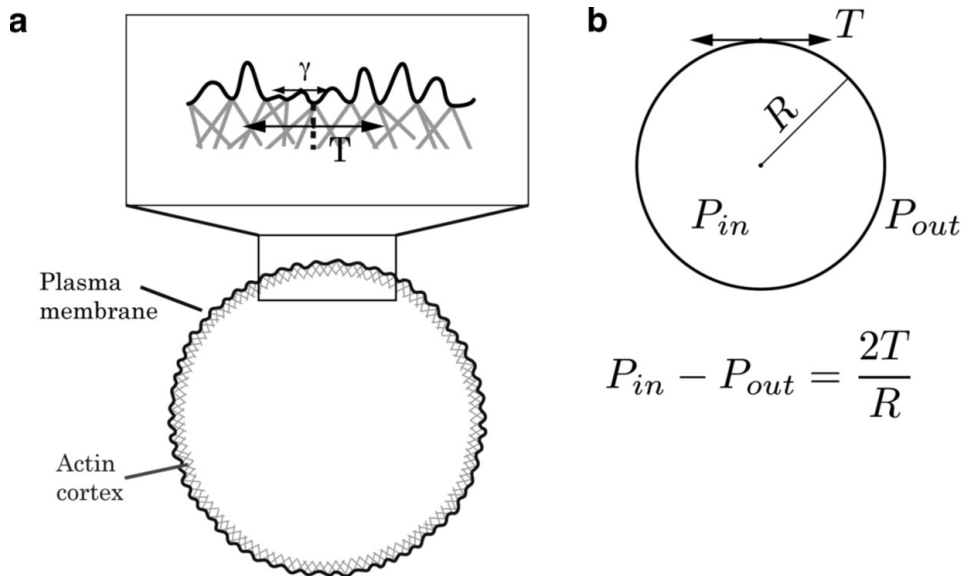


Figure 5.1.: Surface tension and intracellular pressure. a) In most of eukaryotic cells, a network of cross-linked actin filaments is tightly attached to the plasma membrane. Surface tension of the cell is a combination of tension in the plasma membrane γ and the cortical actin network T . b) Tension in cell cortex generates a hydrostatic pressure on the cytoplasm. Laplace law relates the difference between intracellular pressure P_{in} , and external pressure P_{out} , for a cell with radius R , and tension T . Picture is reprinted from [79].

tors pulling on the actin network. It depends on energy provided by ATP hydrolysis, as well as concentration and activity of the myosin motors. However $T_{elastic}$ becomes important usually in the presence of deformations or flow and depends on viscoelastic properties of the cortex [7],[82]. Before going to the experimental details, let's compare the contributions of osmotic pressure and cortex tension in the cell volume.

- Contribution in the cell volume

In a steady state, volume of rounded-up cells (ideally spherical) is fixed with no net flow of water through the cell membrane. That means, hydrostatic pressure on cell is equal the osmotic pressure across the membrane ($\Delta P = \Pi_{in} - \Pi_{out}$).

Based on Laplace law, hydrostatic pressure on spherical the cell wall is $\frac{2T}{R_c}$, when T is the cortex tension, R_c is the cell radius. So we can write

$$\frac{2T}{R_c} = \Pi_{in} - \Pi_{out}. \quad (5.1)$$

Nevertheless, osmotic pressure depends on solute and water mole numbers in both sides. Van't Hoff's law gives the intracellular osmotic pressure:

$$\Pi_{in} = \frac{n_{osm}R\theta}{V_c} \quad (5.2)$$

where n_{osm} number of moles of intracellular osmolytes, R is the gas constant, θ is temperature and V_c is the cell volume:

$$\frac{2T}{R_c} = \frac{n_{osm}R\theta}{V_c} - \Pi_{out} \quad (5.3)$$

$$\Rightarrow V_c = \frac{n_{osm}R\theta}{\Pi_{out} + \frac{2T}{R_c}} \quad (5.4)$$

Substituting the extracellular osmotic pressure ($\sim 10^5$ Pa) for physiological media and typical cortical tension of fibroblasts cells (500-1000 pN/ μ m), one can see the $\frac{2T}{R_c}$ term is orders of magnitude smaller than the osmotic term Π_{out} [7].

In fact, even dramatic change in cortical tension will not have a big influence on the cell volume since extracellular osmotic pressure is much more higher than that. For instance, reducing the cortical tension from 2500 to 10 pN/ μ m results in difference hydrostatic pressure of 1000 Pa, which is equal to 1% of the extracellular osmotic pressure ($\sim 10^5$ Pa). Such a drop in pressure will cause just 1% expansion in volume. This means, cortex alone can not be responsible for cell expansion or shrinkage due to the pressure difference [7].

It has been experimentally proven by (Stewart et al.2011) that actin depolymerized cells, even after 90% drop in cortical tension, showed a small volume expansion instead of immediate bursting. Our result presented in last chapter 4.3, also confirms this idea; volume measurements of myosin inhibited fibroblasts, in average, did not show significant difference in cell volume. Therefore, the contribution of cortical tension is not significant.

Nevertheless, due to the term $\frac{2T}{R_c}$, the cell swelling or shrinkage is slightly different from van't Hoff law' prediction. A 'perfect osmometer' is a spher-

ical body that its volume in response to variations in solute concentration of the suspending medium Π_{out} , obeys van't Hoff law. However, [83],[84] experimentally confirmed that a living cell is not a perfect osmometer.

5.2 Experimental approach

In this section, force measurements of suspended cells under different osmotic conditions, in two parts will be described; the first part has been done when cells were placed in a conventional cover-slips macro chamber and the second part, cells were probed inside our new microfluidic device. Performing these two experiments verifies the advantages of our new technique of probing cells rather than the conventional method.

5.2.1 Single step osmotic change in conventional macro-chambers

Initially we started with a single step, harsh tonicity change of the cell medium in a macro-fluid-chamber:

Confocal imaging of cells in their culture medium was recorded. After 3D reconstruction of the image stacks, the cell volume was calculated. We tried to record the volume fluctuations of the cell suspended in a macro-chambers for 10-15 min. Then high concentration of sugar was added, to finally provide a certain hypertonic sugary medium for the cell (10% D-sorbitol). Within a few seconds it got shocked and dramatically shrink. However, after a few minutes, it relaxed and got slightly increased in volume (but still not to its initial size).

Fig.5.2 shows volume fluctuations of a 3T3 fibroblast in an isotonic media, then shrinkage due to an osmotic shock by 10% sorbitol solution, followed by slow adaptation to the applied level of tonicity and relaxation, $\frac{V_2}{V_0} \sim 70\%$ (or $\frac{R_2}{R_0} \sim 90\%$).

Under the same experimental condition mechanical properties of L-1210 cells, first in the isotonic solution (their cultural medium), and then in the hypertonic sugar solution (500 mM D-sorbitol dissolved in culture medium) were probed with a dual optical trap.

Mechanical properties of cells undergoing this compression is explained in the result section 5.3.1.

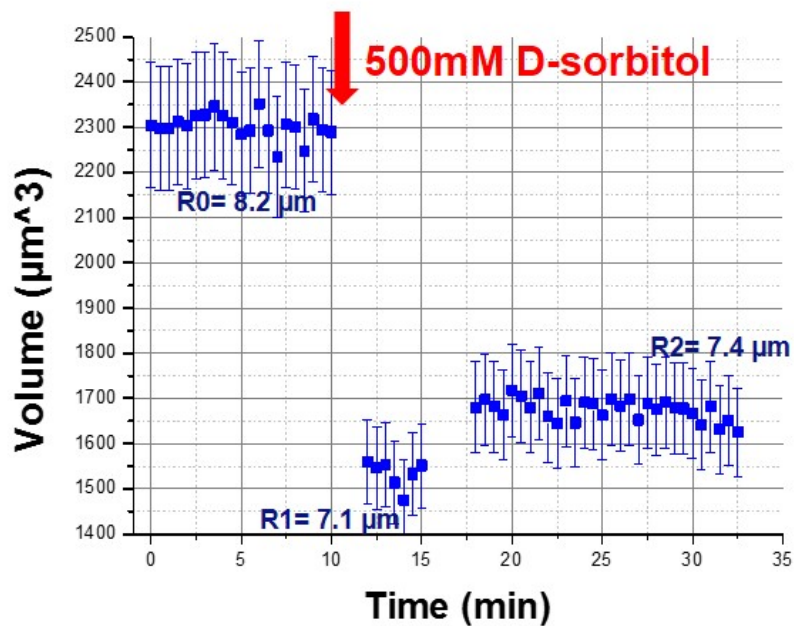


Figure 5.2.: Cell volume changes in hypertonic medium. Volume fluctuation of 3T3 fibroblast before and after adding sugar(500 mM D-Sorbitol). Volume calculation is based on confocal image stacks after 3D reconstruction. R0, R1, R2 are the mean value of cell radius subsequently before, during and after osmotic shock (error bars <10%).

5.2.2 Multi-step osmotic change in a novel microfluidic chamber

Thanks to specification of our new microfluidic chamber, especially the hydrogel membrane fabricated between side and sample channels, we were able to rapidly exchange the osmolytes and expose single cells to multi step osmotic changes in a controllable way (see 3.4.3).

In order to test the diffusion of sugar molecules through the hydrogel membrane, 3T3 fibroblasts were put in the central channel of the micro-chamber. Side channels had been filled with the cell culture medium, resulting in an isotonic environment for the cells in the neighbor channel. Then they were exposed to a rapid exchange of extreme hypo and hypertonic medium (100 mOsm and 800 mOsm). Accordingly the cells swelled or shrank. Fig.5.3 demonstrates how a cell responds to this environmental change. Quantification of the cell size is presented in Fig.5.4.

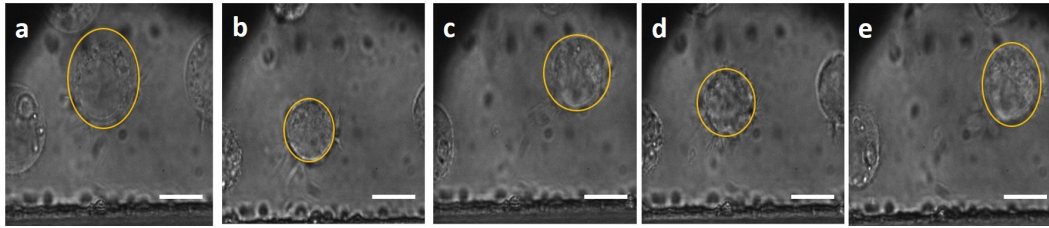


Figure 5.3.: Rapid exchange of side-solutions makes a cell in the middle channel swell or shrink. Rapid exchange of the side solution from extreme hypo- to hyper-tonic and vice versa causes a 3T3 cell in the middle channel swell or shrink. Side solution was repeatedly changed from a) extreme hypotonic 100 mOsm/kg to b) extreme hypertonic 800 mOsm/kg, continued with c) mediated concentration 500 mOsmol/kg, then d) again to 800 and finally e) 500 mOsm/kg. The cell size is quantified in Fig.5.4 (scale bars: 10 μm).

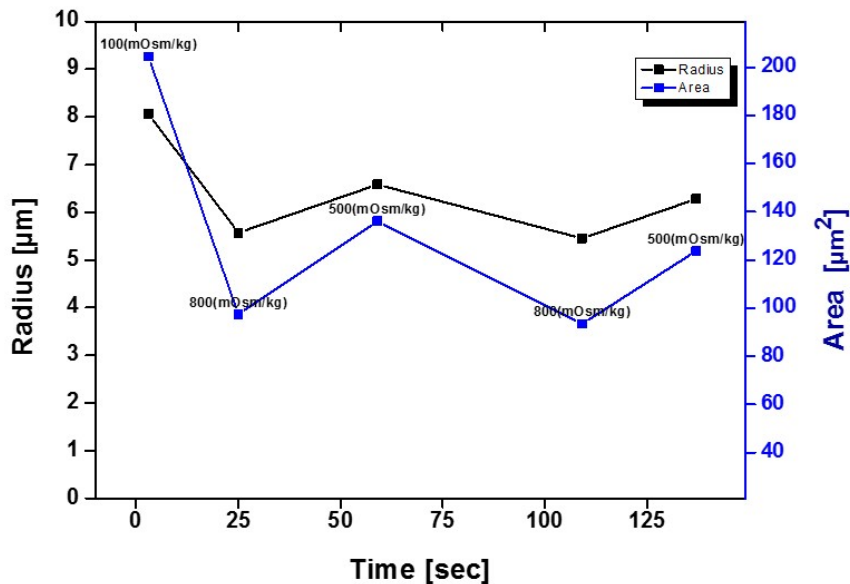


Figure 5.4.: Rapid exchange of side-solutions make a cell in the middle channel swell or shrink. Cross section area (blue) and radius of the cell (black) in the central channel of microfluidic chamber versus time. According to the solution running in the side channels, the cell will shrink or swell. Osmolarity of the side solutions in each step is mentioned.

Furthermore, Fig.5.5 shows transfected 3T3 cells in the central channel of such a micro-device when the side medium was changed from hypo to hapertonic.

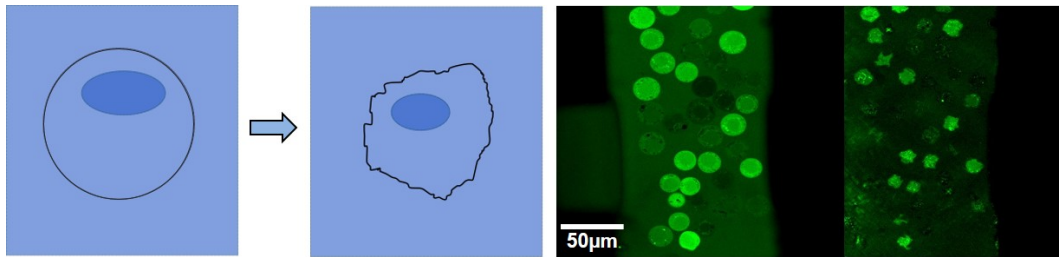


Figure 5.5.: Cell volume shrinkage from hypo- to hyper-tonic medium. Because of semipermeable membrane eukaryotic cell will absorb water in hypotonic medium and lose water in hypertonic one. Schematic volume change from hypo to hypertonic medium shown in left hand side. On right GFP labeled 3T3 cell in microfluidic chamber under this condition are demonstrated.

– Concentration gradient and holding with optical trap

The next step is holding the suspended cells with optical tweezers using trapping particles. Fig.5.6 show the experimental configuration of a cell suspended with the dual optical trap.

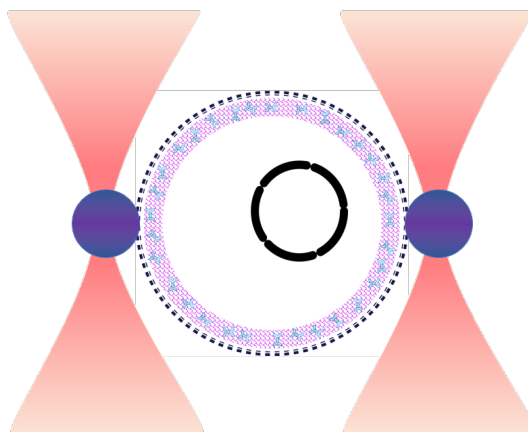


Figure 5.6.: Suspended cell hold with two trapped micro-particles. Schematic of dual optical trap holding a rounded cell to probe the mechanical properties.

A big osmotic shock which causes sudden dramatic diameter (and volume) changes of the cell. Technically, such compression/expansion is problematic because it makes the particles jumping out of the traps.

As both traps were kept stationary (focused on the initial spot) during the osmotic and volume changes, care has to be taken to make smooth and slow tonicity changes. Therefore, additive sugar concentration ΔC , needed for $< 1\mu m$ diameter drop is estimated according to Van't Hoff 's law:

$$\Delta\Pi = R\theta\Delta C \quad (5.5)$$

where R , θ , are gas constant and temperature and ΔC is the concentration gradient. Based on Laplace law:

$$\Delta\Pi = \frac{2T\Delta R_c}{R_c} \quad (5.6)$$

if we assume the tension T , will remain constant for such small change, then corresponding ΔR_c can be calculated. To make sure that the coupled system of trapping particles and cell can bare the volume shrinkage without jumping out while sugar (sorbitol) is increasing, <100 mM sorbitol was added in each single step. Experimentally, we gave the cell ~ 20 min to adapt to each step/level of tonicity.

5.3 Results

5.3.1 Single step osmotic compression

Fig.5.7 shows the force fluctuations and stiffness of L-1210 cells in controlled isotonic medium and hypertonic sugar medium. The cells were gone through a single step osmotic change from their isotonic culture medium to 500 mM D-Sorbitol hypertonic media.

In parallel, Fig.5.2 shows the volume shrinkage of a 3T3 cell in exposed to the same osmotic changes that results in $\frac{V}{V_0} \sim 70\%$.

As a result, averaging between 15 to 20 cells held with optical traps, revealed that in an extreme hypertonic medium cells got smaller and at the same time stiffer. Stiffness of the cells was calculated based on the linear spring model explained in the 2nd chapter. In average, cells became stiffer ($\frac{k_{Hyper}}{k_{control}} \sim 150\%$) and corresponding averaged force fluctuations dropped about 2 folds. Force fluctuation measurements with 2-particle MR are discussed in 2.2.1

Considering these results and volume measurements showed in Fig.5.2, we hypothesized that stiffening is the result of water efflux, that results in

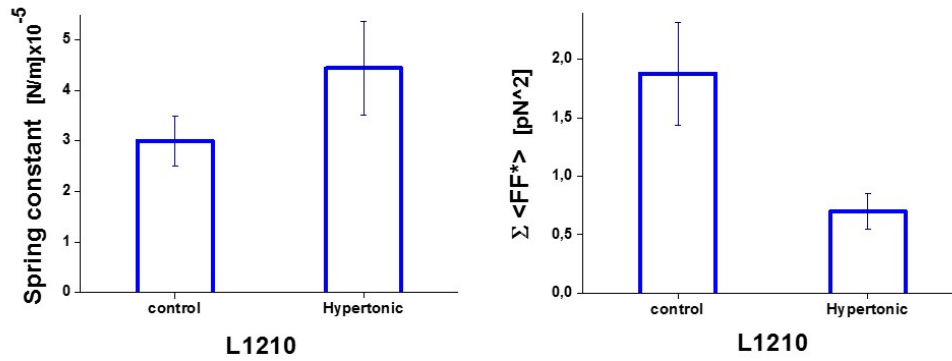


Figure 5.7.: Stiffness and force fluctuations of L1210 cell in isotonic compared with hypertonic medium. Under single step hypertonic (500mM D-Sorbitol) compression made L1210 cells became stiffer and the force fluctuations dropped.

crowding of the intracellular space. We call it intracellular crowding due to osmotic compression (see fig. 5.15). In fact, transfection and labeling, hence volume measurements of 3T3 cells using a fluorescence microscopy were easier than L-1210. Here it is mentioned only as a proof of shrinkage without insisting on the percentage.

Technically, a stiff cell under the constant trap stiffness, transmits lower force to the trapping particles which we measure (see eq.2.23). Therefore, the drop in $\Sigma \langle FF^* \rangle$ is partially due to the cell stiffening.

However, intracellular changes can play a role in the force drop. As it was explained before, myosin motors pull on actin filaments and generate contractile force on the cell's cortical network. The more active the myosins, the higher force generation. The drop of force as a result of hyper osmotic pressure therefore, indicates the lower motor activity on cell cortex. Meaning, the actin network is so compressed such that myosin can not make contraction as before.

Other possible explanation is the following: by osmotic shock the cell undergoes a sudden dramatic compression, that does not let myosins follow actin filaments any longer. It can be either due to the filaments buckling and network deformation (hypothetically occurring during compression

shock) or the slow velocity of motors compared to the global compression of the network. Sliding velocity of myosin on actin filament in cells, a few 100 nm/sec is reported [85]. It is apparently too slow to follow the cortical-actin-network which is compressed by a few $\mu m/s$. However, these statements need more investigations.

5.3.2 Multi step gradual osmotic compression

Our novel technique to study a single cell mechanically stimulated by changing the osmotic pressure, was using specific microfluidic chamber with a hydrogel membrane integrated between neighboring channels. In section 3.4.3, it has been explained how to control molecular diffusion and make a localized concentration gradient (see Fig.3.20, 3.21). Likewise different concentrations of D-Sorbitol in culture medium of cells were prepared, from very mild 6 and 12 mM up to 250 mM. We started with active microrheology using dual optical trap to measure the cell stiffness and increased the sorbitol concentration step by step. We saved about 20 min for each step/ level of tonicity.

Assuming that cell deforms symmetrically, we used the cross section area to calculate the volume of cell sphere/ellipsoid, shown in Fig.5.10. Based on Ponder's relationship, $V = R \frac{\Pi_{iso}}{\Pi} + (1 - R)$, (where R is the Ponder's value) normalized cell volume expected to be linearly related to the reciprocal of the extracellular osmolality [86],[87].

We used 2D images to estimate the volume of a single cell (from single snap shots). Volume and area of recovered cell, after getting back to isotonic medium (blue points), is close to initial values before osmotic compression.

Position of both traps are kept invariant, so the cell was confined by two traps therefore by diffusion of sugar cell shrinkage happened in a direction perpendicular to the cell and the trapping particles coupling axis (Fig.5.8). The corresponding cross section area for each step is shown in Fig.5.9. After running active and passive microrheology a few times, to get the average stiffness and force fluctuations of an individual cell, the solution

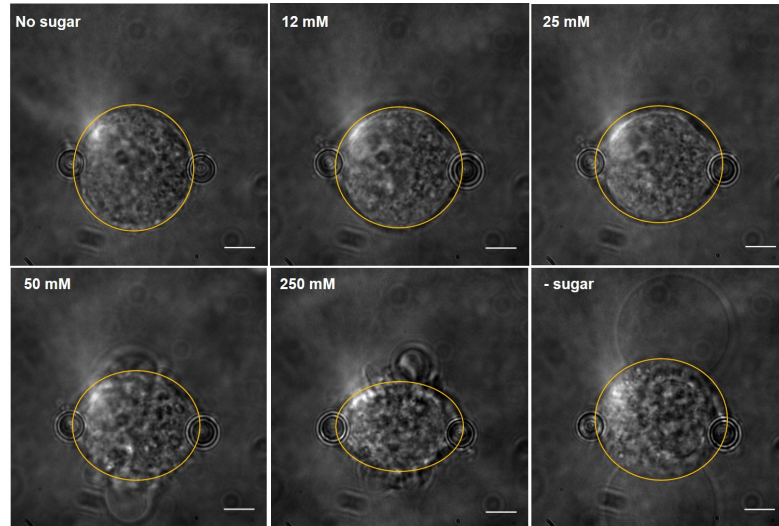


Figure 5.8.: Gradual sugar diffusion changed the cell size while holding with trapping particles. Cross section of representative 3T3 cell held with fibronectin coated particles is changing by step-wise adding sugar. Changing osmolarity from mild to harsh is applied. Images shown here (top view) have been used to calculate cross section area. Last step of experiment was washing sugar out, indicated with '- sugar'. Scale bar is $5\mu\text{m}$.

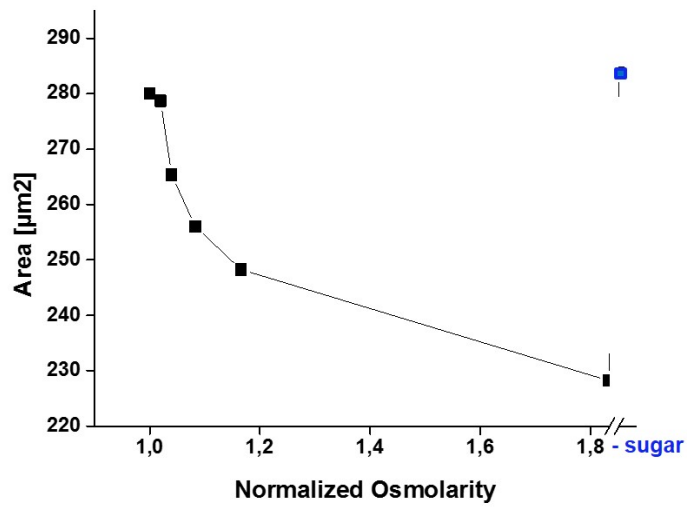


Figure 5.9.: Cross section area of 3T3 cell exposed to gradual sugar diffusion. Cross section of a representative 3T3 cell suspended in microfluidic chamber and held with trapping particles is changing by step-wise adding sugar. Osmolarity was changed from mild to harsh is applied. Top view images have been used to calculate cross section areas. The last step of experiment was washing sugar out, indicated with '- sugar' in blue.

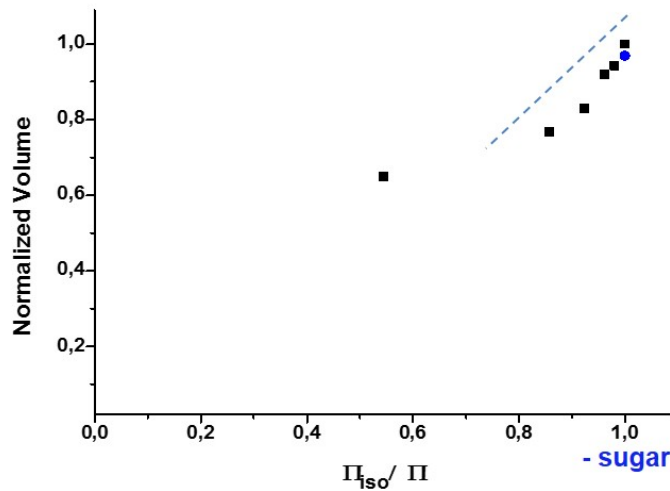


Figure 5.10.: Dependence of relative cell volume on inverse osmotic stress. Hyperosmotic stress decreased the cell volume. Finally, after sugar washed out, hypotonic stress caused cell swelling, indicated with '- sugar' blue circle. Dashed line guides to Ponder's relationship between cell volume and external osmolality.

in side channel is changed, starting from the lowest sugar concentration, 6 mM, running for about 20 min while we kept measuring every 5 min. Then the next solution 12 mM had to be infused and so on (Fig.5.11).

The experiment consisted of 6 successive steps from 6 mM up to 250 mM and at the end normal culture medium without sugar was applied (in order to see the cell recovery). Practically, using our micro-chamber we were able to study hyper and hypotonic changes and then get back to the isotonic condition.

The final calculated values in each step have been averaged, so the error bars in Fig.5.11 to 5.14 denote the variation from average within 20 min.

In the following, we split the results into three parts: 1st from normal to very mild tonicity (the first three steps), 2nd intermediate hypertonicity and 3rd from hypertonic back to isotonic (250 to 0 mM sugar). Fig.5.12 shows the first three steps.

Interestingly, we saw both softening and stiffening of suspended 3T3

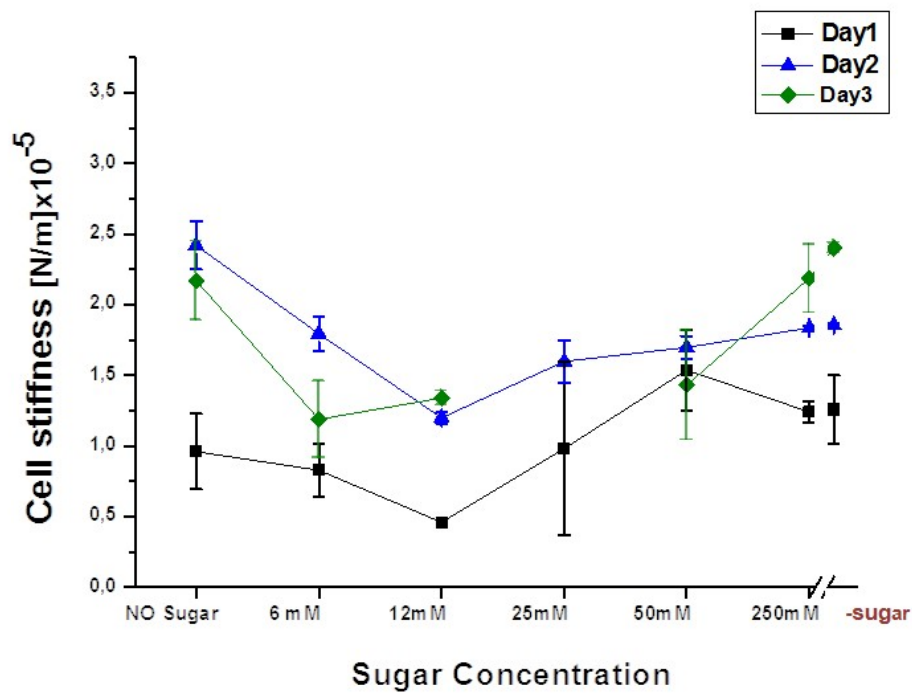


Figure 5.11.: Cell stiffness changes by osmotic pressure corresponding to the sugar level. Sugar concentration diffusing through HMM windows was increased step-wise from 6 and 12 up to 250 mM. At the final step sugar was washed out (shown after break in the horizontal axis). Initial drop in cell stiffness is followed by stiffening in higher concentration. The error bars represent variation from the average in 20 min.

cells when we applied hypertonic solution. In very mild sugar medium ~10 mM, cells became softer, however increasing sugar to 25 and 50 mM made them stiffer. Thus there should be a threshold for this transition. One can see these in Fig.5.12, 5.13, cell stiffness in a given sugar concentration is k_i , and in the initial 'No-sugar' medium is k_0 , with pink-guide lines depicting $k_i/k_0=1$.

For the first steps, when cells exposed to very mild hypertonicity got softer, there is barely literature evidence. However, cell and viral capsule stiffening due to osmotic compression was reported already in [88] and [89].

Lastly, from hypertonic back to the isotonic condition, in spite of an obvious water absorption and volume expansion of the cell, we didn't see any significant difference of the stiffness. Fig.5.8 shows the representative

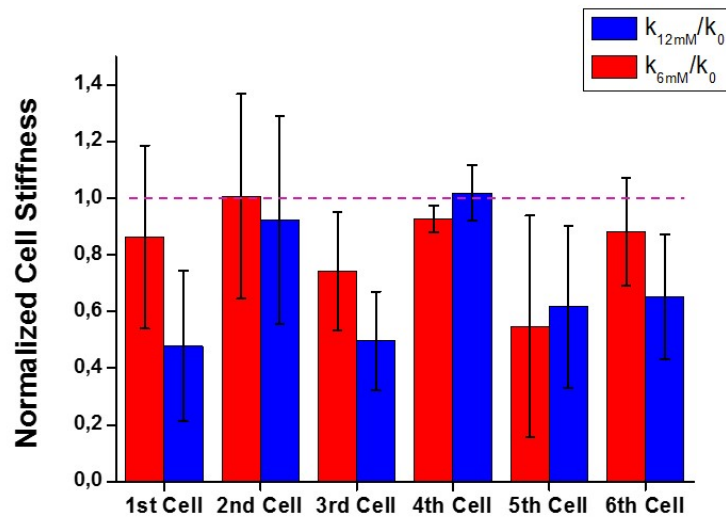


Figure 5.12.: Normalized cell stiffness changes in mild hypertonic medium. Very low sugar addition (6 , 12 mM D-Sorbitol) soften the cells. Cell stiffness in a given sugar concentration is k_i and in 'No-sugar' medium is k_0 . Error bars denote the variation of k_i/k_0 in 20 min periods.

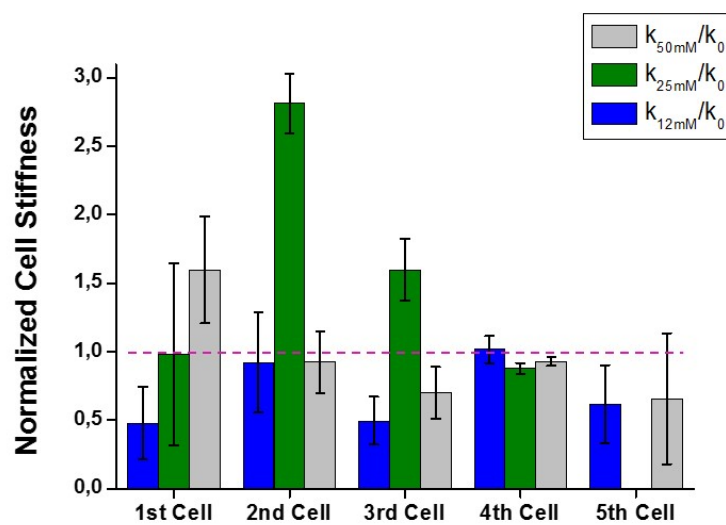


Figure 5.13.: Normalized cell stiffness changes in hypertonic medium. Increasing sugar concentration (25, 50 mM D-Sorbitol) starts stiffening the cells. Cell stiffness in a given sugar concentration is k_i and in 'No-sugar' medium is k_0 . Error bars denote the variation of k_i/k_0 in 20 min periods.

cell could roughly reach its initial size, cross section area, based on our observation.

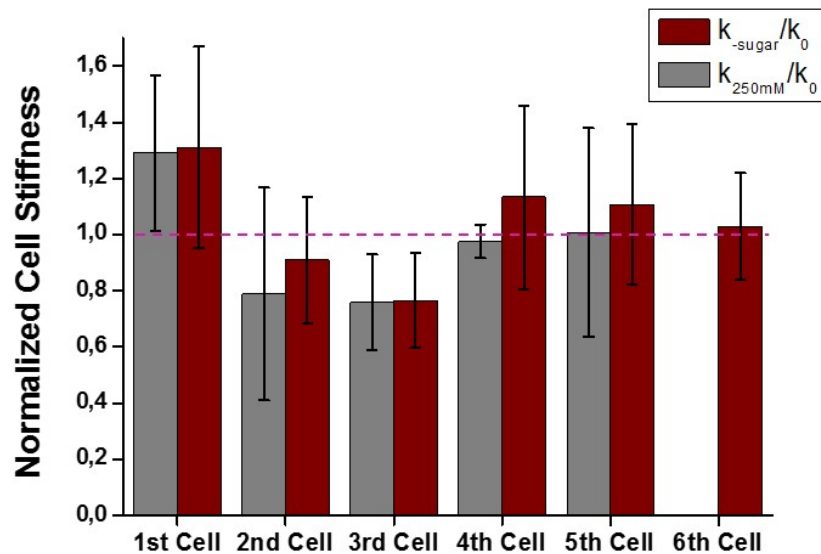


Figure 5.14.: Comparison of normalized cell stiffness in hypertonic sugary medium and in the absence of sugar. Cell was kept on hold for about 20 min in 250 mM D-Sorbitol and then 20 more min when sugar was washed out by running normal culture medium in side channels. Cell stiffness in 250 mM sugar is k_{250mM} , after sugar washed out k_{-sugar} , and in initial 'No-sugar' medium is k_0 . Error bars denote the variation of k_i/k_0 in 20 min periods.

In the last three graphs, large error bars are duo to the fact that, each of k_i is measured within a period of 20 min from the moment of sugar addition. Taken into account that the cell' volume compression and then adaptation happen within this period (see Fig.5.2), one can expect variation in cell stiffness. Assuming that k_0 is measured with $\pm 10\%$ error, and k_i with $\pm 20\%$ error in this time period, results in a final error of $> 22\%$ (see [90]).

5.4 Discussion

Both, the conventional method and the new technique result in: Cells in hypertonic solution (25-500 mM D-sorbitol) shrink and get stiffer. This finding is similar to the behavior of viral capsules studied earlier by (Ivanovska et al.2004) [88]. In accordance with the model for thin shells [91], the stiffness of cells K increases inversely with respect to the radial size R :

$$K \propto E \frac{h^2}{R}. \quad (5.7)$$

where E is elasticity and h is thickness of the capsule.

Moreover, (Zhou et al.2009) have observed stiffening as an universal behavior of osmotically compressed cells[89]. Despite the fact that filaments of compressed cells may buckle and weaken the network of the cell cortex, intracellular crowding is more dominant and thus results in an increased stiffness of the cells [92].

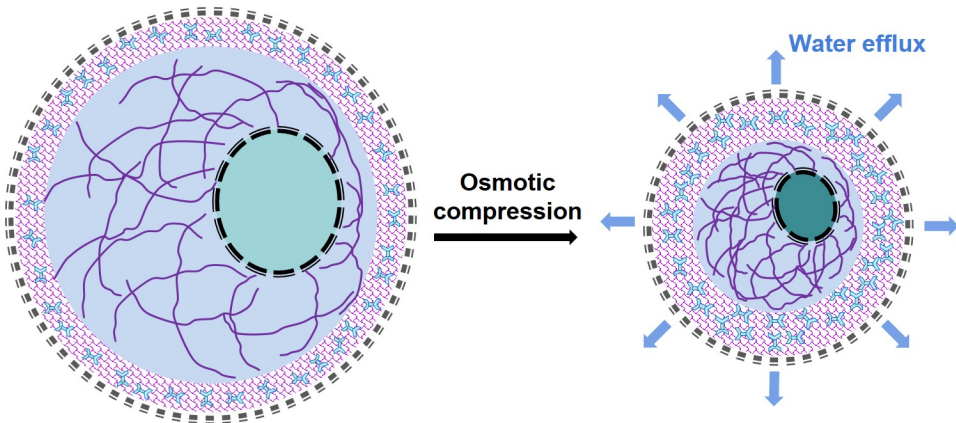


Figure 5.15.: Cell stiffness correlates with its volume. Schematic illustration of cell volume decrease through water efflux, due to osmotic compression and intracellular crowding. Underneath the plasma membrane, cortical acto-myosin network is surrounding interior cytoplasm with filaments and the cell nucleus.

Similarly, considering the single step hypertonicity driven cell mechanics, it seems reasonable to relate cell stiffening to intracellular crowding. Fig.5.15 illustrates the schematic drawing of this phenomenon. Assuming that during compression the cell conserves the density of its interior components, the cell volume will be reduced only by water efflux.

In addition, our novel approach of time-lapse- mechanical studies of single cells, allowed us to control the osmotic pressure, such that we could gradually impose osmolytes from very mild to harsh. Indeed, we successfully managed to expose individual cells to very mild sugar concentration (~ 10 mM) and simultaneously measure the stiffness. To our knowledge, this controlled back and forth play has not been reported in literature.

Interestingly, we observed a new behavior of cells in this mild range of osmolytes. Cells did not show any significant size change (shrinkage), but got softer. The initial softening of cells can be the result of the filament network weakening and possibly interpreted as an intermediate step in the phase transition to stiff cells.

A next step is to clearly identify the threshold of cell stiffening and to further characterize the intermediate state of initial cell softening. Yet, for this purpose, further statistics are required.

Lastly, when hypertonic sugar solution was washed out by the infusion of isotonic solution, despite an increase in cellular size (up to its initial volume) no significant change in cellular stiffness was observed.

Whereas, the stiffening of osmotically compressed cells is a result of intercellular crowding, 'recovered' cells might remain stiff due to the process of water absorption and pressure acting on the cortical network. In other words, water absorption pushes against the cell wall and stiffens the cortical network. Such explanation is consistent with (Stewart et al.2011), when they investigated the cell shape affected by osmotic pressure in conjunction with the actomyosin-cortex-contraction. For spherical cells, actomyosin contractility exerts an inward directed force which will be balanced by outward osmotic pressure. The higher the tension and pressure, the greater the cortex rigidity [2],[68]. This rigid cortex appeared in our last steps of experiment (250 mM hypertonic to isotonic media).

- Comparison with thin shell model

The thin shell model [91] can be used to explain volumetric and mechanical properties of spherical cells under osmotic compression. In the

following, the thin shell model is briefly introduced. Next, the results obtained by the described experiments is interpreted regarding theoretical predictions.

The cortical thickness h of a thin shell is less or equal than ten percent of its radius R ($h/R \leq 10\%$). For a homogeneous, thin, empty shell undergoing small deformation, the spring constant K depends on Young's modulus E , and its geometrical quantity (h/R):

$$K \propto E \frac{h^2}{R} \quad (5.8)$$

This is valid as long as the deformation amplitude is in the order of the shell thickness. For larger deformation amplitudes, as a result of in-plane compression and out-of-plane bending, non-linear buckling is predicted.

As mentioned earlier, the experimental probing of mechanical properties of nanometer bacteriophage shell has been shown by (Ivanovska et al.2004), is consistent with this model. It could confirm the linear elastic response of the viral shell for very small indentation amplitudes.

An extension of this model will be a water filled shell instead of the empty one. As water is an incompressible fluid, volume conservation during deformation comes into play.

Comparison between experiments on a ball, in both empty and water filled condition, revealed that the filling of the shell does not make any difference for deformation up to 20% of the radius compared with the empty ball [93]. In fact, the effect of the fluid will become significant for larger deformations. Although, the smaller thin shell undergoing small deformation appears stiffer, this behavior will change for large deformations.

Empty thin shell under isotropic external pressure, may buckle. Critical pressure for buckling of such a spherical shell P_c will be

$$P_c = \frac{2E}{\sqrt{3(1-\sigma^2)}} \frac{h^2}{R^2} \quad (5.9)$$

where σ is the Poisson ratio. When we substitute corresponding quan-

tities for the cell from [1], P_c turns out to be 300-500 of Pa (<1 kPa), which according to [79],[92], has the same order of magnitude like cortical actomyosin stress of cell itself. Indeed actomyosin contraction applies inward pressure on the cell cytoskeleton [68]. Nevertheless, biological cells, are not only filled with fluid, but also the fluid is under increased osmotic pressure, so called turgor pressure, that pushes against the cortex. So, actomyosin contractile tension is balanced by an outward-directed, intracellular osmotic pressure [93],[68].

Calculations using Laplace law, depict that ~ 30 mM concentration gradient in the cell medium roughly causes an increased pressure up to a few kPa, the same order of magnitude with cortical stress.

Also, (Guilak et al.2002) experimentally studied of physical properties of articular chondrocytes. The cell volume in both ± 150 mOsm/kg conditions, got clearly changed corresponding to the extracellular osmolytes. This study indicated that hypotonic stress (-150 mOsm/kg) significantly influence viscoelastic properties, although, the elastic moduli of cells remained unchanged under hyperosmotic stress by adding (+150 mOsm/kg) osmolytes to the isotonic medium [86].

In fact, most of osmotic pressure studies on cells have been done for high pressure in the MPa regime in order to observe an obvious affect on the cell volume, where the influence of the cell cortex can be neglected. However, in the regime of very mild osmotic change, our results shows the indication of cortex contribution in the cellular stiffness.

This thesis was determined to open new experimental possibilities to study cell mechanics. Main focus was on mechanical properties under the extracellular osmotic changes. For this reason, we presented the preliminary but promising results taken with our new methodology. However, further experiments and statistical analysis is required to be able to generalize the cells response to the osmotic pressure. We hope our new methodology opens a new window to address open questions and helps to come up with a viscoelastic model for the suspended cells.

Conclusions

Living cells possess structural and physical properties that enable them to survive in physiological environments inside or outside of the body. Various stimulations can make them react in order to save their physical integrity as well as biological functions[10]. It has been proven that in response to mechanical and biochemical stimulation, mechanical properties and morphology of cells are changing [6][7],[87].

The use of a dual optical trap to simultaneously probe force generation and elastic responses of living cells has been established by (Mizuno et al.2008, and 2009). Combining active and passive microrheology techniques together with laser interferometry made it possible to quantify non-equilibrium fluctuations and the active force generated by suspended cells. Using this technique (Schlosser et al.2014) investigated the effect of intracellular structure perturbation. However the heterogeneity in cell populations (cell to cell variation), was noticeable and therefore made it difficult to interpret the real impact of some drugs.

This was one of the motivations to find a way to study single cells. Moreover osmotic pressure is known to be the most dominant parameter in volume regulation and hence the mechanics of eukaryotic cells. We were therefore, interested to explore mechanical properties of cells under variable osmotic conditions.

To this end, we adapted a novel microfluidic device that successfully fulfilled both of expectations [50]. We printed hydrogel micro-windows between neighboring flow channels to be able to rapidly change solution conditions for suspended cells. During this exchange we probed their mechanical response with dual optical traps. In fact, we managed to expose the cells to biochemical inhibitors and different osmolytes without direct fluid flow, and simultaneously investigated the time-dependent response of individual cells.

The device configuration and technique to produce hydrogel membrane micro-windows (HMM), was introduced by (Paustian et al.2013 and 2015). The novelty of the work performed in this thesis, was to fabricate the hydrogel membranes with desired sizes and forms, using a simple method obtained with one of a common instruments: UV photo-polymerization using a scanning confocal microscope. We photopolymerized PEG-Da inside our closed microchannels using a UV diode laser. After multiple biochemical- and optical-optimization steps, the whole device with the hydrogel membrane, could be constructed to be bio-compatible with desired optical characteristics, quite robust without any leakage or swelling, reusable for multiple uses and very low-cost compare to commercial micro-chambers. Indeed it is a potential microfluidic device for rapid dialysis and swapping of solvent without any hydrodynamic flow, as well as providing convection-free localized concentration gradients.

As the first application we investigated the effect of myosin inhibition and osmotic pressure by controlling concentration gradients of sugar (sorbitol). By time-lapse tracking of single cells, volume and mechanical changes were recorded simultaneously. According to our result, motor inhibition which is reported to bring down the cortical tension of cells [7], did not

cause clear differences in the stiffness of single cells. However force fluctuations showed a clearly decreasing trend. Our single-cell results may explain the contradiction existing in literatures [15] and [8] about stiffness of myosin inhibited cells as both had been studied in bulk.

Gradual increasing hypertonicity of the cell medium in our microfluidic chamber, made 3T3 fibroblasts softer at low sugar levels, but with increasing hypertonicity they became stiffer. This stiffening caused by osmotic compression was confirmed by our result from single-step osmotic change experiments in macro-chamber, and also agrees with previous works [88],[89]. The softening behavior seems interesting for further investigations.

In summary, we demonstrate a new methodology for studying single cells suspended in a microfluidic device. This provides a complementary techniques to common optical trapping microrheology. The time dependent mechanical response of single cells under biochemical stimulation and controlled osmotic pressure was measured in this work, looks promising for further investigation. We hope our approach opens a new window to address existing open questions and helps to model viscoelastic properties of living cells.

A

Appendix

A.1 Biochemical protocols

In this appendix we present simple protocols used for polystyrene beads and glass coverslips.

A.1.1 Coating of beads

a) Fibronectin coating

- wash 1 ml (50mg/ml) carboxylated beads 2x in 10 ml Milli-Q water.
- after second wash resuspend pellet in 10 ml PBS and transfer it to a 1.5 ml eppendorf tube. Keep pipetting till the beads are very well suspended.
- add 100 mg EDC (N-Ethyl-N'-(3-dimethylaminopropyl)carbodiimide hydrochloride), contentiously stir then leave it for 15 min at room temperature.

- wash 2x with distilled water, then resuspend in 5 ml PBS.
- add the calculated amount of fibronectin (saturation at mg/ml, 240 μ l for 4 μ m beads) and leave them to stir for 2-4 hours at room temperature.
- Meanwhile make quenching solution (0.15 g glycine/50 ml Milli-Q + 1 ml of 10% BSA), and storage buffer (0.1% BSA in PBS).
- After fibronectin reaction is over, wash and resuspend beads in 4 ml of quenching solution. Let them mix gently for 30 minutes.
- wash and resuspend beads in storage buffer to desired storage concentration.
- store at 4°C until used.

b) Poly-L- Lysine coating

This protocol is the optimized version of [36]. Saturation concentration for surface coating using PLL is 1 mL/25 cm². Optimal concentration has to be determined for each application.

- wash 1 ml (50mg/ml) carboxylated 4 μ m beads 2x with Milli-Q water.
- after second wash resuspend pellet in final concentration of 1 ml of Poly-L-Lysine (PLL) solution (0.01% concentration, P4707, sigma).
- Leave them for 20-30 min in room temperature while stirring the mixture.
- spin it down (8000 rpm), wash and resuspend with distilled water.
- store in distilled water at 4°C until used.

PLL coating might not working properly when it gets old. We used to have fresh coated beads every few weeks or after a month.

A.1.2 Glass cover-slip coating

One way of surface treatment for making a hydrophilic glass is using dimethyldichlorosilane (DDS) with the following instruction.

Before coating, first cover slips have to be cleaned using KOH:

- put cover-slips in a teflon holder in a glass box.
- add 6-8 g of KOH pellets and dissolve it in Milli-Q water.
- pour 70% Ethanol into the glass box so that cover-slips are fully covered.
- sonicate for 5 min.
- discard KOH solution, wash and sonicate cover-slips 2x with Milli-Q.

After cleaning, it's time to coat cover-slips with DDS:

- put tiny clean glass beads in a glass petri dish, then transfer KOH cleaned cover-slips to that.
- pour DDS solution (5% DDS in Heptane) on cover-slips, fill the petri dish and incubate them for 20 min.
- put heptane in a beaker and dip cover-slips one by one in there.
- again put cover-slips in teflon holder, put all in the glass box. Add Milli-Q and sonicate for 5 min.
- take them out. Pour a water droplet and check coverslips' hydrophobicity.
- store them in a clean petri dish, sealed until usage.

A.1.3 Conventional sample preparation for two-particle microrheology

Before chamber and biochemical preparation, first check the trap set up alignment by beam profiles, mark their position and vary light intensity using motor driven $\lambda/2$. One can even measure the intensity in both direct and indirect path, with a beam profiler to set the desired intensity led to the sample.

- Make a flow chamber using glass slide, double-stick tape and DDS coted cover-slip.
- Dissolve 1% pluronic in Milli-Q water solution(P-2443, Sigma). After careful mixing, infuse it into the chamber and leave it for 3-5 min.
- Dilute pluronic solution 10x into CO2 independent medium and infuse it into the chamber.
- Take $\sim 900\mu M$ CO2 independent cell medium, add 3-5 μl coated polystyrene beads.
- Sonicate bead solution for 5 min.
- Add 50-100 μl cell solution and again 50 μl pluronic solution to it.
- Cell solution is ready now to infuse into the chamber.

According to the channel geometry(width and height) and duration of the measurement it may need to optimize concentrations.

B

Appendix

B.1 Optics alignment procedure

B.1.1 AOD adjustment

Before driving AODs and driver pay a careful attention to electric impedance and accepted RF power to avoid any damage. Fig.B.1 shows the back and front view of DTSXY 2-axis deflector.

a) First adjustment the Y deflector:

- center the incident polarized beam in the aperture, close to optical auto-collimation referred to the 1st optical face of the Y deflector(check the direction of polarization according to device manual/test-sheet).
- connect the Y deflector.
- drive the deflector using AA driver.
- check the efficiency with a photo-detector.

- improve the AO efficiency using 3. and 4. screws for fine angular adjustment, or 6., 7. and 8. to slightly rotate the XY plate.

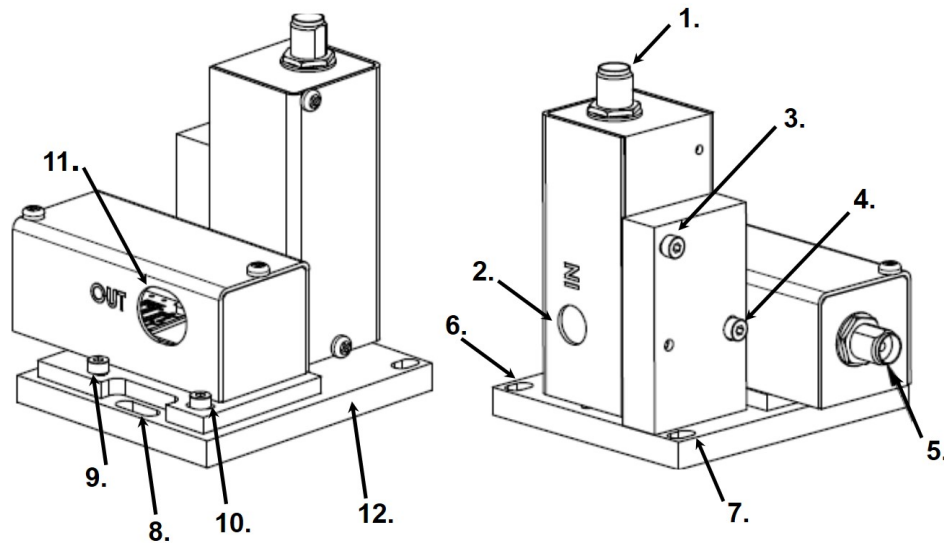


Figure B.1.: AOD back and front view. AAOptoelectronic 2-axis AO deflectors IN and OUT aperture.RF connector (1), IN and OUT apertures (2.,11.), adjustment screws(3.,4.,9.,10.) and fixation holes(6.,7., 8.) are demonstrated, all mounted on a baseplate (12.).

b) Adjustment of the X deflector:

- Y deflector is still connected, connect the X deflector.
- drive the Y deflector with MOD IN=Vmax.
- drive the X deflector also with MOD IN=Vmax.
- drive the XY frequency with FREQ= central frequency.
- check the efficiency with a photo-detector and the collinearity of incident and diffracted beams.
- do final mechanical adjustment using a3 and a4 screws for fine angular rotation.

Note has to be taken, adjustment screws(3.,4.,9.,10.) were preadjusted in factory. Therefore we tried not to touch them but instead rotate the baseplate in 3D using 4 micro-screw mounting base.

C

Appendix

C.1 Soft lithography protocols.

Based on general SU-8 3000 data sheet, two protocols for different thickness of photoresist on 2 inch wafer both using SU-8 3050, are presented [94].

C.1.1 Procedure for $\sim 40\text{-}50\ \mu\text{m}$ photoresist using SU-8 3050.

- Clean Si wafer with Acetone in ultrasonic bath for 10 min.
- Rinse with isopropanol (IPA).
- Dry with N₂.
- Dry on a hot plate at 200°C for 10 min.
- Pour SU-8 3050 on wafer 1ml per inch.
- Spin coating in two steps:
 - 500 rpm, 100 rpm/sec acceleration, 10 sec

- 3500 rpm, 500rpm/sec acceleration, 30 sec
- Soft back on a hot plate at 90°C for 100 min (gradual increase from 65 to 90°C).
- Let it cool down gradually by switching down the hot plate.
- Align the mask and fix the wafer by vacuum.
- Start illumination for soft lithography with 365nm UV exposure for 18 sec.
- Post back in two steps:
 - on hot plate with 65°C for 1 min
 - on a plate with 95°C for 15 min
- Cool down slowly to room temperature, 15-20 min.
- Develop SU-8 while shaking for 5 min, 3 times.
- Stop developing by rinsing with IPA for 30 sec.
- Dry with N₂.
- Hard back at 150°C for 20-30 min.

C.1.2 Procedure for $\sim 70 \mu\text{m}$ photoresist using SU-8 3050.

- Clean Si wafer with Acetone in ultrasonic bath for 10 min.
- Rinse with isopropanol (IPA).
- Dry with N₂.
- Dry on a hot plate at 200°C for 10 min.
- Pour SU-8 3050 on wafer 1ml per inch.
- Spin coating in two steps:
 - 500 rpm, 100 rpm/sec acceleration, 5 sec
 - 2500 rpm, 300rpm/sec acceleration, 30 sec

- Soft back on a hot plate at 90°C for 45 min (gradual increase).
- Let it cool down gradually by switching down the hot plate.
- Align the mask and fix the wafer by vacuum.
- Start illumination for soft lithography with 365nm UV exposure for 20 sec.
- Post back in two steps:
 - on hot plate with 65°C for 1 min
 - on a plate with 95°C for 15 min
- Cool down slowly to room temperature, 15-20 min.
- Develop SU-8 while shaking for 8 min, 3 times.
- Stop developing by rinsing with IPA for 30 sec.
- Dry with N₂.
- Hard back at 200°C for 10-15 min.

D

Appendix

D.1 Microfluidic device fabrication

Using soft lithography of SU-8 photo-resist, as described, a desired pattern with a proper height is printed on a silicon wafer that called mater mold. Mix the PDMS monomer (base) and its curing agent ($\sim 1/10$ of PDMS). Pour it on the master mold and let it back for at least 4 h at 80 degree. After baking carefully peel off the PDMS layer to get a negative PDMS stamp. An illustrative schematic of the device fabrication is shown in Fig.. Here the detail is described.

D.1.1 Microfluidic NOA-81 sticker

In order to fabricate a microfluidic sticker, first prepare the following tools and materials:

NOA-81 adhesive resin, the PDMS stamp, a flat PDMS mold, cleaned coverslips, a benchtop UV lamp (365 nm), a biopsy puncher (0.5 mm), a 5-min Epoxy resin (2-Part), a vacuum desiccator, 5% DDS in heptane solution, tiny acrylic rings and stiff tubings (matched size) for inlet/outlets and a

sharp tweezer.

- Pour a drop of the NOA-81 on the PDMS stamp.
- Carefully suck the air bubbles with a syringe or poke them.
- Sandwich the NOA drop on the PDMS stamp with a flat PDMS mold.
- Expose the sandwich to 365 nm UV light for 2-4 min (NOA has to get stiff).
- Peel off the PDMS stamp.
- Drill inlet/outlet holes into the cured NOA using a biopsy puncher (0.5 mm).
- Replace the PDMS stamp with a cleaned coverslip.
- Expose NOA-on-coverslip to the UV light for 2-4 min.
- Peel off the flat PDMS layer.
- Dip the acrylic rings in NOA and fix them carefully on the inlet/outlet positions using a tweezer.
- Expose the rings-on-coverslip to UV light for 3 more min in order to pre-fix them.
- Insert the tubings into the inlet/outlet rings. Using a pipette tip fully cover the tubing with the 5-min epoxy resin.
- Let epoxy dry to tightly seal the tubing. As the resin layer is thick it may need a few hours to completely dry out.

Now the sticker is ready and it is the time to make it hydrophobic:

- Pour 100 μ l of the DDS solution into a beaker. On top of the beaker, put the sticker-on-coverslip faced down that Silane vapor can enter the channels. Close the beaker fully with a self-made lead.

- Put the beaker in a vacuum desiccator for 10 min. By sucking the air DDS evaporates and Silane vapor goes through the channels.
- Take out the beaker and soak the vapor inside with a syringe connected to the central channel.
- The hydrophobic device can be stored in a clean box away from dust for a few weeks.

D.1.2 Hydrogel membrane fabrication

- Prepare a mixed solution of PEG-DA monomer and a proper photoinitiator with desired ratio (e.g. 95% and 5% respectively).
- Put the empty chamber on the microscope stage and focus a 10x objective on the middle height of the channels. Using the reflection-profile of light is helpful.
- Fill the connected channels with the mixed solution of PEG-DA.
- Set the scanning confocal microscope (Leica TCSS P5) for 1024x1024 image format, 12x zoom-in, 1000 Hz scanning speed, bi-directional scanning, 1 Airy (AU) pinhole.
- Select a rectangular ROI and drag a rectangle that covers the opening of the channel windows.
- Expose the ROI for 1-2 sec to 95% intensity of the 405 nm diode laser to photo-polymerize two hydrogel membrane windows.
- Wash out the channels with IPA to remove uncured solution inside. Using the compressed air is helpful to fill the channels carefully.
- After IPA, wash the channels continuously for at least 20 more min with de-ionized filtered water.
- Fill the connected channels with the mixed solution of PEG-DA monomer.

The chamber with HMM is ready to use. It can be stored for 1 or 2 days. Longer storage (away from dust) is possible but one has to be very careful about the contamination and hydrophobicity.

Bibliography

- [1] Hongyuan Jiang and Sean X. Sun. Cellular pressure and volume regulation and implications for cell mechanics. *Biophysical journal*, 105(3):609–619, 2013. (cited on page 1, 2, 3, 4, 94, and 112)
- [2] Martin P. Stewart, Yusuke Toyoda, Anthony A. Hyman, and Daniel J. Muller. Force probing cell shape changes to molecular resolution. *Trends in biochemical sciences*, 36(8):444–450, 2011. (cited on page 1, 67, 77, and 110)
- [3] Maddaly Ravi, V. Paramesh, S. R. Kaviya, E. Anuradha, and F. D. Paul Solomon. 3D cell culture systems: advantages and applications. *Journal of cellular physiology*, 230(1):16–26, 2015. (cited on page 2 and 66)
- [4] Romain Levayer and Thomas Lecuit. Biomechanical regulation of contractility: spatial control and dynamics. *Trends in cell biology*, 22(2):61–81, 2012. (cited on page 2)
- [5] Kazuaki Nagayama and Takeo Matsumoto. Contribution of actin filaments and microtubules to quasi-in situ tensile properties and internal force balance of cultured smooth muscle cells on a substrate. *American journal of physiology. Cell physiology*, 295(6):C1569–78, 2008. (cited on page 2)
- [6] Guillaume Salbreux, Guillaume Charras, and Ewa Paluch. Actin cortex mechanics and cellular morphogenesis. *Trends in cell biology*, 22(10):536–545, 2012. (cited on page 2, 68, 69, and 115)
- [7] Jean-Yves Tinevez, Ulrike Schulze, Guillaume Salbreux, Julia Roensch, Jean-Francois Joanny, and Ewa Paluch. Role of cortical tension in bleb

- growth. *Proceedings of the National Academy of Sciences of the United States of America*, 106(44):18581–18586, 2009. (cited on page 2, 76, 95, 96, 115, and 116)
- [8] Chii J. Chan, Andrew E. Ekpenyong, Stefan Golfier, Wenhong Li, Kevin J. Chalut, Oliver Otto, Jens Elgeti, Jochen Guck, and Franziska Lautenschläger. Myosin II Activity Softens Cells in Suspension. *Biophysical journal*, 108(8):1856–1869, 2015. (cited on page 2, 35, 91, and 117)
- [9] Priyamvada Chugh, Andrew G. Clark, Matthew B. Smith, Davide A. D. Cassani, Kai Dierkes, Anan Ragab, Philippe P. Roux, Guillaume Charras, Guillaume Salbreux, and Ewa K. Paluch. Actin cortex architecture regulates cell surface tension. *Nature cell biology*, 19(6):689–697, 2017. (cited on page 2)
- [10] C. T. Lim, E. H. Zhou, and S. T. Quek. Mechanical models for living cells—a review. *Journal of biomechanics*, 39(2):195–216, 2006. (cited on page 2, 4, 5, 71, and 115)
- [11] José L. Maravillas-Montero and Leopoldo Santos-Argumedo. The myosin family: unconventional roles of actin-dependent molecular motors in immune cells. *Journal of leukocyte biology*, 91(1):35–46, 2012. (cited on page 3)
- [12] Marita L. Rodriguez, Patrick J. McGarry, and Nathan J. Sniadecki. Review on cell mechanics: experimental and modeling approaches. *Applied Mechanics Reviews*, 65(6):60801, 2013. (cited on page 4 and 71)
- [13] G. Bao and S. Suresh. Cell and molecular mechanics of biological materials. *Nat Mater*, 2(11):715–725, 2003. (cited on page 4 and 71)
- [14] Alexander X. Cartagena-Rivera, Jeremy S. Logue, Clare M. Waterman, and Richard S. Chadwick. Actomyosin Cortical Mechanical Properties in Nonadherent Cells Determined by Atomic Force Microscopy. *Biophysical journal*, 110(11):2528–2539, 2016. (cited on page 5, 70, and 72)
- [15] Florian Schlosser, Florian Rehfeldt, and Christoph F. Schmidt. Force fluctuations in three-dimensional suspended fibroblasts. *Philosophical transactions of the Royal Society of London. Series B, Biological sciences*, 370(1661):20140028, 2015. (cited on page 5, 45, 48, 74, 78, and 117)

- [16] A. Ashkin, J. M. Dziedzic, J. E. Bjorkholm, and Steven Chu. Observation of a single-beam gradient force optical trap for dielectric particles. *Optics Letters*, 11(5):288, 1986. (cited on page 7)
- [17] A. Ashkin. Forces of a single-beam gradient laser trap on a dielectric sphere in the ray optics regime. *Biophysical journal*, 61(2):569–582, 1992. (cited on page 7)
- [18] S. Karel. Biological Applications of Optical Forces. *Annual Review of Biophysics and Biomolecular Structure*, 23(1):247–285, 1994. (cited on page 7)
- [19] Joost van Mameren. Single molecule mechanics of biopolymers: an optical tweezers study. 2002. (cited on page 8, 9, 11, 12, and 16)
- [20] Florian Schlosser. *Mechanics of suspended cells probed by dual optical traps in a confocal microscope*. PhD thesis. (cited on page 8, 23, and 25)
- [21] Frederick Gittes and Christoph F. Schmidt. Interference model for back-focal-plane displacement detection in optical tweezers. *Optics Letters*, 23(1):7, 1998. (cited on page 10 and 56)
- [22] Frederick Gittes and C. F. Schmidt. Thermal noise limitations on micromechanical experiments. *European Biophysics Journal*, 27(1):75–81, 1998. (cited on page 12)
- [23] Frederick Gittes and Christoph F. Schmidt. Interference model for back-focal-plane displacement detection in optical tweezers. *Optics Letters*, 23(1):7, 1998. (cited on page 14)
- [24] André Düselder. *Single-molecule measurements of Kinesin motor proteins*. PhD thesis, Georg-August-Universität, Göttingen, 2014. (cited on page 14 and 16)
- [25] Michael Rubinstein and Ralph H. Colby. *Polymer physics*. Oxford University Press, Oxford and New York, 2003. (cited on page 20)
- [26] D. Mizuno, D. A. Head, F. C. MacKintosh, and C. F. Schmidt. Active and Passive Microrheology in Equilibrium and Nonequilibrium Systems. *Macromolecules*, 41(19):7194–7202, 2008. (cited on page 20 and 21)

- [27] Pietro Cicuti and Athene M. Donald. Microrheology: A review of the method and applications. *Soft Matter*, 3(12):1449, 2007. (cited on page 21)
- [28] Daisuke Mizuno, Rommel Bacabac, Catherine Tardin, David Head, and Christoph F. Schmidt. High-resolution probing of cellular force transmission. *Physical review letters*, 102(16):168102, 2009. (cited on page 22, 24, and 27)
- [29] John Limouze, Aaron F. Straight, Timothy Mitchison, and James R. Sellers. Specificity of blebbistatin, an inhibitor of myosin II. *Journal of muscle research and cell motility*, 25(4):337–341, 2004. (cited on page 30)
- [30] Koji Nobe, Hiromi Nobe, Hiroko Yoshida, Michael S. Kolodney, Richard J. Paul, and Kazuo Honda. Rho A and the Rho kinase pathway regulate fibroblast contraction: Enhanced contraction in constitutively active Rho A fibroblast cells. *Biochemical and biophysical research communications*, 399(2):292–299, 2010. (cited on page 30)
- [31] Melanie Schwingel and Martin Bastmeyer. Force mapping during the formation and maturation of cell adhesion sites with multiple optical tweezers. *PloS one*, 8(1):e54850, 2013. (cited on page 31)
- [32] S. A. Downie and S. A. Newman. Different roles for fibronectin in the generation of fore and hind limb precartilaginous condensations. *Developmental biology*, 172(2):519–530, 1995. (cited on page 31)
- [33] Xuan Huang, Wei Dai, and Zbigniew Darzynkiewicz. Enforced adhesion of hematopoietic cells to culture dish induces endomitosis and polyploidy. *Cell Cycle*, 4(6):801–805, 2005. (cited on page 31)
- [34] I-L Shih, Y-T Van, and M-H Shen. Biomedical applications of chemically and microbiologically synthesized poly (glutamic acid) and poly (lysine). *Mini reviews in medicinal chemistry*, 4(2):179–188, 2004. (cited on page 31)
- [35] Donald W. Jacobsen, Yolanda D. Montejano, Karin S. Vitols, and F. M. Huennekens. Adherence of L1210 murine leukemia cells to sephacryl-aminopropylcobalamin beads treated with transcobalamin-II. *Blood*, 55(1):160–163, 1980. (cited on page 31)

- [36] Sigma-Aldrich. Poly-L-Lysine Cell Attachment Protocol, 2008. (cited on page 31 and 120)
- [37] Oliva Saldanha, Martha E. Brennich, Manfred Burghammer, Harald Herrmann, and Sarah Köster. The filament forming reactions of vimentin tetramers studied in a serial-inlet microflow device by small angle x-ray scattering. *Biomicrofluidics*, 10(2):24108, 2016. (cited on page 35)
- [38] Guilhem Velve-Casquillas, Maël Le Berre, Matthieu Piel, and Phong T. Tran. Microfluidic tools for cell biological research. *Nano today*, 5(1):28–47, 2010. (cited on page 35)
- [39] Mathieu Morel, Denis Bartolo, Jean-Christophe Galas, Maxime Dahan, and Vincent Studer. Microfluidic stickers for cell- and tissue-based assays in microchannels. *Lab on a chip*, 9(7):1011–1013, 2009. (cited on page 36, 38, and 48)
- [40] Denis Bartolo, Guillaume Degre, Philippe Nghe, and Vincent Studer. Microfluidic stickers. *Lab on a chip*, 8(2):274–279, 2008. (cited on page 36 and 48)
- [41] Philip Wägli, Alexandra Homsy, and Nico F. de Rooij. Norland optical adhesive (NOA81) microchannels with adjustable surface properties and high chemical resistance against IR-transparent organic solvents. *Procedia Engineering*, 5:460–463, 2010. (cited on page 37 and 46)
- [42] <https://www.norlandprod.com/adhesives/noa>. Norland Optical Adhesive 81. (cited on page 37, 48, and 63)
- [43] Emile P. Dupont, Raphaëlle Luisier, and Martin A.M. Gijs. NOA 63 as a UV-curable material for fabrication of microfluidic channels with native hydrophilicity. *Microelectronic Engineering*, 87(5):1253–1255, 2010. (cited on page 37 and 45)
- [44] Eric Schilling. Basic microfluidic concepts. *Yager Research Laboratory*. <http://www.faculty.washington.edu/yagerp/microfluidicstutorial/basicconcepts/basicconcepts.htm>, 2001. (cited on page 39)
- [45] *Microlithographic Techniques in IC Fabrication*. SPIE, 1997. (cited on page 40)

- [46] H. Ryssel D. Srikanth. Optical projection lithography- 2009 Indo-German Winter Academy. (cited on page 40)
- [47] N. Cheung, U.C. Berkeley Lectures/lec_11. Photolithography. (cited on page 40)
- [48] James D. Plummer, Michael D. Deal, and Peter B. Griffin. *Silicon VLSI technology: Fundamentals, practice, and modeling / James D. Plummer, Michael Deal, Peter B. Griffin*. Prentice Hall electronics and VLSI series. Prentice Hall, Upper Saddle River, N.J. and London, 2000. (cited on page 41)
- [49] Benjamin D. Fairbanks, Michael P. Schwartz, Christopher N. Bowman, and Kristi S. Anseth. Photoinitiated polymerization of PEG-diacrylate with lithium phenyl-2,4,6-trimethylbenzoylphosphinate: polymerization rate and cytocompatibility. *Biomaterials*, 30(35):6702–6707, 2009. (cited on page 40 and 42)
- [50] Joel S. Paustian, Rodrigo Nery Azevedo, Sean-Thomas B. Lundin, Matthew J. Gilkey, and Todd M. Squires. Microfluidic Microdialysis: Spatiotemporal Control over Solution Microenvironments Using Integrated Hydrogel Membrane Microwindows. *Physical Review X*, 3(4), 2013. (cited on page 42, 43, 51, 57, 61, and 116)
- [51] Joel S. Paustian, Craig D. Angulo, Rodrigo Nery-Azevedo, Nan Shi, Amr I. Abdel-Fattah, and Todd M. Squires. Direct Measurements of Colloidal Solvophoresis under Imposed Solvent and Solute Gradients. *Langmuir : the ACS journal of surfaces and colloids*, 31(15):4402–4410, 2015. (cited on page 43 and 47)
- [52] Joel S. Paustian, Craig D. Angulo, Rodrigo Nery-Azevedo, Nan Shi, Amr I. Abdel-Fattah, and Todd M. Squires. Direct Measurements of Colloidal Solvophoresis under Imposed Solvent and Solute Gradients. *Langmuir : the ACS journal of surfaces and colloids*, 31(15):4402–4410, 2015. (cited on page 43)
- [53] C. Belon, X. Allonas, C. Croutxé-barghorn, and J. Lalevée. Overcoming the oxygen inhibition in the photopolymerization of acrylates: A study

- of the beneficial effect of triphenylphosphine. *Journal of Polymer Science Part A: Polymer Chemistry*, 48(11):2462–2469, 2010. (cited on page 43)
- [54] Aline M. Thomas and Lonnie D. Shea. Cryotemplation for the Rapid Fabrication of Porous, Patternable Photopolymerized Hydrogels. *Journal of materials chemistry. B, Materials for biology and medicine*, 2(28):4521–4530, 2014. (cited on page 43 and 48)
- [55] Ki Wan Bong, Stephen C. Chapin, Daniel C. Pregibon, David Baah, Tamara M. Floyd-Smith, and Patrick S. Doyle. Compressed-air flow control system. *Lab on a chip*, 11(4):743–747, 2011. (cited on page 47)
- [56] Steven R. Caliari and Jason A. Burdick. A practical guide to hydrogels for cell culture. *Nature methods*, 13(5):405–414, 2016. (cited on page 48)
- [57] Christopher A. Durst, Michael P. Cuchiara, Elizabeth G. Mansfield, Jennifer L. West, and K. Jane Grande-Allen. Flexural characterization of cell encapsulated PEGDA hydrogels with applications for tissue engineered heart valves. *Acta biomaterialia*, 7(6):2467–2476, 2011. (cited on page 48)
- [58] Franziska Klein, Benjamin Richter, Thomas Striebel, Clemens M. Franz, Georg von Freymann, Martin Wegener, and Martin Bastmeyer. Two-component polymer scaffolds for controlled three-dimensional cell culture. *Advanced materials (Deerfield Beach, Fla.)*, 23(11):1341–1345, 2011. (cited on page 48)
- [59] Aline M. Thomas and Lonnie D. Shea. Cryotemplation for the Rapid Fabrication of Porous, Patternable Photopolymerized Hydrogels. *Journal of materials chemistry. B, Materials for biology and medicine*, 2(28):4521–4530, 2014. (cited on page 60)
- [60] Anna Valpuri Hakala. Implantoitava glukoosipolttokenno anturina ja teholähteenä–teoreettinen tausta ja mallinnus. 2016. (cited on page 61)
- [61] Imad A. Farhat, Edouard Loisel, Pedro Saez, William Derbyshire, and John Blanshard. The effect of sugars on the diffusion of water in starch gels: a pulsed field gradient NMR study. *International journal of food science & technology*, 32(5):377–387, 1997. (cited on page 61)

- [62] Betty J. M. Hannoun and Gregory Stephanopoulos. Diffusion coefficients of glucose and ethanol in cell-free and cell-occupied calcium alginate membranes. *Biotechnology and Bioengineering*, 28(6):829–835, 1986. (cited on page 61)
- [63] Rommel G. Bacabac, Daisuke Mizuno, Christoph F. Schmidt, Fred C. MacKintosh, Van Loon, Jack J W A, Jenneke Klein-Nulend, and Theo H. Smit. Round versus flat: bone cell morphology, elasticity, and mechanosensing. *Journal of biomechanics*, 41(7):1590–1598, 2008. (cited on page 65 and 67)
- [64] Gonghao Wang, Wenbin Mao, Rebecca Byler, Krishna Patel, Caitlin Henegar, Alexander Alexeev, and Todd Sulchek. Stiffness dependent separation of cells in a microfluidic device. *PloS one*, 8(10):e75901, 2013. (cited on page 65)
- [65] Rasheena Edmondson, Jessica Jenkins Broglie, Audrey F. Adcock, and Liju Yang. Three-dimensional cell culture systems and their applications in drug discovery and cell-based biosensors. *Assay and drug development technologies*, 12(4):207–218, 2014. (cited on page 66)
- [66] Michael W. Hess, Kristian Pfaller, Hannes L. Ebner, Beate Beer, Daniel Hekl, and Thomas Seppi. Chapter 27 - 3D Versus 2D Cell Culture: Implications for Electron Microscopy. In Thomas Müller-Reichert, editor, *Electron Microscopy of Model Systems*, volume 96 of *Methods in Cell Biology*, pages 649–670. Academic Press, 2010. (cited on page 66)
- [67] François Berthiaume and Jeffrey Robert Morgan. *Methods in Bioengineering: 3D Tissue Engineering*. Artech House, 2010. (cited on page 66)
- [68] Martin P. Stewart, Jonne Helenius, Yusuke Toyoda, Subramanian P. Ramanathan, Daniel J. Muller, and Anthony A. Hyman. Hydrostatic pressure and the actomyosin cortex drive mitotic cell rounding. *Nature*, 469(7329):226–230, 2011. (cited on page 67, 77, 110, and 112)
- [69] Elisabeth Fischer-Friedrich, Yusuke Toyoda, Cedric J. Cattin, Daniel J. Müller, Anthony A. Hyman, and Frank Jülicher. Rheology of the Active Cell Cortex in Mitosis. *Biophysical journal*, 111(3):589–600, 2016. (cited on page 67)

- [70] Kazuaki Nagayama and Takeo Matsumoto. Contribution of actin filaments and microtubules to quasi-in situ tensile properties and internal force balance of cultured smooth muscle cells on a substrate. *American journal of physiology. Cell physiology*, 295(6):C1569–78, 2008. (cited on page 68)
- [71] Kristina Haase and Andrew E. Pelling. Investigating cell mechanics with atomic force microscopy. *Journal of the Royal Society, Interface*, 12(104):20140970, 2015. (cited on page 68)
- [72] Marina Soares e Silva, Martin Depken, Björn Stuhmann, Marijn Korsten, Fred C. MacKintosh, and Gijsje H. Koenderink. Active multi-stage coarsening of actin networks driven by myosin motors. *Proceedings of the National Academy of Sciences of the United States of America*, 108(23):9408–9413, 2011. (cited on page 68)
- [73] Gregory W. dehart and Jonathan C. R. Jones. Myosin-mediated cytoskeleton contraction and Rho GTPases regulate laminin-5 matrix assembly. *Cytoskeleton*, 57(2):107–117, 2004. (cited on page 68)
- [74] Andrew G. Clark, Kai Dierkes, and Ewa K. Paluch. Monitoring actin cortex thickness in live cells. *Biophysical journal*, 105(3):570–580, 2013. (cited on page 68)
- [75] Tony Yeung, Penelope C. Georges, Lisa A. Flanagan, Beatrice Marg, Miguelina Ortiz, Makoto Funaki, Nastaran Zahir, Wenyu Ming, Valerie Weaver, and Paul A. Janmey. Effects of substrate stiffness on cell morphology, cytoskeletal structure, and adhesion. *Cytoskeleton*, 60(1):24–34, 2005. (cited on page 69)
- [76] Venkaiah Betapudi. Life without double-headed non-muscle myosin II motor proteins. *Frontiers in chemistry*, 2:45, 2014. (cited on page 70)
- [77] Mihály Kovács, Judit Tóth, Csaba Hetényi, András Málnási-Csizmadia, and James R. Sellers. Mechanism of blebbistatin inhibition of myosin II. *The Journal of biological chemistry*, 279(34):35557–35563, 2004. (cited on page 69 and 70)

- [78] Miguel Vicente-Manzanares, Xuefei Ma, Robert S. Adelstein, and Alan Rick Horwitz. Non-muscle myosin II takes centre stage in cell adhesion and migration. *Nature reviews. Molecular cell biology*, 10(11):778–790, 2009. (cited on page 70)
- [79] Andrew G. Clark and Ewa Paluch. Mechanics and regulation of cell shape during the cell cycle. *Results and problems in cell differentiation*, 53:31–73, 2011. (cited on page 76, 95, and 112)
- [80] Guokai Chen, Zhonggang Hou, Daniel R. Gulbranson, and James A. Thomson. Actin-myosin contractility is responsible for the reduced viability of dissociated human embryonic stem cells. *Cell stem cell*, 7(2):240–248, 2010. (cited on page 85)
- [81] Sven K. Vogel, Zdenek Petrasek, Fabian Heinemann, and Petra Schwille. Myosin motors fragment and compact membrane-bound actin filaments. *Elife*, 2:e00116, 2013. (cited on page 91)
- [82] K. Kruse, J. F. Joanny, F. Jülicher, J. Prost, and K. Sekimoto. Asters, vortices, and rotating spirals in active gels of polar filaments. *Physical review letters*, 92(7):78101, 2004. (cited on page 95)
- [83] W. O. Kwant and Philip Seeman. The Erythrocyte Ghost Is a Perfect Osmometer. *The Journal of General Physiology*, 55(2):208–219, 1970. (cited on page 97)
- [84] Torsten Teorell. PERMEABILITY PROPERTIES OF ERYTHROCYTE GHOSTS. *The Journal of General Physiology*, 35(5):669–701, 1952. (cited on page 97)
- [85] Priyamvada Chugh, Andrew G. Clark, Matthew B. Smith, Davide A. D. Cassani, Kai Dierkes, Anan Ragab, Philippe P. Roux, Guillaume Charras, Guillaume Salbreux, and Ewa K. Paluch. Actin cortex architecture regulates cell surface tension. *Nature cell biology*, 19(6):689–697, 2017. (cited on page 103)
- [86] Farshid Guilak, Geoffrey R. Erickson, and H. Ping Ting-Beall. The Effects of Osmotic Stress on the Viscoelastic and Physical Properties of Articular Chondrocytes. *Biophysical journal*, 82(2):720–727, 2002. (cited on page 103 and 112)

- [87] E. H. Zhou, X. Trepát, C. Y. Park, G. Lenormand, M. N. Oliver, S. M. Mijailovich, C. Hardin, D. A. Weitz, J. P. Butler, and J. J. Fredberg. Universal behavior of the osmotically compressed cell and its analogy to the colloidal glass transition. *Proceedings of the National Academy of Sciences of the United States of America*, 106(26):10632–10637, 2009. (cited on page 103 and 115)
- [88] I. L. Ivanovska, P. J. de Pablo, B. Ibarra, G. Sgalari, F. C. MacKintosh, J. L. Carrascosa, C. F. Schmidt, and G. J. L. Wuite. Bacteriophage capsids: tough nanoshells with complex elastic properties. *Proceedings of the National Academy of Sciences of the United States of America*, 101(20):7600–7605, 2004. (cited on page 106, 109, and 117)
- [89] E. H. Zhou, X. Trepát, C. Y. Park, G. Lenormand, M. N. Oliver, S. M. Mijailovich, C. Hardin, D. A. Weitz, J. P. Butler, and J. J. Fredberg. Universal behavior of the osmotically compressed cell and its analogy to the colloidal glass transition. *Proceedings of the National Academy of Sciences of the United States of America*, 106(26):10632–10637, 2009. (cited on page 106, 109, and 117)
- [90] Harvard University. A Summary of Error Propagation /Physical Sciences2, 2007. (cited on page 108)
- [91] L.D. Landau & E.M. Lifshitz. *Theory of Elasticity*. Oxford, 3rd edition, 1984. (cited on page 109 and 110)
- [92] Ming Guo. *Physical Nature of Cytoplasm*. PhD thesis, Harvard University, 01.01.2014. (cited on page 109 and 112)
- [93] Andreas Fery and Richard Weinkamer. Mechanical properties of micro- and nanocapsules: Single-capsule measurements. *Polymer*, 48(25):7221–7235, 2007. (cited on page 111 and 112)
- [94] www.microchem.com. SU-8 3000 SU-8 3000 Permanent Epoxy Negative Photoresist. (cited on page 125)

List of Figures

1.1	Typical length scales in cell mechanics.	2
1.2	Myosin family in leukocytes	3
1.3	Cellular pressure and volume regulation	4
1.4	Experimental techniques for probing cell mechanics	5
2.1	Optical tweezers principle in Ray regime	9
2.2	Back-focal-plane interferometry	11
2.3	Quadrant photo diode response	12
2.4	Calibration of optical trap using power spectrum	13
2.5	Schematic layout of the dual optical trap set-up	15
2.6	Schematic adjustment of telescope lenses	16
2.7	Bragg diffraction	17
2.8	AA Optoelectronic 2-axis AO-Deflectors	18
2.9	Representation of output optical beams of 2-axis AOD	19
2.10	Two-particle microrheology of cellular system using optical traps	21
2.11	Representation of cellularforce measurement using OT	23
2.12	Response function of MLO-Y4 cell measured by AMR and PMR	24
2.13	Representation of stiffness measurement	25
2.14	Representation of time-course displacements in Active MR	26
2.15	Representative measurement of cell stiffness	27
2.16	Representative measurement of cellular force	28
2.17	Frequency dependence of cellular force fluctuations	28
2.18	Two-particle microrheology in a microfluidic device	33
3.1	NOA-81 Transmission Spectrum	37
3.2	Micro-device design	38

3.3	Actual photoresist profile in comparison to its trapezoidal model	40
3.4	Light projection depth of focus	41
3.5	Mercury arc spectrum	41
3.6	Photo-initiator absorption spectrum	42
3.7	Compressed-air driven flow	47
3.8	Sticker preparation	50
3.9	Device-Close Up view	51
3.10	Laser scanning confocal microscope	52
3.11	LAS AF software interface	53
3.12	HMM fabrication in FlowChamber	54
3.13	Light path inside the flow chamber	55
3.14	Signal amplitude and power spectral density in flow chamber depends on distance to HMM	57
3.15	Light path inside the flow chamber	58
3.16	Long UV exposure HMM	59
3.17	Short UV exposure HMM	59
3.18	Thick versus thin HMM	60
3.19	Transmembrane flow	61
3.20	Diffusion of fluorescein molecules through hydrogel membranes	62
3.21	Diffusion of fluorescein molecules through hydrogel membranes	63
4.1	Connection between cellular morphology, internal structures and mechanical properties	66
4.2	Mammalian cell morphology	67
4.3	Cytoskeletal organization of adherent and non-adherent cells	69
4.4	Acto-myosin cortex of non-adherent cells	70
4.5	Blebbistatin treatment of myosin labeled 3T3 fibroblasts	71
4.6	Probed cell lines with different morphology	73
4.7	Mechanical properties of different cell lines brought into suspension	74
4.8	Fluorescent confocal imaging of GFP transfected fibroblast	75
4.9	Fluorescent confocal image of RFP transfected fibroblasts	76

4.10 Volume and cross section of fibroblasts changes after myosin inhibition 76

4.11 Fluorescent confocal image of GFP transfected fibroblasts . . . 77

4.12 Volume of fibroblasts changes after myosin inhibition 77

4.13 Two particles microrheology in microfluidic device 79

4.14 Long term stiffness measurements of cells suspended in the flow chamber 81

4.15 Time series of the spring constant blebbistatin treated 3T3 fibroblasts 82

4.16 Spring constants of blebbistatin treated 3T3 fibroblasts 83

4.17 Force fluctuations of blebbistatin treated 3T3 fibroblasts 84

4.18 Force generated by blebbistatin treated 3T3 fibroblasts 85

4.19 Spring constant of Y-27632 treated 3T3 fibroblasts 86

4.20 Force generated by Y-27632 treated 3T3 fibroblasts 87

4.21 3T3 fibroblasts stiffness during treatment and recovery 89

5.1 Surface tension and intracellular pressure 95

5.2 Cell volume changes in hypertonic medium 98

5.3 Rapid exchange of the side-solutions make cell in the middle channel swell or shrink. 99

5.4 Rapid exchange of the side-solutions make cell in the middle channel swell or shrink. 99

5.5 Cell volume shrinkage from hypo- to hyper-tonic medium . . 100

5.6 Suspended cell hold with two trapped micro-particles. 100

5.7 Stiffness and force fluctuations of L1210 cells in isotonic compared with hypertonic medium 102

5.8 Gradual sugar diffusion changed the cell size held with trapping particles 104

5.9 Cross section area of the 3T3 cell, suspended in microfluidic chamber and held with trapping particles exposed to gradual sugar diffusion 104

5.10 Dependence of relative cell volume on inverse osmotic stress . 105

5.11 Cell stiffness changes by osmotic pressure corresponding to the sugar level 106

5.12 Normalized cell stiffness changes in mild hypertonic medium 107

5.13 Normalized cell stiffening in hypertonic sugary medium . . .	107
5.14 Comparison of normalized cell stiffness in hypertonic sugary medium and in absence of sugar	108
5.15 Cell stiffness correlates with its volume	109
B.1 AOD back and front view	124

Abbreviations

AFM	Atomic force microscopy
AMR	Active microrheology
AOD	Acousto-optic deflector
ATP	Adenosine triphosphate
BFP	Back focal plane
BSA	Bovine Serum Albumin
DDS	Dimethyl-dichloro-silane
DM	Dichroic mirror
DMEM	Dulbecco's Modified Eagle's medium
DNA	Deoxyribonucleic acid
DOF	Depth of focus
FBS	Fetal Bovine Serum
FDT	Fluctuation dissipation theorem
GFP	Green fluorescent protein
HMM	Hydrogel micro-membrane
IPA	Iso-propanole
MFS	Micro-fluidic sticker
MR	Microrheology
NA	Numerical aperture
NMM	Non-muscle myosin
NOA	Norland optical adhesive
OT	Optical trap
PDMS	Poly-di-methyl-siloxane
PEG-DA	Poly-ethylene-glycol diacrylate
PLL	Poly-L-Lysine
PMR	Passive microrheology
PSD	Power spectral density
QPD	Quadrant photo diode
RF	Radio frequency
RFP	Red fluorescent protein
RI	Refractive index
ROI	Region of interest
TL	Telescope lens

Acknowledgments

It has been a long journey. I have received tremendous help and guidance from so many people. Saving many stories for my memoir, below I give an incomplete list of people without whom the last four years would not have been possible.

First and foremost I like to thank my supervisor Prof. Christoph F. Schmidt whom it is always an honor working with him. He trusted me with giving the opportunity to start biophysics from scratch, then an infinite freedom to learn, and to find my way. Last couple of years I had a chance attending the best scientific meetings, conferences, lab visits all around the world keeping myself up to date on current topics in biophysics. All this while he was the strong support. I owe it all to him; wish life keeps him always active and smiling.

I had the privilege of working with Prof. Todd Squires, whose lab in UC Santa Barbara kindly hosted me. This collaboration led to a new direction in my work which forms the cornerstone of this thesis. I have to thank him and Dr. Nan Shi for introducing me to their micro-devices, and inspiring me with their engineering perspectives. Indeed Nan kept his eyes on me, worked side by side for a month in Santa Barbara and later had several discussions over emails regarding the device' design.

I also extend my heartfelt gratitude to:

Dr. Florian Rehfeldt and Dr. Dieter Klopfenstein, for all their scientific comments, useful hints, critiques and advices especially during Friday' seminars. I admire Dieter's patience and dedication, always encouraging to answer my biochemistry questions, even if sometimes led to more reading for him. I wish him the best for his career.

Dr. Florian Schlosser who first introduced me to experimental techniques in cell mechanics, from confocal microscopy to optical trapping and microrheology.

Dr. Carina Wollnik, who taught me from biophysics basics starting with 'What is a cell? ' I learned a lot from her, from culturing, labeling, to cell treatments. She was open to all my questions throughout.

Dr. Renata Garces and Dr. Kengo Nishi, caring postdocs and good friends, for their scientific help and professional advices; Renata for 100s of coffees along our loud and cheerful conversations over almost everything and her smart questions always triggering me. I wish she keeps up her passions forever. Kengo, whose point of view and experimental approach looks simple yet it is thoughtful. With him, I enjoyed working on trap alignments, studying microrheology and discussing over many things.

I am deeply in debt to all my colleagues and friends in the third institute of physics, some of whom I started and ended my work with and others who were a source of valuable company. Andre, Florian, Alok, Meenakshi, Christopher, Mitja, Ulrich, Carina, Eugenia, Til, Achintya and Galina (all with Dr. title now!), as well as Miquel, Gabriele, Christina, Constantin, Philip, Daniel (M), Daniel (H), Peter, Theresa, Philipp also recently joined Post-Docs Amna, Chonglin, Jianguo, and of course the fresh motivated PhDs Soheil, Heidi and Behzad. You provided a happy, wonderful and active working atmosphere. All of you were considerate and kind throughout my time here and some became close friends. Thank you and wishing the best of luck for your career or studies.

I was lucky to be around with the finest staff at DPI, secretaries Nicole and Ewa and lab technicians Kerstin, Ulrika and Tanja. I looked forward to seeing your happy, friendly faces every day. Tanja, thanks a lot for helping me prepare solutions, place purchase orders and most importantly saving my mornings with fresh coffee! I almost never needed breakfast apart from that.

Many thanks to IT administration, mechanics and electronics workshop' staff of DPI, who were an immense help for the technical parts.

My special thanks to Dieter, Oliva, Carina, Anna, Christina, Renata, Gabriele, Heidi and Subha for life-saving proofreading of this thesis draft. It's definitely benefited from the corrections.

My best friends, faithful companions and roommates Christina and Oliva, who stood by me through ups and downs. Apart from the fun, happy, cheerful times and unforgettable loud laughs, sharing my years with you given me strength to always step forward but not back. Thank you very much for your cheerful spirits and kind hearts. Wish you everlasting smiles!

Dr. Anna-Lena Robisch, I was incredibly lucky to be in a wrong place at the right time to meet you. Soon you became a friend who stood in difficulty and ease. I had happy times with you from top of cherry threes to last days of thesis writing. Wish you a sunny smile and happy thoughts as always!

Dr. Tahere Rouhi, we became close and made amazing memories together from Zanzan, to Sari, Esfahan and Boroujen, up till Germany. It's a 10 years story now and you are still the one whom I call when need someone to hear me out. Doesn't matter where we are in this world or in our lives. Thanks for being my support all along actively, from creative day-long jokes to late night conversations, with no judgment reminding me to be true to myself! Wish you all the best days filled with laughter and joy!

IQMG, our Persian community that have helped me a lot with the regular meetings since the very beginning in Gottingen, through happy days as well as taught ones. It was a great pleasure to have you around. I am so grateful for making me feel home and faithfully thanking you all.

Last but my utmost regards and deepest gratitude to my family, who were the biggest support throughout my life. Although they were far, yet stood close all along this way; as my motivation to start, companion throughout and encouragement till the end. I am so beyond thankful to them.

The deepest appreciation to my parents for being the real meaning of compassion and faithfully giving me their best of love. If not for their day-to-day inspiration, drive and support -in so many ways- I would not be here today. Thanks a lot for teaching me life is a short story, yet worth to do my best. Words could never be enough to express my gratitude!

September 2017,
Göttingen

Affidavit

I herewith declare that I have produced this dissertation without the prohibited assistance of third parties and without making use of aids other than those specified; notions taken over directly or indirectly from other sources have been identified as such. This dissertation has not previously been presented in identical or similar form to any other German or foreign examination board.

The thesis work was conducted from April 2014 to October 2017 under the supervision of Prof. Dr. Christoph F. Schmidt at the Third Institute of Physics - Biophysics.

Samaneh Rezvani

Göttingen, October 2017

Curriculum Vitae

Personal data

Name: Samaneh Rezvani-Boroujeni
Address: Im Hassel 15
37077 Göttingen
Germany
E-Mail: srezvani@physik3.gwdg.de
Date of birth: 6/ 9/1985
Place of birth: Esfahan
Nationality: Iranian

Education

2014- 2017 PhD studies in Physics
Georg-August-Universität Göttingen
Third Institute of Physics- Biophysics
PhD thesis: "Mechanical and biochemical stimulation of suspended cells in a microfluidic device"
Supervisor: Prof. Christoph F. Schmidt

2007- 2009 Master studies in Atomic and Molecular Physics (Optics)
University of Zanjan
Faculty of Sciences
Master thesis: "Optical test of aspheric surface with moiré technique"
Supervisor: Dr. Ahmad Darudi

2003- 2007 Bachelor of Science in Solid State Physics
Isfahan University of Technology (IUT)
& Bu Ali Sina University
Bachelor project: "Heat distribution in glasses
under certain boundary conditions"
Supervisor: Dr. Mohammad Amiri

Work experience

2013- 2017 Researcher at the CRC SFB 937 for "Morphogen-
esis of the force-generating machinery in cells"

Publication

Journal of Physics D : Rezvani S., Shi N., Squires T. M., Schmidt C. F.
Applied Physics
Microfluidic device for chemical and mechanical
manipulation of suspended cells
Vol. 51, No. 4, 045403 (9pp), 2018.
https : //doi.org/10.1088/1361 – 6463/aaa121

October 2017,
Göttingen